Suv4-20h2 mediates chromatin compaction and is important for cohesin recruitment to heterochromatin

Matthias Hahn,[1,2,9] Silvia Dambacher,[1,2,9] Stanimir Dulev,[1,2] Anastasia Yurievna Kuznetsova,[3] Simon Eck,[4,5] Stefan Wörz,[4,5] Dennis Sadic,[1,2] Maike Schulte,[1,2] Jan-Philipp Mallm,[5,6] Andreas Maiser,[1,7] Pierre Debs,[8] Harald von Melchner,[8] Heinrich Leonhardt,[1,7] Lothar Schermelleh,[1,7,10] Karl Rohr,[4,5] Karsten Rippe,[5,6] Zuzana Storchova,[3] and Gunnar Schotta[1,2,11]

[1]Munich Center for Integrated Protein Science (CiPS[M]), Ludwig Maximilians University; [2]Adolf-Butenandt-Institute, 80336 Munich, Germany; [3]Max Planck Institute of Biochemistry, 82152 Martinsried, Germany; [4]Department of Bioinformatics and Functional Genomics, Biomedical Computer Vision Group, Institut für Pharmazie und Molekulare Biotechnologie (IPMB), BioQuant, University of Heidelberg, 69120 Heidelberg, Germany; [5]Deutsches Krebsforschungszentrum (DKFZ) Heidelberg, 69120 Heidelberg, Germany; [6]Research Group Genome Organization and Function, BioQuant, 69120 Heidelberg, Germany; [7]Department of Biology II, Biozentrum, 82152 Munich, Germany; [8]Department of Molecular Hematology, University of Frankfurt Medical School, 60590 Frankfurt am Main, Germany

Cohesin plays an important role in chromatid cohesion and has additional functions in higher-order chromatin organization and in transcriptional regulation. The binding of cohesin to euchromatic regions is largely mediated by CTCF or the mediator complex. However, it is currently unknown how cohesin is recruited to pericentric heterochromatin in mammalian cells. Here we define the histone methyltransferase Suv4-20h2 as a major structural constituent of heterochromatin that mediates chromatin compaction and cohesin recruitment. Suv4-20h2 stably associates with pericentric heterochromatin through synergistic interactions with multiple heterochromatin protein 1 (HP1) molecules, resulting in compaction of heterochromatic regions. *Suv4-20h* mutant cells display an overall reduced chromatin compaction and an altered chromocenter organization in interphase referred to as "chromocenter scattering." We found that *Suv4-20h*-deficient cells display chromosome segregation defects during mitosis that coincide with reduced sister chromatid cohesion. Notably, cohesin subunits interact with Suv4-20h2 both in vitro and in vivo. This interaction is necessary for cohesin binding to heterochromatin, as *Suv4-20h* mutant cells display substantially reduced cohesin levels at pericentric heterochromatin. This defect is most prominent in G0-phase cells, where cohesin is virtually lost from heterochromatin, suggesting that Suv4-20h2 is involved in the initial loading or maintenance of cohesion subunits. In summary, our data provide the first compelling evidence that Suv4-20h2 plays essential roles in regulating nuclear architecture and ensuring proper chromosome segregation.

[*Keywords*: Suv39h; Suv4-20h2; chromocenter clustering; chromosome segregation; cohesin; heterochromatin]

Supplemental material is available for this article.

Received November 15, 2012; revised version accepted March 26, 2013.

Pericentric heterochromatin in mammalian cells is formed from large arrays of noncoding satellite repeat sequences. Heterochromatic domains from different chromosomes can join into large clusters (so-called chromocenters) that can be visualized as DAPI-dense regions in interphase cells. Pericentric heterochromatin is largely transcriptionally inert but serves important functions in ensuring genomic stability and accurate chromosome segregation (Peters et al. 2001; Ting et al. 2011; Zhu et al. 2011). Thus, dysregulation of heterochromatin organization leads to severe diseases and developmental defects (Hahn et al. 2010).

The major constitutive heterochromatin proteins that are thought to establish the proper chromatin structure at pericentric heterochromatin are heterochromatin protein 1 (HP1) isoforms and the histone methyltransferases Suv39h and Suv4-20h (Supplemental Fig. S1A). Suv39h enzymes induce histone H3 Lys 9 trimethylation (H3K9me3) at heterochromatic regions (Peters et al. 2001). This modification is recognized by HP1 molecules, which recruit

[9]These authors contributed equally to this work.
[10]Present address: Department of Biochemistry, University of Oxford, Oxford OX1 3QU, United Kingdom.
[11]Corresponding author
E-mail gunnar.schotta@med.uni-muenchen.de
Article published online ahead of print. Article and publication date are online at http://www.genesdev.org/cgi/doi/10.1101/gad.210377.112.

Suv4-20h histone methyltransferases that subsequently establish H4K20me3 (Schotta et al. 2004, 2008). It is assumed that HP1 is a major regulator of heterochromatin organization and compaction. However, this view is challenged by the fact that HP1 proteins only transiently associate with heterochromatin (Cheutin et al. 2003). Therefore, other more constitutive components might contribute to regulating heterochromatin organization.

During mitosis, pericentric heterochromatin is important to facilitate sister chromatid cohesion. This is accomplished by cohesin complexes that connect sister chromatids at pericentric regions until anaphase onset (Salic et al. 2004; Tang et al. 2004). The cohesin ring consists of a Smc1–Smc3 dimer that is connected through the α-kleisin subunit Scc1/Rad21 (Nasmyth 2011). Cohesin is loaded onto chromatin in early G1 phase. Sites of cohesin loading can differ from regions with the highest cohesin enrichment, and therefore the cohesin rings are assumed to slide several kilobases from the loading site (Lengronne et al. 2004), where they might be fixed by interactions with other proteins, such as CTCF (Parelho et al. 2008; Rubio et al. 2008; Wendt et al. 2008). Due to the large size and compact structure of pericentric regions, there must be loading sites within heterochromatin, and it is therefore likely that core heterochromatin proteins assist in stable cohesin recruitment within these domains. In agreement with this hypothesis, cohesin is recruited to heterochromatic regions by Swi6/HP1 in fission yeast (Nonaka et al. 2002). However, HP1 proteins do not interact with cohesin in mammalian cells (Koch et al. 2008), and it is currently unknown how recruitment and maintenance of cohesin at pericentric heterochromatin is mediated.

In this study, we discovered an interaction between the histone methyltransferase Suv4-20h2 and cohesin. We found that Suv4-20h2 is required for cohesin recruitment to pericentric heterochromatin. *Suv4-20h*-deficient cells have strongly reduced cohesin levels at pericentric heterochromatin, resulting in chromosome segregation defects. Thus, our data demonstrate a novel role of the Suv39h–Suv4-20h pathway in cohesin recruitment to pericentric heterochromatin.

Results

Suv4-20h2 is a stable component of pericentric heterochromatin

We first set out to determine whether any of the heterochromatin core proteins could play structural roles in heterochromatin. We assessed their mobility in embryonic stem (ES) cells by fluorescence recovery after photobleaching (FRAP) analysis specifically at pericentric heterochromatin (Supplemental Fig. S1B). Consistent with previous reports (Cheutin et al. 2003), we found that HP1α is a very mobile protein (Fig. 1A). This is a common feature of all HP1 variants, as the other isoforms—HP1β and HP1γ—also displayed the same fast recovery kinetics (K Rippe, pers. comm.). The histone methyltransferases Suv39h1 and Suv4-20h1 showed intermediate mobility. Surprisingly, Suv39h2 and Suv4-20h2 stably associate with heterochromatin, as both proteins showed almost no recovery on the minute time scale (Fig. 1A). In addition, we determined the mobility parameters of the core heterochromatin proteins in another cell system: mouse embryonic fibroblast cells (MEFs). Interestingly, the recovery kinetics of all proteins were slower as compared with ES cells, which is in agreement with the hypothesis that heterochromatin is less plastic in differentiated cells (Meshorer et al. 2006). Similarly to ES cells, we found that Suv39h2 and Suv4-20h2 exhibit the strongest binding to heterochromatin (Fig. 1A). These experiments were complemented by fluorescence correlation spectroscopy (FCS) measurements of Suv4-20h2 at endogenous expression levels (Supplemental Fig. S2). For these assays, we generated a *Suv4-20h2*^{EGFP} knock-in ES cell line that expresses *Suv4-20h2* at nearly endogenous levels (Supplemental Fig. S2B) and displays clear enrichment of Suv4-20h2 and H4K20me3 at pericentric heterochromatin (Supplemental Fig. S2C). FCS mobility measurements confirm that at endogenous expression levels, the mobile Suv4-20h2 binds more tightly to chromatin than HP1, since its apparent diffusion coefficient, which includes the binding contribution, is reduced (Supplemental Fig. S2D). Furthermore, the immobile pool of Suv4-20h2 was ~10 times higher than that of HP1, as determined from continuous photobleaching experiments (Supplemental Fig. S2E). Taken together, our data suggest that the histone methyltransferases Suv39h2 and Suv4-20h2 could play structural roles in pericentric heterochromatin.

Stable binding of Suv4-20h2 is mediated through synergistic HP1 interactions

The stable binding of Suv4-20h2 to heterochromatin was also demonstrated in a previous study for human SUV4-20H2 (Souza et al. 2009), suggesting that this feature of Suv4-20h2 is evolutionarily conserved. However, as the bulk of HP1 only transiently associates with heterochromatin, it is surprising that Suv4-20h2 can stably bind heterochromatin. Therefore, we asked how this stable association of Suv4-20h2 is mediated. The C terminus of Suv4-20h2 is responsible for heterochromatin targeting (Schotta et al. 2004). In order to better define the targeting domain, we generated a panel of EGFP-tagged Suv4-20h2 truncation proteins as subfragments of the C terminus (Fig. 1B). Fragment M12, which comprises only 62 amino acids of the Suv4-20h2 C terminus, showed clear pericentric enrichment (Fig. 1B; Supplemental Fig. S2F). We further subdivided this fragment and found that two nonoverlapping truncations—M13 and M14—were both able to localize to pericentric heterochromatin as well (Fig. 1B; Supplemental Fig. S2F). These data indicate that at least two independent heterochromatin targeting modules exist in Suv4-20h2. We then asked whether the M12 region is really crucial for mediating pericentric recruitment of Suv4-20h2 and tested the localization of a Suv4-20h mutant protein lacking the M12 region. We did not detect enrichment of this mutant protein at pericentric

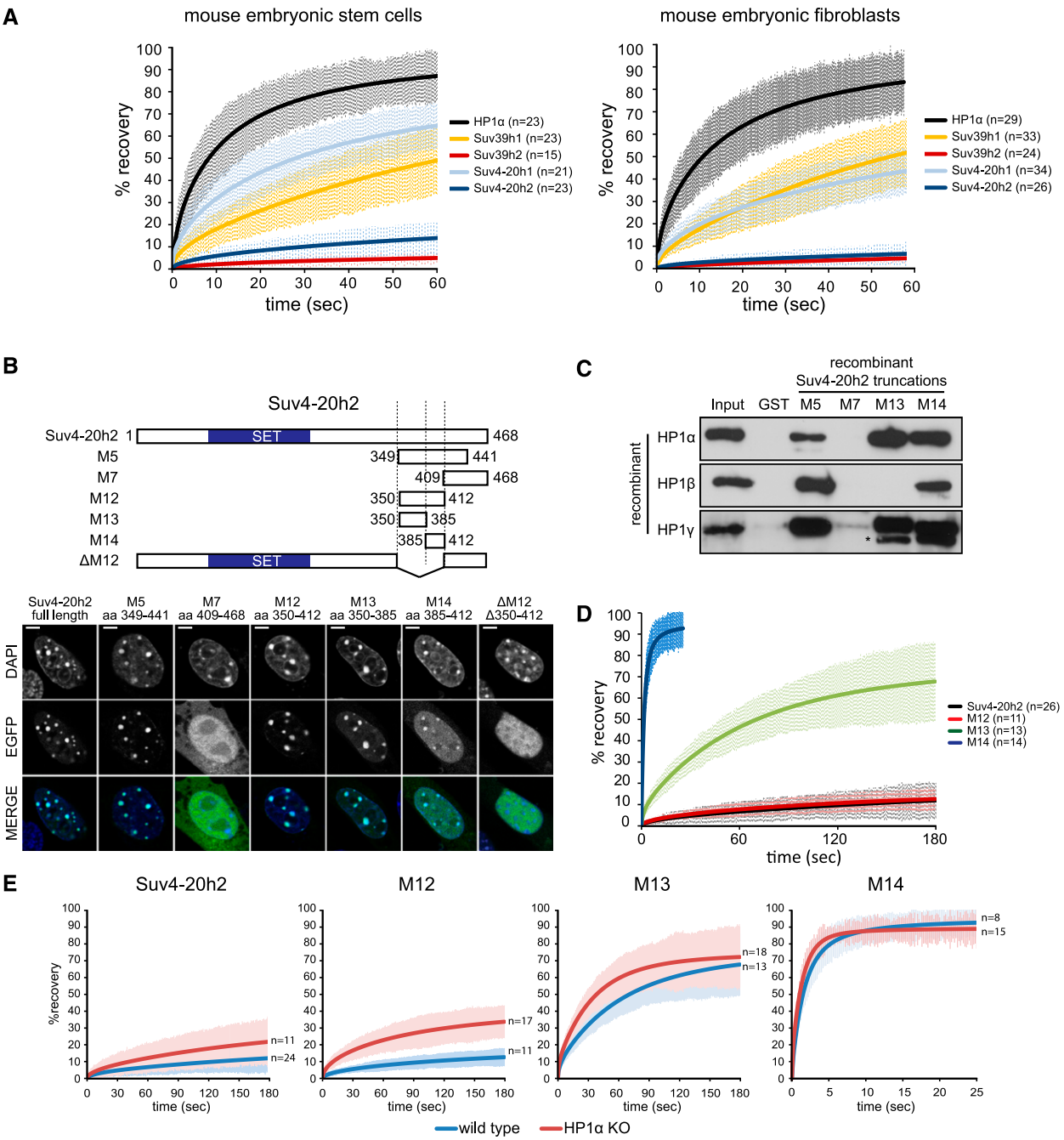

Figure 1. Suv4-20h2 is a stable component of pericentric heterochromatin. (*A*) FRAP analysis of core heterochromatin proteins. EGFP-tagged proteins were expressed in wild-type ES cells and MEFs. Laser bleaching and analysis of fluorescence recovery were carried out specifically at pericentric heterochromatin. FRAP recovery experiments for multiple cells (indicated in the legend) were averaged and fitted to a reaction diffusion model. Error bars represent the standard deviation of the FRAP measurements in each series. (*B*) Distinct regions in the C terminus mediate heterochromatin localization of Suv4-20h2. (*Top* panel) Schematic showing Suv4-20h2 truncation proteins that were expressed as EGFP fusion proteins in wild-type MEFs. (*Bottom* panel:) Confocal sections of MEFs expressing EGFP-tagged Suv4-20h2 truncations. Bars, 5μm. (*C*) In vitro interaction test of Suv4-20h2 truncation proteins and HP1 isoforms. GST-tagged Suv4-20h2 truncation proteins were bound to GST beads and incubated with recombinant HP1α, HP1β, and HP1γ, respectively. Bound proteins were separated on SDS page and probed with HP1 isoform-specific antibodies. The asterisk indicates cross-reacting bands with the HP1γ antibody. (*D*) FRAP kinetics of Suv4-20h2 truncation proteins at pericentric heterochromatin. The C-terminal fragment M12 is as stable as the full-length Suv4-20h2 protein. Subfragments of M12 (M13 and M14) show a much faster recovery. FRAP recovery experiments for multiple cells (indicated in the legend) were averaged and fitted to a reaction diffusion model. Error bars represent the standard deviation of the FRAP measurements in each series. (*E*) Suv4-20h2 is more dynamic in HP1α mutant cells. Suv4-20h2 full-length and truncation proteins were expressed in wild-type and HP1α knockout cells. FRAP kinetics at heterochromatin of all Suv4-20h2 truncations are faster in HP1α mutant cells. FRAP recovery experiments for multiple cells (indicated in the legend) were averaged and fitted to a reaction diffusion model. Error bars represent the standard deviation of the FRAP measurements in each series.

heterochromatin (Fig. 1B). Thus, we conclude that the region comprising amino acids 350–412 represents the heterochromatin targeting domain in Suv4-20h2.

Heterochromatin targeting of Suv4-20h2 depends on HP1 proteins (Schotta et al. 2004). We found that Suv4-20h2 can interact with all three mammalian HP1 isoforms in living cells (Supplemental Fig. S3). In vitro interaction assays revealed that all Suv4-20h2 truncations that localize to heterochromatin can directly interact with HP1 isoforms (Fig. 1C). Suv4-20h2 fragment M12 could not be generated as a soluble recombinant protein. However, as fragment M5 interacts with HP1 and fragment M7 does not show interaction with HP1, we conclude that the HP1 interaction domain resides within fragment M12. This is further supported by our finding that fragments M13 and M14, which are subregions of fragment M12, strongly interact with HP1 (Fig. 1C). Interestingly, HP1α and HP1γ appear as the major interaction partners with both M13 and M14, whereas HP1β only interacts with fragment M14 (Fig. 1C). These data are in line with recent reports on HP1 interaction networks that demonstrate that HP1α and HP1γ share similar interaction partners that do not necessarily overlap with HP1β interactors (Vermeulen et al. 2010). In summary, these data demonstrate that Suv4-20h2 has multiple independent HP1 interaction sites within its C terminus.

We further characterized the Suv4-20h2 truncations by measuring their mobility in heterochromatin using FRAP analysis. Full-length Suv4-20h2 stably binds to heterochromatin and showed a recovery of only ~10% at 3 min post-bleaching (Fig. 1D). The Suv4-20h2-M12 truncation behaved virtually identical to the full-length protein, indicating that this fragment comprises the essential domain that "clamps" Suv4-20h2 onto heterochromatin (Fig. 1D). We therefore refer to this region as the Suv4-20h2 "clamp domain." Notably, the mobility of the M12 subfragments M13 and M14 was much higher. While the mobility of fragment M14 was in the range of HP1, M13 was more stably bound than HP1 (Fig. 1D), suggesting that distinct regions in Suv4-20h2 mediate the stable association with heterochromatin through interactions with HP1 proteins.

To test this hypothesis, we measured the mobility of the individual Suv4-20h truncations in fibroblasts with reduced HP1 levels. HP1α knockout cells retained both H3K9me3 and H4K20me3 at pericentric heterochromatin, indicating that the recruitment of Suv39h and Suv4-20h enzymes to heterochromatin is not generally impaired (Supplemental Fig. S4A). Indeed, the localization of the Suv4-20h2 truncations was not altered in the absence of HP1α (Supplemental Fig. S4B). However, the FRAP recovery kinetics of full-length Suv4-20h2 and truncations M12 and M13 were clearly enhanced (Fig. 1E). We did not observe faster recovery of fragment M14, as the FRAP kinetics of this fragment were already in the range of HP1 in wild-type cells. In summary, our data suggest that Suv4-20h2 is bound to heterochromatin through at least two independent interaction sites by HP1 proteins. As the individual interactions can only generate intermediate stability (M13 and M14), we postulate that synergistic interaction with multiple HP1 proteins in the Suv4-20h2 clamp domain ensures its stable association with heterochromatin.

Suv4-20h2 regulates chromatin compaction

The tight interaction of Suv4-20h2 with heterochromatin suggests a direct involvement in regulating the structure of pericentric heterochromatin. To verify this hypothesis, we performed micrococcal nuclease (MNase) chromatin accessibility assays in wild-type, *Suv4-20h2* knockout, and *Suv4-20h* double-knockout ES cells (Schotta et al. 2008). Notably, we detected higher chromatin accessibility in both *Suv4-20h2* knockout and *Suv4-20h* double-knockout cells (Fig. 2A,B). The increased accessibility clearly involves heterochromatic regions, as demonstrated by Southern blotting of the digested DNA with major satellite probes (Fig. 2A,B). A similar increase in chromatin accessibility was also observed in *Suv4-20h*-deficient MEF cells, suggesting that Suv4-20h2 plays general roles in regulating chromatin structure (Supplemental Fig. S5). Importantly, re-expression of *Suv4-20h2*, which restores H4K20me3 (Nicetto et al. 2013), and even of the Suv4-20h2 clamp domain (M12) rescues the accessibility phenotype of *Suv4-20h* double-knockout cells (Supplemental Fig. S5), indicating that Suv4-20h2 can induce chromatin compaction through its clamp domain.

Superresolution three-dimensional (3D) structured illumination microscopy (3D-SIM) is a recently developed technique that allows imaging of subcellular structures below the optical diffraction limit (Schermelleh et al. 2008). Using this technique, we detected a slightly reduced chromatin density in *Suv4-20h* double-knockout cells around the nuclear envelope (Fig. 2C; Supplemental Fig. S6). We quantified these data by measuring the DAPI intensity of the nuclear periphery compared with the overall DAPI intensity of the nuclei (Supplemental Fig. S6B). These data indicate that wild-type nuclei have a generally higher chromatin density in the nuclear periphery as compared with *Suv4-20h* double-knockout cells (Supplemental Fig. S6C). Interestingly, this reduction in peripheral heterochromatin correlates with changes in the distribution of nuclear pores, which are more stochastically arranged in *Suv4-20h* double-knockout nuclei (Fig. 2C). Strong overexpression of *Suv4-20h2* results in dramatic changes of the nuclear structure, most notably in increased chromatin compaction around chromocenters, nucleoli, and the nuclear envelope (Fig. 2C; Supplemental Fig. S6A). The increased density of the peripheral heterochromatin upon overexpression of *Suv4-20h2* is again reflected in the altered distribution of nuclear pores, which tend to be excluded from the highly compacted regions. In order to quantify the effect of Suv4-20h2 on nuclear pore organization, we developed an automatic 3D image analysis approach to measure nuclear pore parameters in our 3D-SIM images (Supplemental Fig. S6D). In agreement with the qualitative analysis of the nuclear pore staining, we found that the percentage of regions with low nuclear pore density (sparse nuclear pore regions) was

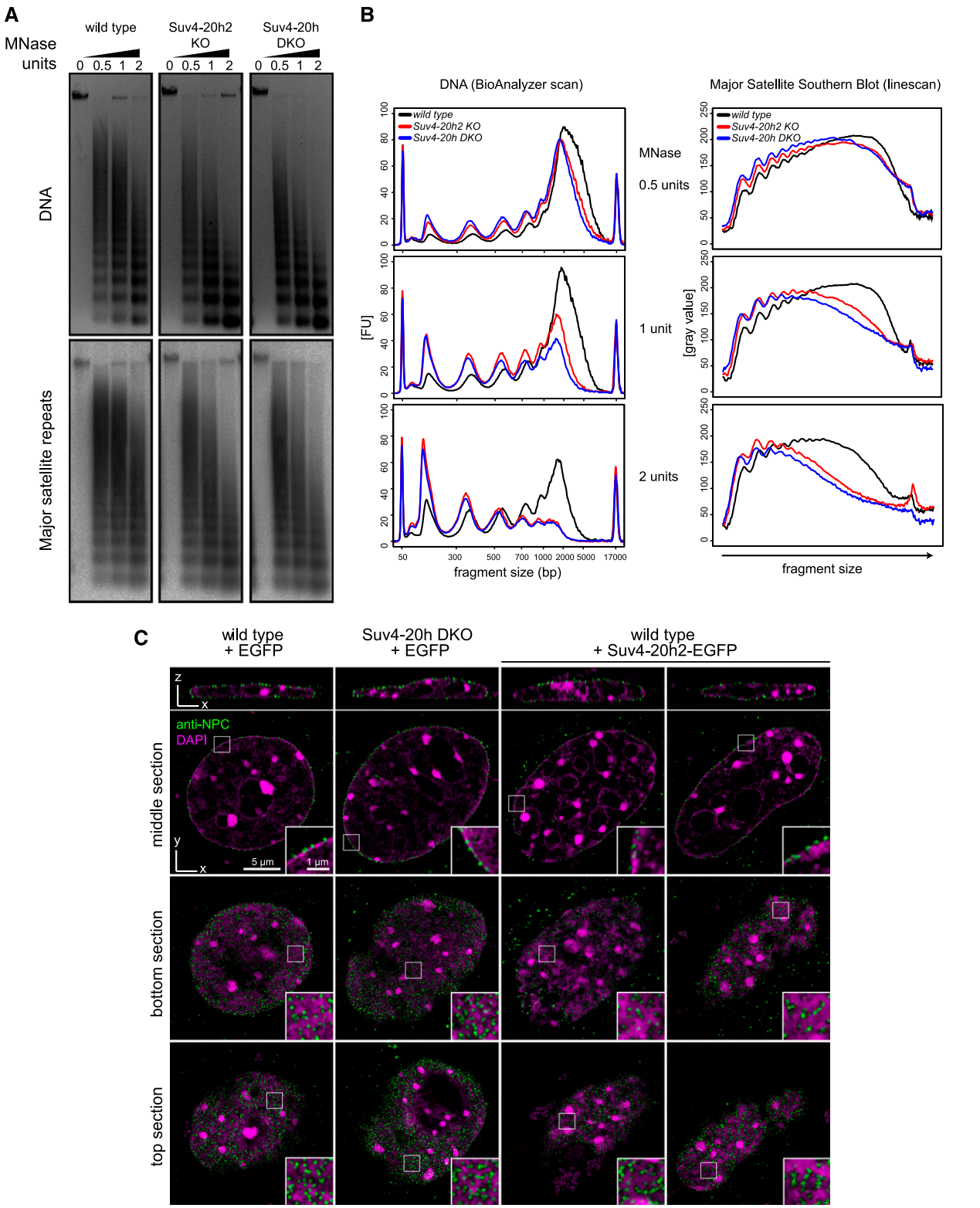

Figure 2. Suv4-20h2 mediates chromatin compaction. (*A*) MNase accessibility assay. Nuclei from wild-type, *Suv4-20h2* knockout, and *Suv4-20h* double-knockout ES cells were isolated and incubated with increasing amounts of MNase. (*Top* panel) The digested DNA was purified, separated on agarose gels, and stained with ethidium bromide. (*Bottom* panel) Heterochromatic regions were visualized by Southern blotting using a major satellite-specific probe. (*B*, *left* panel) Overlay of DNA electropherograms obtained from Bioanalyzer runs of the MNase-digested DNA from wild-type, *Suv4-20h2* knockout, and *Suv4-20h* double-knockout ES cells. The first and the last sharp peaks represent the markers of the Agilent DNA 12000 kit. (FU) Fluorescence units. (*Right* panel) Intensity line scan of major satellite Southern blots. Gray values correspond to signal intensities of the Southern blot. (*C*) 3D-SIM sections of wild-type and *Suv4-20h* double-knockout fibroblasts as well as wild-type cells overexpressing Suv4-20h2-EGFP. Immunofluorescence staining with an anti-NPC antibody marks nuclear pores. *Insets* show enlargements of the nuclear envelope. Quantifications of peripheral heterochromatin density and nuclear pore distribution are shown in Supplemental Figure S6.

reduced in *Suv4-20h* double-knockout cells and increased in cell overexpressing *Suv4-20h2* (Supplemental Fig. S6E).

We further asked which part of Suv4-20h2 would be responsible for the compaction phenotype. Overexpression of the N terminus containing the SET domain does not lead to obvious alterations of the nuclear structure (Supplemental Fig. S7). In contrast, the C terminus of Suv4-20h2 is very potent in inducing chromatin compaction (Supplemental Fig. S7). The Suv4-20h2 clamp domain does not show a compaction phenotype. Interestingly, these data show that Suv4-20h2 has important roles in regulating nuclear architecture, which is independent of its function as a histone methyltransferase.

Chromocenter scattering in Suv4-20h-deficient cells

Our data so far demonstrate that Suv4-20h2 is a major regulator at different levels of chromatin organization in vivo. On the one hand, the observed alterations in chromatin accessibility suggest that Suv4-20h2 regulates compaction of chromatin fibers. On the other hand, the structural changes in *Suv4-20h*-deficient and overexpressing cells indicate that Suv4-20h2 might even mediate long-range interactions between chromatin domains. We therefore investigated whether organization of pericentric heterochromatin is altered in *Suv4-20h* double-knockout cells. In mouse cells, heterochromatic regions of different chromosomes interact and form clusters, which are well discernible by DAPI staining. How this clustering is mediated is unknown. In order to visualize pericentric heterochromatin very precisely, we performed fluorescence in situ hybridization (FISH) detection of major satellite repeats in G0-arrested cells to investigate the steady-state situation of heterochromatin in the absence of cell cycle perturbations (Fig. 3A). Stacks of confocal images were evaluated using an image segmentation procedure to detect and measure individual FISH foci (Supplemental Fig. S8). In wild-type cells, we detected ~25–30 foci (Fig. 3A,B), which is consistent with previous data on chromocenter clustering in mouse fibroblasts (Guenatri et al. 2004). *Suv4-20h* double-knockout cells, in contrast, showed chromocenter scattering, as we observed significantly more foci per nucleus (Fig. 3A,B; Supplemental Fig. S9). At the same time, the average focus volume was smaller in the mutant cells (Fig. 3B). Notably, re-expression of full-length *Suv4-20h2* in *Suv4-20h* double-knockout cells (DKO+FL) restores the altered nuclear organization of pericentric heterochromatin close to wild-type levels (Fig. 3B). Re-expression of the Suv4-20h2 clamp domain (M12) did not lead to a significant rescue (Fig. 3B; Supplemental Fig. S9), suggesting that although the clamp domain of Suv4-20h2 is necessary and sufficient to induce chromatin compaction as measured by MNase accessibility, additional features of the full-length protein are required to mediate long-range chromatin interactions like chromocenter clustering. Therefore, we asked whether chromocenter organization can be restored by a Suv4-20h2 mutant protein lacking methyltransferase activity (Nicetto et al. 2013). Re-expression of Suv4-20h2^{N182A,Y217A} (SET*) could not significantly reduce chromocenter

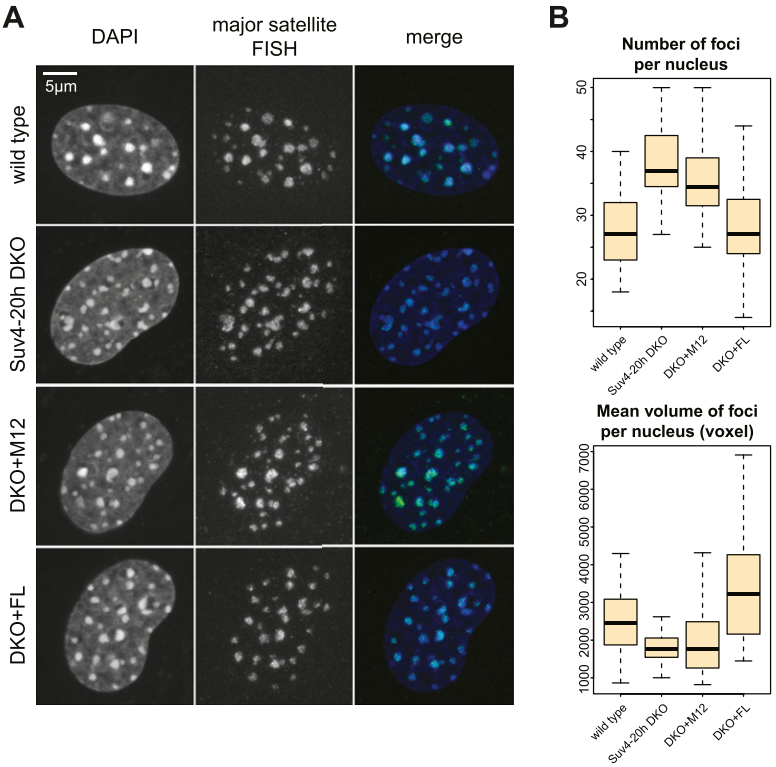

Figure 3. *Suv4-20h*-deficient cells display chromocenter scattering. (*A*) FISH analysis of major satellite repeats in G0-phase wild-type, *Suv4-20h* double-knockout, and *Suv4-20h2* rescue cells expressing Suv4-20h2 full-length protein (DKO+FL) or the Suv4-20h2 clamp domain (DKO+M12). (*B*) Quantification of major satellite FISH analyses. Chromocenter foci were counted and measured using an image segmentation analysis of confocal 3D stacks. Box plots showing the numbers of chromocenters and the chromocenter volume in wild-type (n = 43), *Suv4-20h* double-knockout (n = 35), DKO+FL (n = 28), and DKO+M12 (n = 24) nuclei. The mean number of foci per nucleus is significantly different between wild-type and *Suv4-20h* double-knockout as well as between *Suv4-20h* double-knockout and DKO+FL. Detailed statistical tests are provided in the Supplemental Material and in Supplemental Figure S9.

scattering (Supplemental Fig. S10), indicating that establishment of H4K20me3 is important for normal chromocenter organization.

Based on our data, we propose that Suv4-20h2 can mediate interactions between chromatin fibers by binding to H3K9me3-rich and HP1-rich domains. Loss of Suv4-20h enzymes would lead to a compromised heterochromatin organization, although H3K9me3 and HP1 are still present at heterochromatic regions.

Suv4-20h-deficient cells display chromosome segregation defects

Defects in heterochromatin organization often coincide with genomic instability. Therefore, we examined Suv4-20h mutant cells for chromosome segregation defects by analyzing mitotic figures. Significantly more mitotic abnormalities, such as anaphase bridges and lagging chromosomes, could be observed in the *Suv4-20h* double-knockout cells (Fig. 4A). These defects can be rescued by expression of Suv4-20h2 full-length protein (DKO+FL) and even by expression of the Suv4-20h2 clamp domain (DKO+M12), demonstrating that Suv4-20h2 is important for proper chromosome segregation (Fig. 4A).

An analysis of different mitotic stages revealed that the segregation defects are not due to an altered progression through mitosis (Supplemental Fig. S11). Therefore, we tested whether key checkpoint proteins (AurB and Sgo1) or HP1 were altered in the absence of Suv4-20h enzymes. No obvious difference for either of these proteins was observed. However, we found that the centromere distance, as measured by the distance between adjacent CenpA foci, was wider in *Suv4-20h* double-knockout cells (Fig. 4B). Statistical evaluation confirmed an, on average, 100-nm increased centromere distance in mitotic spreads of *Suv4-20h* double-knockout cells (Fig. 4C).

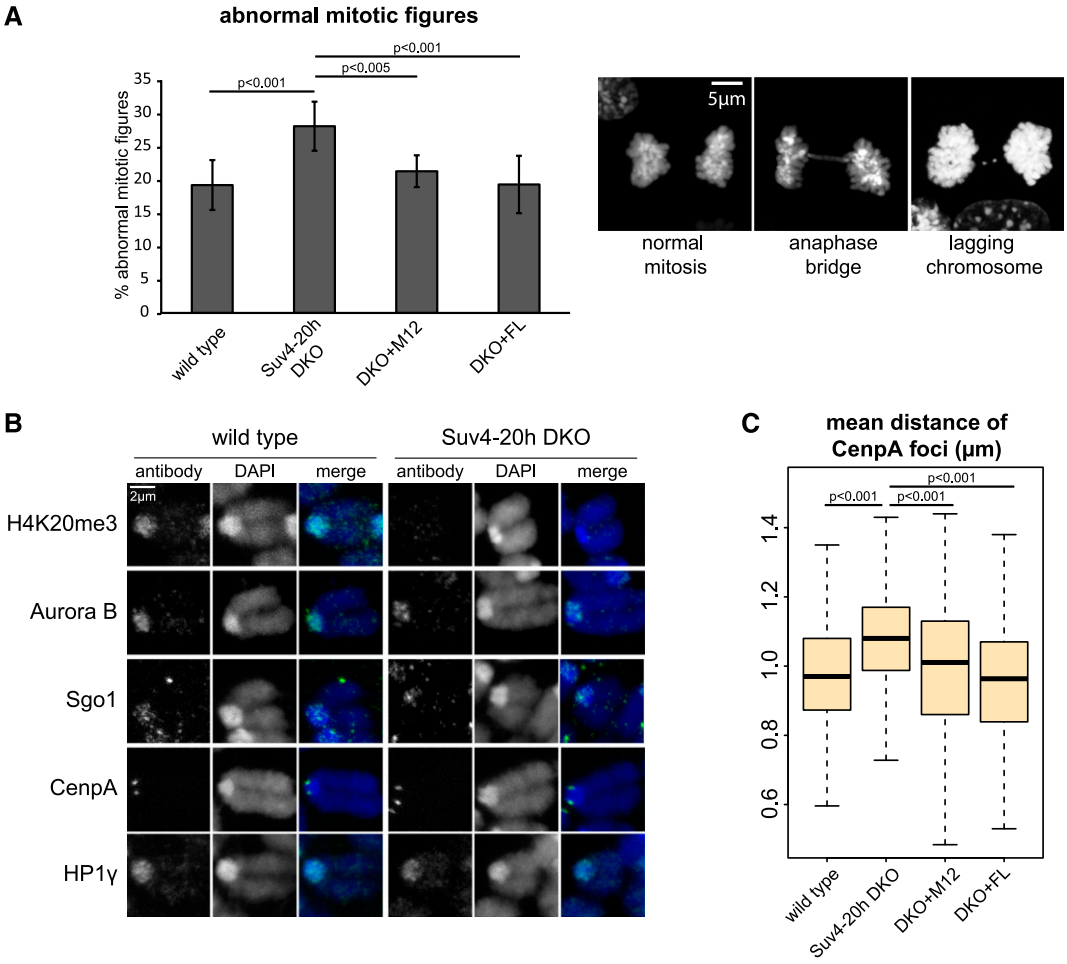

Figure 4. *Suv4-20h* mutants display chromosome segregation defects. (*A*) *Suv4-20h* mutant cells have mitotic chromosome segregation defects. Mitotic cells of wild-type (n = 1497), *Suv4-20h* double-knockout (n = 1242), and rescue MEFs (DKO+FL, n = 768; DKO+M12, n = 687) were assessed for anaphase bridges and lagging chromosomes (the *right* panel shows representative pictures of these defects). *P*-values of Student's *t*-test are indicated. Error bars correspond to standard deviation. (*B*) Mitotic marker analysis. Chromosome spreads of wild-type and *Suv4-20h* double-knockout cells were stained for specific markers that are known to be important for chromosome segregation. Representative pictures of mitotic chromosomes are shown. (*C*) Mean distance of CenpA foci in wild-type (n = 458), *Suv4-20h* double-knockout (n = 348), DKO+FL (n = 242), and DKO+M12 (n = 318) mitotic chromosomes. *P*-values of Student's *t*-test are indicated.

Re-expression of *Suv4-20h2* (DKO+FL) or of the Suv4-20h2 clamp domain (DKO+M12) lead to centromere distances comparable with wild-type cells (Fig. 4C). These data indicate that Suv4-20h2 is important for mediating normal sister chromatid cohesion. Reduced cohesion in *Suv4-20h* double-knockout cells in turn leads to mitotic abnormalities such as lagging chromosomes and anaphase bridges.

Suv4-20h2 interacts with cohesin

We thus hypothesized that in addition to having a structural role in heterochromatin, Suv4-20h2 may recruit additional proteins that facilitate sister chromatid cohesion. We performed GST pull-down assays to identify potential interaction partners of Suv4-20h2 using two different C-terminal truncation proteins (Supplemental Fig. S12A). The first region, M5, comprises the clamp domain, whereas the second fragment, M7, contains the very C terminus that does not localize to heterochromatin (see Fig. 1B). We could clearly precipitate all HP1 isoforms with fragment M5 (Fig. 5A), confirming the direct interaction of HP1 with the Suv4-20h2 clamp domain. Interestingly, additional proteins consistently found to coprecipitate with Suv4-20h2-M5 were subunits of the cohesin complex (Fig. 5A; Supplemental Table S1). The GST pull-down experiments were performed using sonicated nuclear extracts that contain genomic DNA and large chromatin fragments. In order to test whether cohesin indirectly associates with Suv4-20h2 through DNA, we repeated the GST pull-down assays using extracts that were treated with benzonase to degrade all forms of RNA and DNA. Accordingly, extracts treated with benzonase were devoid of any contaminating DNA (Supplemental Fig. S12B). When using benzonase-treated extracts in GST pull-down assays, we clearly detected binding of both HP1 and cohesin subunits to Suv4-20h2-M5 (Fig. 5B). Similar results were obtained when extracts were treated with ethidium bromide, which disrupts DNA–protein interactions (Fig. 5B).

In order to verify that Suv4-20h2 interacts with cohesin subunits in vivo, we performed coimmunoprecipitation experiments using a *Suv4-20h2*$^{HA\text{-}Flag}$ knock-in cell line. In this cell line, the endogenous *Suv4-20h2* locus is modified to produce a HA-3xFlag-tagged fusion protein, ensuring endogenous expression levels (Supplemental Fig. S12C). We developed a two-step extraction protocol to remove the bulk of cohesin through digestion of the DNA with benzonase (fraction I), followed by salt extraction of Suv4-20h2 and the remaining cohesin (fraction II). Flag affinity purification of Suv4-20h2 from fraction II extracts coprecipitated cohesin subunits (Fig. 5C). In the reverse experiment, cohesin subunit Smc1 could coprecipitate Suv4-20h2$^{HA\text{-}Flag}$ (Fig. 5C). We did not detect interaction of unrelated proteins such as Suz12, confirming the specificity of the Suv4-20h2-cohesin interaction. In the pull-down experiments, we found that Suv4-20h2 fragment M5, containing the clamp domain, interacts with cohesin subunits. To test whether the clamp domain is important to mediate interaction with cohesin, we

A

protein	*Suv4-20h2 GST pulldown* GST	M5 (aa 349-441)	M7 (aa 409-468)
Suv4-20h2	4	112	62
HP1α	0	41	0
HP1β	0	40	0
HP1γ	1	40	0
Smc1	0	7	1
Smc3	0	3	0

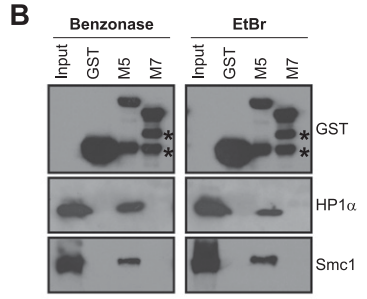

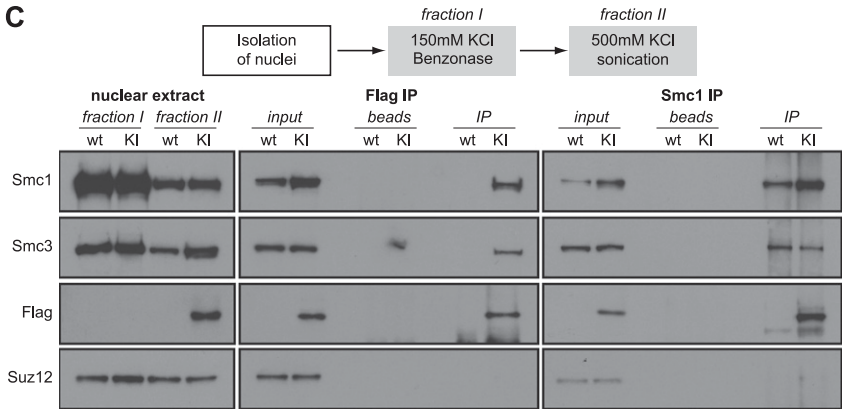

Figure 5. Suv4-20h2 interacts with cohesin subunits. (*A*) GST pull-down of Suv4-20h2 truncation proteins. Suv4-20h2 truncations—heterochromatin-associated (M5) and disperse nuclear (M7)—were expressed as recombinant GST-tagged proteins, incubated with nuclear extracts, and bound to affinity beads. Mass spectrometry identification of bound proteins revealed HP1 isoforms and two cohesin subunits to specifically interact with Suv4-20h2 fragment M5 (summary of triplicate experiments). The number of unique spectra that were identified for each protein in the mass spectrometry analysis is indicated (Scaffold analysis). The full list of identified proteins is shown in Supplemental Table S1. (*B*) GST pull-down experiments. Benzonase-treated nuclear extracts contain no detectable DNA contamination. Ethidium bromide treatment disrupts protein–DNA interactions. Western blots for GST pull-down experiments using recombinant GST, Suv4-20h2-M5, and Suv4-20h2-M7 were probed for GST, HP1α, and Smc1. The Input lane contains the nuclear extract. Degradation products of the GST-tagged proteins are indicated by asterisks. (*C*) Suv4-20h2 and cohesin interact in vivo. Fractionated nuclear extracts were prepared from wild-type (wt) and *Suv4-20h2*$^{HA\text{-}Flag}$ knock-in (KI) ES cells. Suv4-20h2 and Smc1 were precipitated from fraction II extracts using Flag and Smc1 antibodies, respectively. Bound proteins were visualized by Western blotting using Flag, Smc1, Smc3, and Suz12 antibodies.

performed immunoprecipitation experiments in cells expressing full-length *Suv4-20h2* or *Suv4-20h2*-ΔM12, which lacks the clamp domain. We detected interaction of cohesin with full-length Suv4-20h2 but not with Suv4-20h2-ΔM12 (Supplemental Fig. S12D), suggesting that the clamp domain is important to facilitate interaction with cohesin.

Reduced heterochromatin-associated cohesin in Suv4-20h-deficient cells

To test whether Suv4-20h2 plays a role in recruiting cohesin to heterochromatin, we performed chromatin immunoprecipitation (ChIP) experiments for cohesin subunits and tested their enrichment at major satellite repeats and control regions outside of pericentric heterochromatin. In wild-type cells, heterochromatin is enriched for repressive histone modifications (H3K9me3 and H4K20me3) and cohesin subunits (Fig. 6A; Supplemental Fig. S13). Strikingly, in *Suv4-20h* double-knockout cells, cohesin subunits were strongly reduced at major satellite repeats (Fig. 6A; Supplemental Fig. S13) but not at the control regions where cohesin is recruited through different mechanisms (Parelho et al. 2008; Rubio et al. 2008; Wendt et al. 2008). We observed reduced heterochromatin-associated cohesin in two independent *Suv4-20h2*

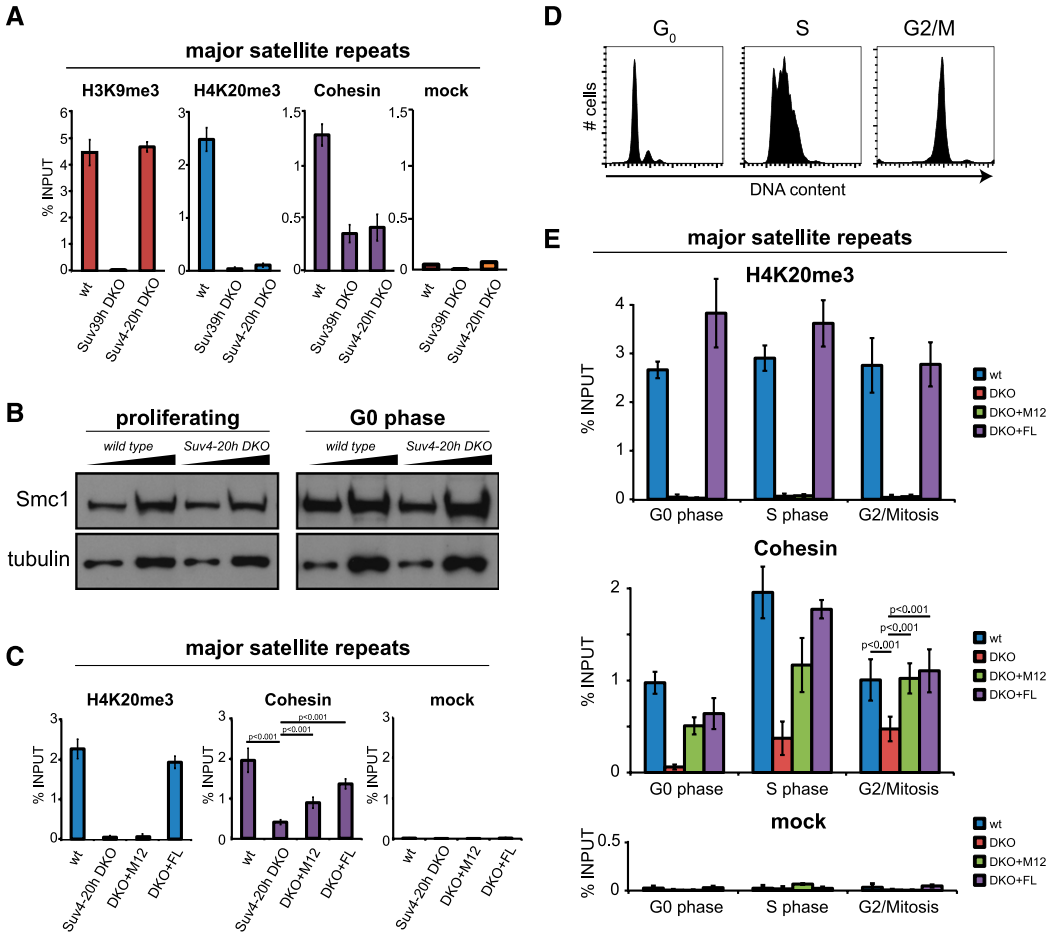

Figure 6. Suv4-20h2 is important for cohesin recruitment to pericentric heterochromatin. (*A*) *Suv39h* double-knockout and *Suv4-20h* double-knockout cells display reduced cohesin levels at pericentric heterochromatin. ChIP analysis of histone modifications and the cohesin subunits Smc3 in wild-type, *Suv39h* double-knockout, and *Suv4-20h* double-knockout cells at major satellite repeats. Merge of two experiments in two independent cell lines with three technical replicates each. Error bars represent standard deviation over all experiments. (*B*) Cohesin levels are not generally impaired in *Suv4-20h* double-knockout cells. Protein extracts of proliferating (*left* panel) or G0-arrested (*right* panel) wild-type and *Suv4-20h* double-knockout cells were tested for cohesin levels by Western blot for Smc1 (cohesin) and tubulin (loading control). Two different amounts of cell extracts were loaded. (*C*) Cohesin establishment can be mediated by the Suv4-20h2 clamp domain. ChIP analysis of H4K20me3 and cohesin (Smc3) at major satellite repeats. Expression of full-length *Suv4-20h2* (DKO+FL) restores H4K20me3 and cohesin in *Suv4-20h* double-knockout cells. Cohesin is partially rescued by expression of the *Suv4-20h2* clamp domain (DKO+M12). Merge of two independent experiments with three technical replicates. Error bars represent standard deviation over all experiments. (*D*) FACS analysis of wild-type cells in G0, S, and M phase. Cells were isolated as described and stained with propidium iodide prior to FACS analysis. (*E*) Suv4-20h enzymes are essential for cohesin recruitment to heterochromatin. Wild-type, *Suv4-20h* double-knockout, and rescue cell lines (DKO+M12 and DKO+FL) were harvested in G0, S, and M phase. ChIP analysis for H3K9me3, H4K20me3, and cohesin (Smc3) at major satellite repeats was performed in two independent experiments with three technical replicates. Error bars represent standard deviation over all experiments.

knockout and two independent *Suv4-20h* double-knockout cell lines (Supplemental Fig. S13). Cohesin levels are not generally reduced in *Suv4-20h* double-knockout cells (Fig. 6B), suggesting specific defects in recruitment of cohesin to heterochromatin. Association of Suv4-20h2 with pericentric heterochromatin depends on Suv39h-mediated H3K9me3 and HP1 association. Therefore, we tested cohesin levels in *Suv39h* double-knockout cells that have lost both H3K9me3 and H4K20me3 at pericentric heterochromatin (Fig. 6A). Importantly, reduced cohesin levels could also be detected in two independent *Suv39h* double-knockout cell lines (Fig. 6A; Supplemental Fig. S14), demonstrating that the Suv39h–Suv4-20h pathway is important for cohesin recruitment to heterochromatin.

We then asked whether Suv4-20h2 is responsible for cohesin recruitment to heterochromatin by rescue experiments in *Suv4-20h* double-knockout cells. Expression of full-length *Suv4-20h2* (DKO+FL) could rescue both cohesin and H4K20me3 at major satellite repeats (Fig. 6C). Interestingly, the *Suv4-20h2* clamp domain (DKO+M12) could also increase cohesin levels at heterochromatin, although this truncation protein lacks the SET domain and thus was unable to restore H4K20me3 (Fig. 6C). Cohesin at control regions was not affected in the different rescue experiments (Supplemental Fig. S15). We conclude that Suv4-20h2 plays an important role in recruiting cohesin to heterochromatic regions through interactions with cohesin subunits.

Suv4-20h2 is important for the initial recruitment of cohesin to pericentric heterochromatin

Finally, we investigated whether Suv4-20h2 is involved in the initial recruitment/maintenance of cohesin at heterochromatin. Loading of cohesin onto chromatin occurs in early G1 phase (Watrin et al. 2006). In the subsequent cell cycle stages, cohesin is maintained on the chromosomes until mitosis. During metaphase, cohesin is removed from chromosome arms by proteolytic cleavage (Hauf et al. 2001). Only cohesin at pericentric heterochromatin is maintained until the onset of anaphase to ensure sister chromatid cohesion (Salic et al. 2004; Tang et al. 2004). In order to investigate whether Suv4-20h2 is implicated in cohesin loading or maintenance, we analyzed cohesin levels in different cell cycle stages. We synchronized cells in G0, S, and G2/M phase (Fig. 6D; Supplemental Fig. S16) and prepared chromatin for ChIP analysis. We found that cohesin levels varied only slightly over the cell cycle in wild-type cells (Fig. 6E). In contrast, in *Suv4-20h* double-knockout cells, cohesin was basically absent from heterochromatic regions in G0 phase, suggesting that Suv4-20h enzymes are crucial for loading and/or maintaining cohesin at heterochromatin. At later stages in the cell cycle (S and G2/M phase), cohesin levels increased (Fig. 6E), indicating that additional, Suv4-20h-independent recruitment mechanisms exist during S phase. The loss of heterochromatin-associated cohesin in *Suv4-20h* double-knockout cells could be rescued by expressing the clamp domain (M12) or full-length Suv4-20h2 (Fig. 6E), whereas cohesin recruitment at unrelated control regions was not affected in the rescue cells (Supplemental Fig. S17). Thus, our data demonstrate that Suv4-20h2 is an important factor for cohesin loading onto heterochromatin.

Discussion

Heterochromatin is a very abundant chromatin state in mammalian cells, as >30% of the mammalian genome is composed of repetitive sequences that need to be silenced. Heterochromatin is therefore characterized by low transcriptional activity and features a less accessible chromatin structure. These special properties of heterochromatin are established in a step-wise manner. First, specific proteins need to recognize heterochromatic sequences (Bulut-Karslioglu et al. 2012). Second, heterochromatin becomes marked with distinct histone modifications that recruit additional binding proteins to ultimately mediate the special properties of this chromatin state. In vivo, heterochromatin is not a stiff entity, but rather a dynamic equilibrium of a protein interaction network. Thus, it can both reduce chromatin accessibility under steady-state conditions and open up chromatin structure in response to specific stimuli; for example, DNA damage (Goodarzi et al. 2008). Here we demonstrate that Suv4-20h2 is an important constituent of this interaction network for regulating chromatin accessibility and long-range chromatin interactions. In ES cells and fibroblasts, these functions do not seem to be shared with Suv4-20h1, which features a different heterochromatin targeting domain that is not homologous to the Suv4-20h2 clamp domain and does not bind so tightly to heterochromatin (Supplemental Fig. S18A).

How is Suv4-20h2 integrated into this network and how can it affect heterochromatin structure? Heterochromatin displays abundant H3K9me3, which provides a binding interface for HP1 proteins. Although HP1 shows only a weak affinity to H3K9me3 in vitro, the high density of H3K9me3 can lead to a high HP1 abundance in heterochromatin. We found that Suv4-20h2 features multiple HP1 interaction sites in its clamp domain, which can explain its stable association with regions that feature high HP1 concentrations. The interaction with multiple HP1 proteins raises an interesting hypothesis that Suv4-20h2 might bridge H3K9me3- and HP1-rich chromatin fibers to render chromatin less accessible. In agreement with this view, we found that chromatin in cells lacking *Suv4-20h2* is indeed more accessible to nucleases. Notably, the level of Suv4-20h2 can alter the balance within the heterochromatin interaction network and may therefore modulate the functions of its interacting proteins, like HP1. Another protein that may be affected by Suv4-20h2 is the linker histone H1. This is inferred by the observed alterations in the nucleosome repeat length in *Suv4-20h* double-knockout cells (Fig. 2B), which is a typical feature of cells with reduced levels of histone H1 (Fan et al. 2005). The current knowledge of the topology of the heterochromatin interaction network is insufficient to distinguish direct effects from indirect effects. However, our data demonstrate that Suv4-20h2

is a central node within this network, and therefore changes of Suv4-20h2 levels lead to drastic alterations in nuclear architecture.

Interestingly, the clamp domain of Suv4-20h2 is necessary and sufficient for chromatin compaction, as *Suv4-20h* double-knockout cells expressing this domain display normal chromatin accessibility. However, the clamp domain is not sufficient to mediate long-range chromatin interactions and condensation of large chromatin domains. Therefore, other domains in Suv4-20h2, such as an active SET domain, or recruitment of additional proteins are required for these functions. An intriguing possibility is that heterochromatin-associated cohesin, which is recruited by Suv4-20h2, is implicated in these long-range interactions (Hadjur et al. 2009; Kagey et al. 2010; Degner et al. 2011). Recent evidence suggests that cohesin may be involved in regulating the condensation of heterochromatic domains. Cohesin is present in a balance between a chromatin-associated form and a free form that is adjusted by a loading–releasing cycle (Kueng et al. 2006; Gause et al. 2010). Perturbation of this balance by knockdown of the cohesin-releasing factor WAPL leads to increased cohesin association with chromatin and a dramatic chromatin compaction phenotype (Seitan and Merkenschlager 2012). However, we could not detect significant perturbations in chromocenter organization in cells lacking the cohesin subunit Scc1/Rad21 (Supplemental Fig. S19). Therefore, we expect that other proteins that interact with Suv4-20h2 outside of the clamp domain are necessary to mediate chromocenter clustering.

Although cohesin appears to be dispensable for nuclear architecture in interphase cells, heterochromatin-associated cohesin is absolutely crucial for sister chromatid cohesion during mitosis. How cohesin is loaded onto chromatin and how the cohesin ring stabilizes interactions between chromatids are currently unclear (Nasmyth 2011). We found that the Suv39h–Suv4-20h pathway is important for the loading of cohesin to pericentric heterochromatin (Fig. 7). Our data are consistent with a study demonstrating that *Suv39h*-deficient cells display defects in sister chromatid cohesion and chromosome segregation (Koch et al. 2008). Although Koch et al. (2008) could not demonstrate that cohesin levels in *Suv39h* double-knockout cells were reduced, this may be due to their semiquantitative ChIP analysis, which is not suitable for highly repetitive sequences. We clearly detected reduced cohesin levels at major satellite repeats in different *Suv39h* double-knockout, *Suv4-20h* double-knockout, and *Suv4-20h2* knockout cell lines. In none of these cell lines, cohesin was completely lost from heterochromatin, suggesting additional loading pathways. Based on our data, we conclude that the primary function of Suv39h enzymes is to prepare pericentric heterochromatin for HP1 recruitment, which is a prerequisite for stable association of Suv4-20h2. Cohesion recruitment is then facilitated through interactions of cohesin subunits with Suv4-20h2 and possibly additional factors. Suv4-20h1 does not interact with cohesin and is therefore unlikely to contribute to cohesin recruitment (Supplemental Fig. S18C). Interestingly, cohesin recruitment can be mediated at least partially through the Suv4-20h2 clamp domain. As this domain can interact with cohesin and also induce chromatin compaction, it is not possible to distinguish which of the two functions is more relevant for cohesin recruitment to heterochromatin.

The cell cycle analysis revealed that Suv4-20h2 is essential for cohesin loading in G0 phase. During later stages of the cell cycle, Suv4-20h2-independent pathways can recruit cohesin to heterochromatin. This would explain why mitosis is not completely blocked and why comparably mild mitotic phenotypes were detected in *Suv4-20h*-deficient cells. Importantly, our data are consistent with other reports that demonstrate that the fidelity of mitosis is already compromised when heterochromatin-associated cohesin levels are only reduced (Eckert et al. 2007). A low level of mitotic defects can therefore ensure survival of the cells but contributes to genomic instability.

Dysregulation of pericentric heterochromatin has been suggested to play important roles in cancer development and progression (Hahn et al. 2010; Zhu et al. 2011). Cancer cells are frequently characterized by genomic instability and cohesion defects (Thompson et al. 2010), but the mechanisms are still poorly understood. Previous analyses have shown that a reduced level of H4K20me3, which is an indirect measure for the presence of Suv4-20h enzymes, characterizes different human tumors (Fraga et al. 2005). In light of our data, we hypothesize that Suv4-20h2 might be an important cohesin recruitment factor in human cells. Its dysregulation could lead to reduced levels of heterochromatin-associated cohesin, which in turn contributes to the genomic instability that is characteristic of many human tumors and could explain the negative survival prognosis with tumors that have low H4K20me3 levels (Van Den Broeck et al. 2008; Schneider et al. 2011).

Materials and methods

FRAP

FRAP measurements were performed in MEF and ES cell lines after transient expression of EGFP-tagged proteins. Analysis of the recovery curves of the intensity integrated over the region of interest (ROI) was done using FREDIS software (Muller et al. 2009). For Figure 1, the averaged recovery curves were fitted to a diffusion model or a reaction diffusion model that incorporates both diffusion and binding processes.

HP1 interaction test

GST fusion proteins of Suv4-20h2, HP1α, HP1β, and HP1γ were expressed in *Escherichia coli* and purified using glutathione-S-sepharose beads (Amersham Biosciences). The GST tag was subsequently removed using PreScission protease. Interaction tests were performed by incubating 5 μg of GST-Suv4-20h2 fusion protein with 5 μg of either HP1α, HP1β, or HP1γ for 1 h at room temperature on a rotating wheel.

Chromatin accessibility assay

Nuclei of wild-type, *Suv4-20h2* knockout, and *Suv4-20h2* double-knockout ES cells and wild-type, *Suv4-20h* double-knockout,

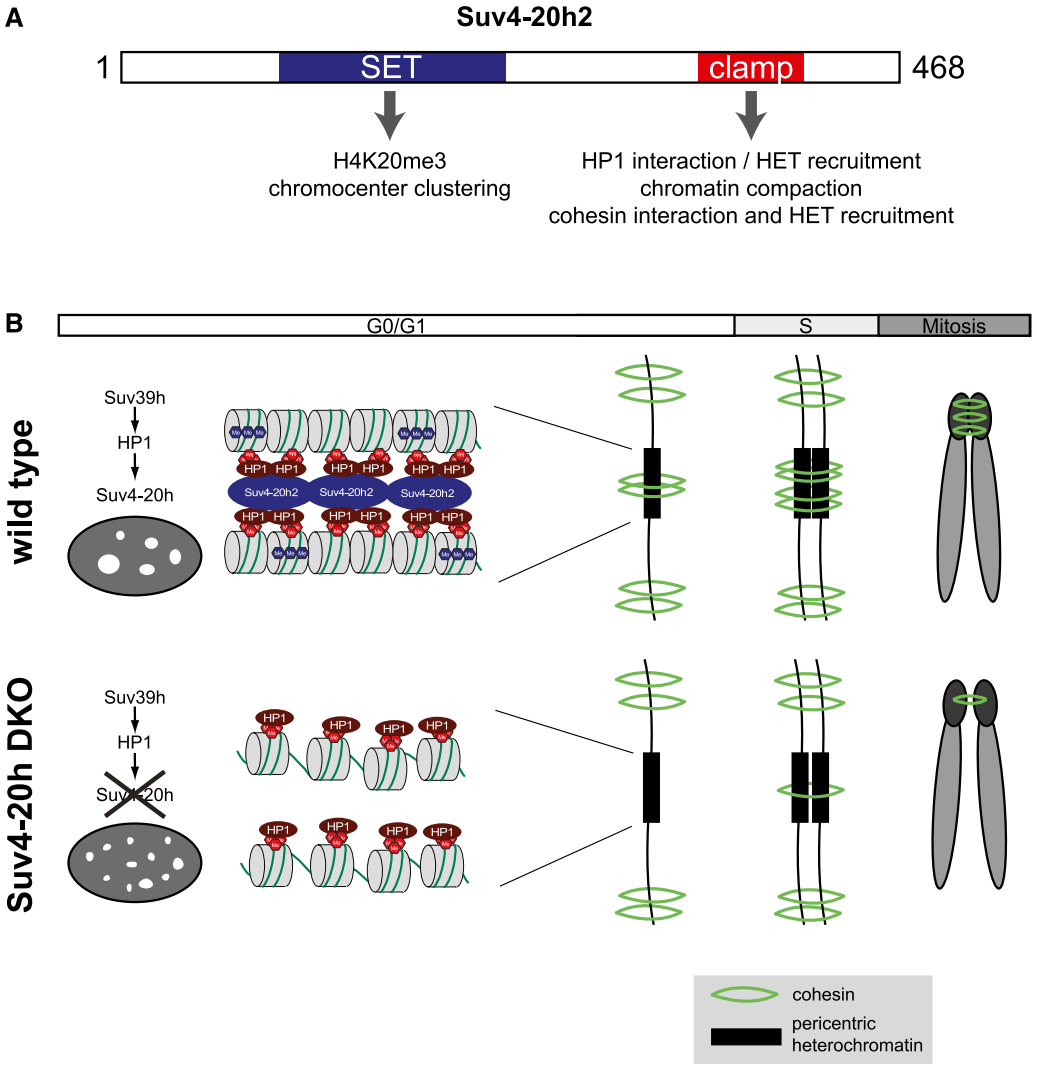

Figure 7. Model for Suv4-20h2-mediated chromatin compaction. (*A*) Functional domains in Suv4-20h2. The SET domain is the catalytic domain that induces H4K20me3. Establishing this modification is important to mediate chromocenter clustering. The clamp domain is essential to recruit Suv4-20h2 to pericentric heterochromatin. The clamp domain also mediates the Suv4-20h2-cohesin interaction and thus the recruitment of cohesin to heterochromatin. (*B*) Model showing the role of the Suv39h–HP1–Suv4-20h pathway for chromatin compaction and cohesin recruitment to pericentric heterochromatin. Based on our data, we propose that Suv4-20h2 can mediate interactions between chromatin fibers by binding to H3K9me3-rich and HP1-rich domains. The loss of Suv4-20h enzymes leads to a compromised heterochromatin organization (reduced chromatin compaction and chromocenter scattering) although H3K9me3 and HP1 are still present at heterochromatic regions. In G0/G1 cells, the interaction with Suv4-20h2 is important for cohesin recruitment to pericentric heterochromatin. Cohesin is not completely lost from mitotic chromosomes due to alternative, Suv4-20h-independent loading pathways during S/G2 phase.

DKO+FL, and DKO+M12 fibroblast cell lines were digested with different amounts of MNase (Sigma) according to Gilbert et al. (2007). Genomic DNA was purified and separated on a 1% agarose gel or loaded onto a DNA LabChip (Agilent Technologies).

3D-SIM

Superresolution 3D-SIM of immunofluorescently labeled and DAPI-stained nuclei was performed as previously described (Schermelleh et al. 2008) on a DeltaVision OMX V3 system (Applied Precision) equipped with a 100×/1.40 NA PlanApo oil immersion objective (Olympus) and Cascade II:512 EMCCD cameras (Photometrics) using 405-nm and 592-nm diode laser.

Mitotic abnormalities

To quantify the number of abnormal mitotic figures in MEF cells, mitotic cells were collected by shake-off, spun onto a glass-bottomed 96-black well plate (Greiner Bio-One) for 5 min at 400*g*, fixed in 4% formaldehyde, and stained with VectaShield containing DAPI.

Coimmunoprecipitation

Nuclei of wild-type and *Suv4-20h2*$^{HA\text{-}Flag}$ ES cells were sequentially extracted with low-salt (fraction I) and high-salt (fraction II) immunoprecipitation buffer and incubated with 5 μg of either

Flag M2 antibody (Sigma) or Smc1 antibody (Bethyl Laboratories) coupled to ProteinA/G magnetic beads (Dynabeads, Invitrogen) overnight at 4°C on a rotating wheel. Bound proteins were separated on SDS–polyacrylamide gels and analyzed by Western blotting.

ChIP

ChIP experiments were performed as in Samoshkin et al. (2012) using the following antibodies: anti-H3K9me3 (Abcam, #ab8898), anti-H4K20me3 (Active Motif, #39180.3918; or Millipore, #07-463), anti-Rad21 (Abcam, #ab992), and anti-Smc3 (Abcam, #ab9263).

Automatic 3D quantification of FISH foci

Major satellite FISH experiments were performed according to Markaki et al. (2013). To determine quantitative information of FISH major satellite repeats from the acquired two-channel 3D confocal microscopy images, we developed a fully automatic 3D image analysis approach consisting of 3D cell nuclei segmentation and 3D foci segmentation.

Acknowledgments

We thank Alexander Nuber for technical help. We are grateful to Thomas Cremer for sending major satellite FISH probes and protocols. We thank Jan-Michael Peters for sending antibodies, and Matthias Merkenschlager for sharing the Scc1 conditional knockout cell lines. We are indebted to Jerome Dejardin for discussions and sharing unpublished data. The work of G.S., K. Rippe, H.L., and K. Rohr was funded by the BMBF project EpiSys in the SysTec program. Additional support was from the Deutsche Forschungsgemeinschaft (SFB-TR5 and SFB684) to L.S., H.L., and G.S. H.v.M. was supported by the Fritz Thyssen Stiftung (AZ. 10.05.1.165).

References

Bulut-Karslioglu A, Perrera V, Scaranaro M, de la Rosa-Velazquez IA, van de Nobelen S, Shukeir N, Popow J, Gerle B, Opravil S, Pagani M, et al. 2012. A transcription factor-based mechanism for mouse heterochromatin formation. *Nat Struct Mol Biol* **19:** 1023–1030.

Cheutin T, McNairn AJ, Jenuwein T, Gilbert DM, Singh PB, Misteli T. 2003. Maintenance of stable heterochromatin domains by dynamic HP1 binding. *Science* **299:** 721–725.

Degner SC, Verma-Gaur J, Wong TP, Bossen C, Iverson GM, Torkamani A, Vettermann C, Lin YC, Ju Z, Schulz D, et al. 2011. CCCTC-binding factor (CTCF) and cohesin influence the genomic architecture of the Igh locus and antisense transcription in pro-B cells. *Proc Natl Acad Sci* **108:** 9566–9571.

Eckert CA, Gravdahl DJ, Megee PC. 2007. The enhancement of pericentromeric cohesin association by conserved kinetochore components promotes high-fidelity chromosome segregation and is sensitive to microtubule-based tension. *Genes Dev* **21:** 278–291.

Fan Y, Nikitina T, Zhao J, Fleury TJ, Bhattacharyya R, Bouhassira EE, Stein A, Woodcock CL, Skoultchi AI. 2005. Histone H1 depletion in mammals alters global chromatin structure but causes specific changes in gene regulation. *Cell* **123:** 1199–1212.

Fraga MF, Ballestar E, Villar-Garea A, Boix-Chornet M, Espada J, Schotta G, Bonaldi T, Haydon C, Ropero S, Petrie K, et al. 2005. Loss of acetylation at Lys16 and trimethylation at Lys20 of histone H4 is a common hallmark of human cancer. *Nat Genet* **37:** 391–400.

Gause M, Misulovin Z, Bilyeu A, Dorsett D. 2010. Dosage-sensitive regulation of cohesin chromosome binding and dynamics by Nipped-B, Pds5, and Wapl. *Mol Cell Biol* **30:** 4940–4951.

Gilbert N, Thomson I, Boyle S, Allan J, Ramsahoye B, Bickmore WA. 2007. DNA methylation affects nuclear organization, histone modifications, and linker histone binding but not chromatin compaction. *J Cell Biol* **177:** 401–411.

Goodarzi AA, Noon AT, Deckbar D, Ziv Y, Shiloh Y, Lobrich M, Jeggo PA. 2008. ATM signaling facilitates repair of DNA double-strand breaks associated with heterochromatin. *Mol Cell* **31:** 167–177.

Guenatri M, Bailly D, Maison C, Almouzni G. 2004. Mouse centric and pericentric satellite repeats form distinct functional heterochromatin. *J Cell Biol* **166:** 493–505.

Hadjur S, Williams LM, Ryan NK, Cobb BS, Sexton T, Fraser P, Fisher AG, Merkenschlager M. 2009. Cohesins form chromosomal *cis*-interactions at the developmentally regulated IFNG locus. *Nature* **460:** 410–413.

Hahn M, Dambacher S, Schotta G. 2010. Heterochromatin dysregulation in human diseases. *J Appl Physiol* **109:** 232–242.

Hauf S, Waizenegger IC, Peters JM. 2001. Cohesin cleavage by separase required for anaphase and cytokinesis in human cells. *Science* **293:** 1320–1323.

Kagey MH, Newman JJ, Bilodeau S, Zhan Y, Orlando DA, van Berkum NL, Ebmeier CC, Goossens J, Rahl PB, Levine SS, et al. 2010. Mediator and cohesin connect gene expression and chromatin architecture. *Nature* **467:** 430–435.

Koch B, Kueng S, Ruckenbauer C, Wendt KS, Peters JM. 2008. The Suv39h–HP1 histone methylation pathway is dispensable for enrichment and protection of cohesin at centromeres in mammalian cells. *Chromosoma* **117:** 199–210.

Kueng S, Hegemann B, Peters BH, Lipp JJ, Schleiffer A, Mechtler K, Peters JM. 2006. Wapl controls the dynamic association of cohesin with chromatin. *Cell* **127:** 955–967.

Lengronne A, Katou Y, Mori S, Yokobayashi S, Kelly GP, Itoh T, Watanabe Y, Shirahige K, Uhlmann F. 2004. Cohesin relocation from sites of chromosomal loading to places of convergent transcription. *Nature* **430:** 573–578.

Markaki Y, Smeets D, Cremer M, Schermelleh L. 2013. Fluorescence in situ hybridization applications for super-resolution 3D structured illumination microscopy. *Methods Mol Biol* **950:** 43–64.

Meshorer E, Yellajoshula D, George E, Scambler PJ, Brown DT, Misteli T. 2006. Hyperdynamic plasticity of chromatin proteins in pluripotent embryonic stem cells. *Dev Cell* **10:** 105–116.

Muller KP, Erdel F, Caudron-Herger M, Marth C, Fodor BD, Richter M, Scaranaro M, Beaudouin J, Wachsmuth M, Rippe K. 2009. Multiscale analysis of dynamics and interactions of heterochromatin protein 1 by fluorescence fluctuation microscopy. *Biophys J* **97:** 2876–2885.

Nasmyth K. 2011. Cohesin: A catenase with separate entry and exit gates? *Nat Cell Biol* **13:** 1170–1177.

Nicetto D, Hahn M, Jung J, Schneider TD, Straub T, David R, Schotta G, Rupp RA. 2013. Suv4-20h histone methyltransferases promote neuroectodermal differentiation by silencing the pluripotency-associated oct-25 gene. *PLoS Genet* **9:** e1003188.

Nonaka N, Kitajima T, Yokobayashi S, Xiao G, Yamamoto M, Grewal SI, Watanabe Y. 2002. Recruitment of cohesin to heterochromatic regions by Swi6/HP1 in fission yeast. *Nat Cell Biol* **4:** 89–93.

Parelho V, Hadjur S, Spivakov M, Leleu M, Sauer S, Gregson HC, Jarmuz A, Canzonetta C, Webster Z, Nesterova T, et al. 2008. Cohesins functionally associate with CTCF on mammalian chromosome arms. *Cell* **132:** 422–433.

Peters AH, O'Carroll D, Scherthan H, Mechtler K, Sauer S, Schofer C, Weipoltshammer K, Pagani M, Lachner M, Kohlmaier A, et al. 2001. Loss of the Suv39h histone methyltransferases impairs mammalian heterochromatin and genome stability. *Cell* **107:** 323–337.

Rubio ED, Reiss DJ, Welcsh PL, Disteche CM, Filippova GN, Baliga NS, Aebersold R, Ranish JA, Krumm A. 2008. CTCF physically links cohesin to chromatin. *Proc Natl Acad Sci* **105:** 8309–8314.

Salic A, Waters JC, Mitchison TJ. 2004. Vertebrate shugoshin links sister centromere cohesion and kinetochore microtubule stability in mitosis. *Cell* **118:** 567–578.

Samoshkin A, Dulev S, Loukinov D, Rosenfeld JA, Strunnikov AV. 2012. Condensin dysfunction in human cells induces nonrandom chromosomal breaks in anaphase, with distinct patterns for both unique and repeated genomic regions. *Chromosoma* **121:** 191–199.

Schermelleh L, Carlton PM, Haase S, Shao L, Winoto L, Kner P, Burke B, Cardoso MC, Agard DA, Gustafsson MG, et al. 2008. Subdiffraction multicolor imaging of the nuclear periphery with 3D structured illumination microscopy. *Science* **320:** 1332–1336.

Schneider AC, Heukamp LC, Rogenhofer S, Fechner G, Bastian PJ, von Ruecker A, Muller SC, Ellinger J. 2011. Global histone H4K20 trimethylation predicts cancer-specific survival in patients with muscle-invasive bladder cancer. *BJU Int* **108:** E290–E296.

Schotta G, Lachner M, Sarma K, Ebert A, Sengupta R, Reuter G, Reinberg D, Jenuwein T. 2004. A silencing pathway to induce H3-K9 and H4-K20 trimethylation at constitutive heterochromatin. *Genes Dev* **18:** 1251–1262.

Schotta G, Sengupta R, Kubicek S, Malin S, Kauer M, Callen E, Celeste A, Pagani M, Opravil S, De La Rosa-Velazquez IA, et al. 2008. A chromatin-wide transition to H4K20 monomethylation impairs genome integrity and programmed DNA rearrangements in the mouse. *Genes Dev* **22:** 2048–2061.

Seitan VC, Merkenschlager M. 2012. Cohesin and chromatin organisation. *Curr Opin Genet Dev* **22:** 93–100.

Souza PP, Volkel P, Trinel D, Vandamme J, Rosnoblet C, Heliot L, Angrand PO. 2009. The histone methyltransferase SUV420H2 and heterochromatin proteins HP1 interact but show different dynamic behaviours. *BMC Cell Biol* **10:** 41.

Tang Z, Sun Y, Harley SE, Zou H, Yu H. 2004. Human Bub1 protects centromeric sister-chromatid cohesion through Shugoshin during mitosis. *Proc Natl Acad Sci* **101:** 18012–18017.

Thompson SL, Bakhoum SF, Compton DA. 2010. Mechanisms of chromosomal instability. *Curr Biol* **20:** R285–R295.

Ting DT, Lipson D, Paul S, Brannigan BW, Akhavanfard S, Coffman EJ, Contino G, Deshpande V, Iafrate AJ, Letovsky S, et al. 2011. Aberrant overexpression of satellite repeats in pancreatic and other epithelial cancers. *Science* **331:** 593–596.

Van Den Broeck A, Brambilla E, Moro-Sibilot D, Lantuejoul S, Brambilla C, Eymin B, Khochbin S, Gazzeri S. 2008. Loss of histone H4K20 trimethylation occurs in preneoplasia and influences prognosis of non-small cell lung cancer. *Clin Cancer Res* **14:** 7237–7245.

Vermeulen M, Eberl HC, Matarese F, Marks H, Denissov S, Butter F, Lee KK, Olsen JV, Hyman AA, Stunnenberg HG, et al. 2010. Quantitative interaction proteomics and genome-wide profiling of epigenetic histone marks and their readers. *Cell* **142:** 967–980.

Watrin E, Schleiffer A, Tanaka K, Eisenhaber F, Nasmyth K, Peters JM. 2006. Human Scc4 is required for cohesin binding to chromatin, sister-chromatid cohesion, and mitotic progression. *Curr Biol* **16:** 863–874.

Wendt KS, Yoshida K, Itoh T, Bando M, Koch B, Schirghuber E, Tsutsumi S, Nagae G, Ishihara K, Mishiro T, et al. 2008. Cohesin mediates transcriptional insulation by CCCTC-binding factor. *Nature* **451:** 796–801.

Zhu Q, Pao GM, Huynh AM, Suh H, Tonnu N, Nederlof PM, Gage FH, Verma IM. 2011. BRCA1 tumour suppression occurs via heterochromatin-mediated silencing. *Nature* **477:** 179–184.

SUPPLEMENTAL DATA

Figure S1. FRAP analysis of heterochromatin core proteins.

(A) Heterochromatin is marked by two prominent histone modifications, H3K9me3 and H4K20me3. Suv39h enzymes are recruited by currently unknown mechanisms to pericentric heterochromatin and induce H3K9me3. This modification is then bound by HP1 proteins. Suv4-20h proteins bind to heterochromatin in an HP1-dependent manner and induce H4K20me3. (B) FRAP analysis in wild type fibroblast cells expressing HP1α-EGFP or Suv4-20h2-EGFP. Red circle marks the bleached region which corresponds to pericentric heterochromatin.

Figure S2. Mobility of Suv4-20h2 at endogenous expression level

(A) *Suv4-20h2* knock-in strategy to express C-terminally tagged Suv4-20h2-EGFP from the endogenous locus. The region of the targeting construct is shown as bold line. After homologous recombination, exon 8 contains an insertion of the EGFP open reading frame just before the regular STOP codon, followed by a neomycin resistance cassette. (B) Western blot of *Suv4-20h2*^{EGFP} and wild type ES cells using an antibody specifically recognizing Suv4-20h2 (Dambacher et al. 2012). (C) Confocal microscopy section of *Suv4-20h2*^{EGFP} knock-in cells. The EGFP-tagged Suv4-20h2 is clearly enriched at pericentric heterochromatin, together with H4K20me3. (D) Quantification of the transiently bound pool Suv4-20h2 and HP1 isoforms via FCS in terms of the apparent diffusion coefficient. (E) Immobile fraction of Suv4-20h2 and HP1β as measured by continuous photobleaching. (F) Western blot of wild type fibroblast cells which were transiently transfected with EGFP-tagged *Suv4-20h2* truncations. Due to variations in transfection efficiency the expression levels of the different truncations cannot be directly compared. The minus sign (-) denotes an empty lane.

Figure S3. *In vivo* HP1 interaction test.

BHK cells containing a *lac* operator repeat array were co-transfected with expression vectors for lacR-GBP, Suv4-20h2-EGFP and HP1 isoforms as mCherry fusions. The lacR-GBP fusion protein binds to the lac operator array and recruits Suv4-20h2-EGFP. All HP1 isoforms interact with Suv4-20h2 in vivo and show co-localization at the lac operator arrays. Histograms display the percentage of cells where HP1 proteins co-localize with EGFP and Suv4-20h2-EGFP, respectively.

Figure S4. HP1α knock-out cells display normal heterochromatin marks.

(A) Wild type and HP1α KO MEFs were stained for HP1α, H3K9me3 and H4K20me3. HP1α is not detectable in the HP1α KO cells. H3K9me3 and H4K20me3 are enriched at heterochromatin in both wild type and mutant cells (scale bars, 5μm). (B) Localization of Suv4-20h2 truncation proteins in HP1α KO cells. Confocal sections of HP1α KO fibroblasts expressing EGFP-tagged Suv4-20h2 truncations are shown (scale bars, 5μm).

Figure S5. Suv4-20h2 mediates chromatin compaction.

(A) MNase accessibility assay using fibroblast cell lines. Nuclei from wild type, *Suv4-20h2* DKO and rescue cells expressing full length *Suv4-20h2* (DKO+FL) or *Suv4-20h2*-M12 (DKO+M12) were isolated and incubated with increasing amounts of MNase. The digested DNA was purified, separated on agarose gels and stained with ethidium bromide (upper panel). Heterochromatic regions were visualized by Southern blotting using a major satellite-specific probe (lower panel). (B) Overlay of DNA electropherograms obtained from Bioanalyzer runs of the MNase-digested DNA from wild type, *Suv4-20h2* DKO and rescue cells (left panel). The first and the last sharp peak represent the markers of the Agilent DNA 12000 kit (FU = fluorescence units). Intensity linescan of major satellite Southern blots (right panel). Gray values correspond to signal intensities of the southern blot.

Figure S6. Reduced peripheral heterochromatin and altered arrangement of nuclear pores in *Suv4-20h* DKO cells.

(A) 3D-SIM analysis of nuclear structure (DAPI) was performed in wild type, *Suv4-20h* DKO and wild type cells over-expressing *Suv4-20h2*. Inserts are enlargements of the nuclear periphery. (B) Nuclear periphery of central sections of the 3D-SIM images was automatically segmented to measure DAPI intensities. Example images for segmented wild type and *Suv4-20h* DKO nuclei are shown. The area highlighted in blue was used to measure the DAPI intensity of peripheral heterochromatin. (C) The relative intensities of peripheral heterochromatin were calculated over several 3D-SIM images as ratio of peripheral DAPI intensity vs. total nuclear DAPI intensity. The P values of Student's t-test are indicated. (D) Automated 3D image analysis of nuclear pores. 3D-SIM images were automatically segmented based on the DAPI channel to identify the nucleus and the anti-NUP staining to identify nuclear pores. Image shows an example wild type nucleus as 3D visualization of the segmentation result. Black spots – nuclear pores on the top surface; gray spots – nuclear pores on the bottom surface. (E) Quantification of the nuclear pore segmentation. The average nuclear pore density is not significantly different between wild type and *Suv4-20h* DKO cells, or cells over-expressing *Suv4-20h2* (P values of Student's t-test). Regions with a low density of nuclear pores (sparse nuclear pore regions: less than 2 pores in a radius of 0.5μm) are less abundant in *Suv4-20h* DKO cells and are strongly increased in cells over-expressing *Suv4-20h2* (P values of Chi-square with Yates correction).

Figure S7. Large-scale chromatin compaction upon over-expression of Suv4-20h2.

Mouse embryonic fibroblast cells were transfected with constructs expressing EGFP or EGFP-tagged Suv4-20h2 truncations. 3D-SIM analysis of nuclear structure (DAPI) was then performed in EGFP-positive cells. Over-expression of *Suv4-20h2* full length and C-terminus (aa 280-468) lead to large-

scale chromatin compaction (increased chromatin density of peripheral heterochromatin and around nucleoli). Neither the N-Terminus (aa1-280) of Suv4-20h2 nor the clamp domain (M12) lead to obvious alterations in nuclear structure.

Figure S8. 3D image segmentation of major satellite FISH experiments.

Example results of 3D nuclei segmentation (green) and 3D foci segmentation (red) for nuclei of three different cell types: wild type cells (first row), *Suv4-20h* DKO cells (second row), and *Suv4-20h* DKO cells which re-express *Suv4-20h2* (third row). The first and second column show contours of the 3D segmentation results overlaid with the original images (maximum intensity projections, MIPs) of the FISH and DAPI channel, respectively. The third column shows 3D visualizations of the segmentation results.

Figure S9. Statistical tests for 3D image segmentation results.

Results of statistical relevance tests performed on the quantified number n of foci per nucleus: (A) Shapiro-Wilk test testing the null hypothesis that n is normally distributed for wild type cells, *Suv4-20h* DKO cells and rescue cells (DKO+FL). For DKO+M12 the null hypothesis is rejected. Therefore a two-sample Wilcoxon Rank Sum Test was performed showing no significant differences between DKO and DKO+M12. (B) F-test for homogeneity of variances of n (null hypothesis) between different cell types, (C) Welch-test for homogeneity of means of n (null hypothesis) between different cell types, indicating that the difference in FISH foci numbers is significantly different between wild type and *Suv4-20h* DKO cells.

Figure S10. The functional SET domain and the clamp domain of Suv4-20h2 are important to mediate chromocenter clustering.

Quantification of FISH analyses of major satellite repeats in G0 phase *Suv4-20h* DKO and *Suv4-20h2* rescue cells expressing *Suv4-20h2* with deletion of the clamp domain (DKO+ΔM12) or *Suv4-20h2* containing mutations that render the SET domain inactive (DKO+SET*). Chromocenter foci were counted and measured using an image segmentation analysis of confocal 3D stacks. Boxplots showing the numbers of chromocenters in *Suv4-20h* DKO (n=28), DKO+ΔM12 (n=25) and DKO+SET* (n=25) nuclei. The mean number of foci per nucleus is not significantly different between the three cell lines (statistical tests which correspond to the analysis in Figure S9 are shown in the right panel).

Figure S11. Mitotic stages in wild type and *Suv4-20h* DKO MEFs.

Progression through mitosis is normal in *Suv4-20h* DKO cells. Different mitotic stages were counted for wild type (n=285) and *Suv4-20h* DKO (n=335) MEFs (P-prophase, PM/M-prometaphase/metaphase, A-anaphase, T-telophase).

Figure S12. Suv4-20h2 GST pulldown and knock-in strategy.

(A) GST pulldown experiments were performed as described in materials and methods. Proteins which bound to the GST beads were eluted and loaded on a protein gel followed by silver staining. Recombinant GST, Suv4-20h2-M5 and Suv4-20h2-M7 proteins are marked with an arrow head, degradation products of the recombinant proteins are marked with asterisks. (B) PCR analysis for major satellite repeats with DNA isolated from sonicated extracts that were used for GST pulldown experiments and DNA isolated from benzonase-treated extracts. Undigested genomic DNA was used as control (gDNA). (C) Knock-in strategy for the *Suv4-20h2* locus. The region of the targeting construct which was used for homologous recombination in wild type ES cells is shown as thick line. The knock-

in allele contains the coding sequence for a HA-3xFLAG tag immediately after the last codon of *Suv4-20h2*. A FRT-flanked neomycin selection cassette was used for positive selection of the knock-in clones. (D) The clamp domain in Suv4-20h2 is important for cohesin interaction. Nuclear extract was prepared from wild type fibroblast cell lines expressing EGFP, Suv4-20h2-EGFP or Suv4-20h2-ΔM12-EGFP. Suv4-20h2 was precipitated from these extracts using EGFP affinity beads. Bound proteins were visualized by western blotting using Suv4-20h2 and Smc1 antibodies.

Figure S13. Cohesin ChIP in wild type, Suv4-20h2 KO and Suv4-20h DKO cells.

ChIP analysis for histone modifications (H3K9me3, H4K20me3) and cohesin subunits (Rad21, Smc3) in wild type (E19-8, W9), *Suv4-20h2* KO (E29-7, E27-5) and *Suv4-20h* DKO (E94-4, E35-3) cell lines. Major satellite repeats represent pericentric heterochromatin. Control regions where cohesin is enriched independently from H3K9me3-H4K20me3 (pos controls: Chr.6, Chr.7, Chr.10) and where cohesin is not present (neg. controls: Chr.5, Chr. 6-1, Chr.10-1) are shown. Merge of two experiments with three technical replicates, each. Error bars represent standard deviation.

Figure S14. Cohesin ChIP in wild type and Suv39h DKO cells.

ChIP analysis for histone modifications (H3K9me3, H4K20me3) and the cohesin subunit Smc3 in wild type (W9) and two independent *Suv39h* DKO cell lines. Major satellite repeats represent pericentric heterochromatin. Control regions where cohesin is enriched independently from H3K9me3-H4K20me3 (pos controls: Chr.6, Chr.7, Chr.10) and where cohesin is not present (neg. controls: Chr.5, Chr. 6-1, Chr.10-1) are shown. Merge of three technical replicates (two independent experiments for E124-1). Error bars represent standard deviation.

Figure S15. Cohesin ChIP in wild type and Suv4-20h rescue cells.

ChIP analysis for histone modifications (H3K9me3, H4K20me3) and cohesin (Smc3) were performed in wild type cells and *Suv4-20h* DKO cells which express full length Suv4-20h2-EGFP (DKO+FL) or Suv4-20h2-M12 (DKO+M12). The control region Chr.6 displays detectable levels of H4K20me3 upon re-expression of Suv4-20h2 in DKO cells, which is probably an over-expression effect. Merge of two experiments with three technical replicates, each. Error bars represent standard deviation.

Figure S16. FACS analyses of cell cycle synchronized fibroblasts.

FACS analysis of cells in G0, S and M phase. Cells were isolated as described and stained with propidium iodide prior to FACS analysis.

Figure S17. Cohesin ChIP in wild type and Suv4-20h rescue cells in different cell cycle stages.

ChIP analysis for histone modifications (H3K9me3, H4K20me3) and the cohesin subunit Smc3 were performed in wild type, *Suv4-20h* DKO and rescue cell lines expressing full length Suv4-20h2 (DKO+FL) or the Suv4-20h2 clamp domain (DKO+M12).

Figure S18. Suv4-20h1 does not interact with cohesin.

(A) Suv4-20h1 is a heterochromatin-associated protein. EGFP-tagged full length (C0) and different truncations of Suv4-20h1 were expressed in wild type fibroblast cells. Fragment C4 is the smallest truncation which is still able to localize to heterochromatin. This truncation contains one classical PxVxL HP1 interaction motif. (B) Knock-in strategy for the *Suv4-20h1* locus. The region of the targeting construct which was used for homologous recombination in wild type ES cells is shown as thick line. The knock-in allele contains the coding sequence for a HA-3xFLAG tag immediately after the last codon of *Suv4-20h1*. A FRT-flanked neomycin selection cassette was used for positive

selection of the knock-in clones. (C) Suv4-20h1 does not interact with cohesin. Nuclear extracts were prepared from wild type (wt) and *Suv4-20h1*$^{HA\text{-}FLAG}$ knock-in ES cells (KI). Suv4-20h1 was precipitated from these extracts using a FLAG antibody. Bound proteins were visualized by western blotting using FLAG and Smc1 antibodies.

Figure S19. Cohesin is not important to mediate chromocenter clustering.

(A) Inducible deletion of Scc1/Rad21. *Scc1*$^{f/+}$; Cre-ERT2 and *Scc1*$^{f/f}$; Cre-ERT2 (cko) cells (Seitan et al. 2011). Fibroblasts were arrested in G0 by serum deprivation. Addition of 4-OHT activates the Cre recombinase which leads to conversion of the *Scc1* flox to a *Scc1* mutant allele. Three weeks after addition of 4-OHT total cell extracts were prepared and analyzed for Scc1 protein levels compared to tubulin loading control. In 4-OHT-induced *Scc1* cko cells Scc1 protein is not detectable. The reduced signal intensity in lane 2 (induced *Scc1*$^{f/+}$ cells) is due to reduced loading. (B) Quantification of FISH analyses of major satellite repeats in G0 phase non-induced (control) vs. 4-OHT induced Scc1 cko cells. Chromocenter foci were counted and measured using an image segmentation analysis of confocal 3D stacks. Boxplots showing the numbers of chromocenters in Scc1 control (n=25) and Scc1 cko (n=28) nuclei. The mean number of foci per nucleus is not significantly different between the two cell lines (statistical tests which correspond to the analysis in Figure S9 are shown in the right panel).

SUPPLEMENTAL EXPERIMENTAL PROCEDURES

Cloning of Suv4-20h2-ΔM12:

Internal deletion mutants of the *Suv4-20h2* cDNA were created by inverse PCR on the *Suv4-20h2* wild type plasmid pDONR207-Suv4-20h2 using a reverse primer upstream and a forward primer downstream of the M12 region. Primer overhangs were designed to create 15 bp complementary ends on both sides of the PCR product to allow seamless recircularization using the Infusion HD cloning kit (Clontech).

Cell culture

MEF and ES cells were cultivated in High Glucose DMEM with L-Glutamine complemented with sodium pyruvate, fetal calf serum, beta-mercaptoethanol, non-essential amino acids (PAA) and penicillin/streptomycin (PAA) in a 37°C incubator at 5% CO_2. For ES cell culture medium was supplemented with leukemia inhibitory factor (LIF). Cells were transfected using Lipofectamine 2000 (Invitrogen) or TransIT-LT1 (Mirus). ES cells were seeded on matrigel (BD Biosciences) coated slides 24h before FRAP analysis.

FRAP

FRAP measurements were conducted in MEF and ES cell lines after transient expression of EGFP-tagged proteins using a Leica TCS SP5 confocal laser scanning microscope (CLSM) equipped with a HCX PL APO lambda blue 63x/1.4 NA oil immersion objective or an UltraVIEW VoX spinning disk microscope system (PerkinElmer). The region of interest (ROI) with an effective diameter of 1.9 μm was subjected to high intensity laser pulses to irreversibly bleach EGFP. Post-bleach images were collected at different time intervals with the laser intensity attenuated to the same level as in the pre-

bleach images. Analysis of the recovery curves of the intensity integrated over the ROI was done using FREDIS software (Muller et al. 2009). For Figure 1 the averaged recovery curves have been fitted to a diffusion model or a reaction-diffusion model that incorporates both diffusion and binding processes.

Fluorescence Correlation Spectroscopy

For FCS experiments a Zeiss LSM 710 ConfoCor3 was used. Before measurements, the system was calibrated with Alexa Fluor 488 C maleimide (Invitrogen) and from these measurements the effective focal volume was determined. Similar laser intensities were used for all experiments with an acquisition time of 60 s. For each FCS measurement a continuous photobleaching (CP) fit was applied to determine the immobile fraction as described previously (Wachsmuth et al. 2003; Muller et al. 2009). FCS data were analyzed as previously described (Erdel et al. 2010) with minor alterations. Since bleaching occurred during the measurements, especially in heterochromatin regions, only intensity fluctuations that were monitored 10 s after starting the acquisition were used for fittings. Then a moving average trend correction was applied and an autocorrelation function was fitted for anomalous diffusion. Over 15 individual cells per genotype were measured and averaged to derive the mobility data from the FCS based experiments. FCS data for HP1 were taken from (Muller et al. 2009).

HP1 interaction test

GST fusion proteins of Suv4-20h2, HP1α, HP1β and HP1γ were expressed in *E. coli* and purified using Glutathione-S-Sepharose beads (Amersham Biosciences). GST-tags of HP1α, HP1β and HP1γ were removed by PreScission (GE Healthcare) cleavage. Interaction tests were performed by incubating 5µg GST-Suv4-20h2 fusion protein with 5µg of either HP1α, HP1β and HP1γ in IP buffer [50 mM Tris pH 7.5, 150 mM NaCl, 1 mM EDTA, 0.1% NP40, 20% glycerol and proteinase inhibitor cocktail (Roche)] for 1h at room temperature on a rotating wheel. Then 60µl Glutathione-S- Sepharose beads were added

and incubated for 1h at 4°C on a rotating wheel. The beads were washed 3x with IP buffer containing 300 mM NaCl and eluted with 50 µl SDS sample buffer. Proteins were separated on SDS-polyacrylamidgels and detected by immunoblotting using isoform-specific HP1 antibodies (Euromedex).

Chromatin accessibility assay

Cytoplasm of wild type, Suv4-20h2 KO and Suv4-20h2 DKO ES cells and wild type, Suv4-20h DKO, DKO+FL and DKO+M12 fibroblast cell lines was removed by spinning through a Ficoll gradient. Isolated nuclei were resuspended in Ex100 buffer [10 mM HEPES pH 7.6, 100 mM KCl, 1.5 mM $MgCl_2$ 0.5 mM EGTA, 10% Glycerol, proteinase inhibitor cocktail (Roche)] and digested with different amounts of MNase (Sigma) in the presence of 3mM $CaCl_2$. Digest was stopped after 9 min by addition of 1/10 volume MNase stop buffer [0.5 M EDTA, 10% SDS]. Genomic DNA was purified and then separated on a 1% agarose gel, followed by blotting onto a Nylon membrane [Roti-Nylon plus, Roth] via capillary transfer. Hybridization with a ^{32}P-labeled major satellite probe was performed using standard conditions. MNase digestion patterns were further analyzed using the Agilent 2100 bioanalyzer (Agilent Technologies). 100ng of each sample were loaded onto a DNA LabChip using the Agilent DNA 12000 kit and analysis was performed using the 2100 expert software (Agilent Technologies). Southern blot quantification was performed using the line selection and plot profile function of ImageJ.

Lac-recruitment assay

EGFP-tagged proteins were recruited via a lac I repressor-GFP binding domain fusion protein to telomeres and promyelocytic leukemia nuclear bodies in a telomerase-negative U2OS cell carrying three integrations of lacO arrays as described (Jegou et al. 2009). 24 h after transfection, cells were

fixed and mounted with Prolong (Invitrogen). Images were taken with a Leica SP5 microscope and pictures were analyzed with ImageJ. Signal intensity of mCherry was measured at lacO arrays and regions adjacent to the lacO arrays. Positive recruitment was defined as the signal increase at the lacO array by >1.5 fold as compared to adjacent regions.

3D-structured illumination microscopy

Fibroblasts were seeded on No. 1.5H precision coverslips (thickness 0.170±0.005 mm; Marienfeld Superior), fixed with 4% formaldehyde, permeabilized with 0.5% Triton X-100, stained with 2 µg/ml 4',6-diamidino-2-phenylindole (DAPI) and embedded in Vectashield mounting medium (Vector Labs). Nuclear pore complexes (NPCs) were immunostained with monoclonal anti-Nup153 antibodies (QE5, Abcam) and Alexa Fluor 594 conjugated secondary antibodies (Invitrogen). Super-resolution 3D-structured illumination microscopy (3D-SIM) was performed as previously described (Schermelleh et al. 2008) on a Delta Vision OMX V3 system (Applied Precision) equipped with a 100x /1.40 NA PlanApo oil immersion objective (Olympus) and Cascade II:512 EMCCD cameras (Photometrics), using 405 nm and 592 nm diode lasers. In brief, a fine-striped interference pattern of illumination was generated by coherent laser light directed through a movable optical grating. Raw image stacks with 15 images per plane (5 phase shifts, 3 angles) and a z-distance of 125 nm were acquired and computationally reconstructed (SoftWoRX, Applied Precision) to obtain a super-resolution image dataset with a two-fold resolution improvement in x, y and z direction (eight-fold volumetric resolution improvement) compared to conventional diffraction-limited optical sectioning microscopy (Gustafsson et al. 2008). Images from the different color channels were registered with alignment parameter obtained from calibration measurements with 0.2 µm diameter TetraSpeck beads (Invitrogen).

Mitotic abnormalities

To quantify the number of abnormal mitotic figures in MEF cells, mitotic cells were collected by shake-off, spun onto glass-bottomed 96-black well plate (Greiner Bio-One) for 5min at 400g, fixed in 4% formaldehyde and stained with Vectashield containing DAPI.

To quantify mitotic stages MEF cells were grown for 48h cells on cover slips and fixed with 4% formaldehyde. After mounting with Vectashield containing DAPI cells were classified according to DAPI stain and mitotic spindle morphology into different stages: P-prophase; PM/M–prometaphase/metaphase; A-anaphase; T-telophase.

Immunofluorescence analysis

Immunofluorescence analyses were performed as described (Dambacher et al. 2012) using the following antibodies: CENP-A (C51A7, Cell Signaling Technology), AuroraB (Abcam ab2254), H4K20me3 (Schotta et al. 2008), Sgo1 (Whelan et al. 2012), Nup-153 (QE5, Abcam) and secondary antibodies conjugated to Cy5 (Dianova).

For chromosome spreads, untreated or nocodazole arrested (final concentration 200 nM, 4 h) mitotic cells were collected by shake-off, swollen for 10 min at room temperature in 75 mM KCl and spun onto microscope slides using a Cytospin centrifuge (Fischer). Cells were extracted for 5 min at room temperature with KCM-buffer [120 mM KCl, 20 mM MgCl2, 10 mM, Tris pH 8.0, 0.5 mM EDTA, 0.1% Triton X-100] and fixed in 2% formaldehyde. Slides were blocked for 30 min in KCM/0.1% Tween-20/2.5% BSA, and sequentially incubated with primary and secondary antibodies. After washing with KCM/0.1% Tween-20 chromosomes were mounted with Vectashield containing DAPI.

A Leica TCS SP5 confocal laser scanning microscope with a HCX PL APO CS 63x/1.3 NA glycerol immersion objective and a Zeiss LSM510 confocal microscope were used to obtain the images. Sequential excitation at 405 nm, 488 nm, 543 nm and 633 nm was provided by diode, argon and

helium-neon gas lasers, respectively. Emission detection ranges of the PMTs were adjusted to minimize crosstalk between the channels. Images were further analyzed using ImageJ software.

HP1 knock-out cell line

The W205C07 gene trap ESC line carrying a null mutation in the first intron of the HP1α gene was isolated from a large scale genetrap screen (Hansen et al. 2003) carried out in 129S2/SvPAS ES cells with the retroviral gene trap vector Rosabgeo. The W205C07 ESCs were converted into mice by standard procedures using C57BL6J host blastocysts. The 129/C57BL6J F1 offspring were back-crossed on C57BL6J for over 10 generations. The HP1α homozygous mutants are viable and show no obvious phenotype (PD and HvM, unpublished). Mouse Embryonic Fibroblasts (MEFs) were derived by standard procedures from E13.5 embryos and immortalized using the 3T3 protocol.

GST pull-down assays

GST fusions of Suv4-20h2 truncations were expressed from pGEX6P1 vector in *E. coli* and purified using Glutathione-S-Sepharose beads (Amersham Biosciences). Nuclei of wild type ES cells were isolated by spinning through a Ficoll gradient. For the Benzonase treatment cells were resuspended in low salt IP buffer [50 mM Tris pH 7.5, 150 mM KCl, 1 mM EDTA, 20% glycerol, 0.1% NP40] and digested with Benzonase (Merck Chemicals) for 15 min at 30°C, then adjusted to 500 mM KCl, incubated on ice for 30 min followed by 3x 10 sec sonication at an amplitude of 30 in a Branson sonifier. For the salt extract, proteins were extracted with high salt IP buffer [50 mM Tris pH 7.5, 500 mM KCl, 1 mM EDTA, 20% glycerol, 0.1% NP40, proteinase inhibitor cocktail (Roche)] incubated on ice for 30 min, followed by 3x 10 sec sonication at an amplitude of 30 in a Branson sonifier. Both nuclear extracts were diluted to a final concentration of 250 mM KCl with no salt IP buffer; precipitated or non-soluble proteins were then removed by centrifugation. 5µg of either GST or the

different GST-Suv4-20h2 fusion proteins were incubated with the Benzonase treated nuclear extract or salt extract supplemented with 50µg/ml EtBr over night at 4°C on a rotation wheel. Precipitates were again removed by centrifugation before 60µl Glutathione-S-Sepharose beads were added and incubated for another hour at 4°C. Beads were washed with IP buffer containing 300 mM KCl; subsequently, the bound proteins were eluted with 50µl SDS sample buffer. Proteins were separated on a SDS-polyacrylamid gel, visualized by silver staining and identified by mass-spectrometry analysis.

Co-immunoprecipitation

Nuclei of wild type and *Suv4-20h2*$^{HA\text{-}FLAG}$ ES cells were isolated by spinning through a Ficoll gradient. The nuclear pellet was resuspended in low salt IP Buffer [50mM Tris pH 7.5, 150mM KCl, 1mM EDTA, 20% glycerol, 0.1% NP40, proteinase inhibitor cocktail (Roche)]. Fraction I extract was isolated after digestion for 15 min at 37°C with Benzonase (Merck) in low salt IP buffer, followed by mild sonication 1x 10 sec at amplitude 20 in a Branson sonifier. Insoluble proteins were separated by spinning for 10 min at 13000 rpm at 4°C. The protein pellet was further extracted with high salt IP Buffer [50mM Tris pH 7.5, 500mM KCl, 1mM EDTA, 20% glycerol, 0.1% NP40, proteinase inhibitor cocktail (Roche)] on ice for 30 min followed by 3x 10 sec sonication at an amplitude of 30 in a Branson sonifier. Fraction II extract was then diluted to a final concentration of 250mM NaCl with no salt IP Buffer and precipitated or insoluble proteins were removed by centrifugation (30min, 13000rpm, 4°C). The different extracts were incubated with either 5µg Flag M2 antibody (Sigma) or Smc1 antibody (Bethyl Labs) coupled to ProteinA/G magnetic beads (Dynabeads Invitrogen) o/n at 4°C on a rotating wheel. The beads were washed 5x in IP buffer containing 300mM KCl and eluted with SDS sample buffer. Proteins were separated on SDS-polyacrylamidgels and analyzed by western blotting using antibodies for Flag M2 (Sigma), Smc1 (Bethyl labs), Smc3 (Abcam), Suz12 (Cell Signalling) and Suv4-20h2 (Dambacher et al. 2012). Immunoprecipitation experiments of EGFP-

tagged proteins were performed using GFP-Trap A beads (ChromoTek).

Chromatin immunoprecipitation (ChIP)

ChIP experiments were performed according to standard methods. Chromatin was sonicated to an average size of 300-600 bp. 50 µl Dynabeads Protein A/G beads (Dynabeads, Invitrogen) were pre-bound with 3-5 µg antibody (anti-H3K9me3 Abcam #ab8898, anti-H4K20me3 Active Motif #39180.3918 or Millipore #07-463, anti-Rad21 Abcam #ab992, anti-Smc3 Abcam #ab9263) and added to the chromatin. After 16 h incubation at 4°C on a rotating wheel beads were collected by DynaMag magnet (or Dynal MPC) for 1 min. Beads were washed with Sonication buffer [50 mM Hepes pH 7.9, 140 mM NaCl, 1 mM EDTA, 1% Triton X-100, 0.1% Na-deoxycholate, 0.1% SDS, 0.5 mM PMSF, Protease inhibitor cocktail (Roche)], wash buffer A [Sonication buffer supplemented with 500mM NaCl], wash buffer B [20 mM Tris, pH 8.0, 1 mM EDTA, 250 mM LiCl, 0.5% NP-40, 0.5% Na-deoxycholate, 0.5 mM PMSF, Roche protease inhibitor cocktail] and TE buffer pH 8.0 [10 mM Tris-Cl pH 8.0, 1 mM EDTA pH 8.0 (supplemented with 50 mM NaCl)]. 200 µl of elution buffer [50 mM Tris pH 8.0, 1 mM EDTA, 1% SDS, 50mM $NaHCO_3$] was added to the beads for 20 min at 65°C in two rounds. Eluates were purified after crosslink reversal using the GenElute PCR Clean-Up Kit (Sigma).

Cell cycle arrest

MEF cells were plated onto 150 mm plates at 40-50% confluency and treated with 2 mM thymidine. After 18 h cells were washed 3x with medium, and after 8 h the second thymidine block was applied. Cells were released after 17 h by 3 washes with medium and harvested 3 h after the release. For mitotic arrest MEF cells were first treated with thymidine (2 mM) for 20h. Then cells were washed 3x with medium, and after 3 h nocodazole was added to 100 ng/ml. Cells were harvested 11 h after the

thymidine release by mitotic shake-off. Cells were arrested in G0 by 48 h serum starvation. The *Scc1*/*Rad21* conditional knock-out cell line (*Scc1*$^{lox/lox}$; Cre-ERT2) was arrested in G0 by serum starvation and after 72 h treated with ethanol (Scc1 control) or induced with 250 nM final concentration of 4-OHT (solubilized in ethanol) for 21 days (Scc1 cko). The medium was exchanged every 3 days.

FACS

Cells were stained with propidium iodide (PI) to analyze the cell cycle phase by DNA amount. Trypsinized MEF cells were fixed with 70% methanol for 30 min on ice and PBS washed. PI staining was performed at 37°C for 30 min in a buffer containing 10 mM Tris pH 7.5, 5 mM $MgCl_2$ and 200 µg RNAse A.

Suv4-20h1 and Suv4-20h2 knock-in cell lines

The *Suv4-20h1*$^{HA\text{-}FLAG}$ and *Suv4-20h2*$^{HA\text{-}FLAG}$ targeting constructs were obtained using the recombineering cloning technique described previously. The NotI-linearized targeting vector was electroporated into feeder-independent wild type ES cells. Cells were selected in 180 µg/ml G418 (PAA) and 2 µM Ganciclovir (Invivogen). Single colonies were picked and screened by nested PCR to obtain the final ES cell clones. The same strategy was used for generating *Suv4-20h2*^{EGFP} knock-in ES cells, except that the targeting construct contained the EGFP open reading frame fused to the last codon of Suv4-20h2. Primers used for cloning and PCR screening are listed in Table S1.

Automatic 3D Quantification of FISH Foci

To determine quantitative information of FISH major satellite repeats from the acquired two-channel 3D confocal microscopy images, we developed a fully automatic 3D image analysis approach consisting of 3D cell nuclei segmentation and 3D foci segmentation. First, 3D cell nuclei segmentation

is performed by Otsu thresholding based on the information in the DAPI channel. This enables to determine relevant parameters (e.g., number and mean volume of FISH foci) for each nucleus individually. To ensure a valid statistical analysis, cell nuclei at the image border which are only partially visible are automatically excluded using a threshold on the number of border voxels of the segmented nucleus volume. Second, after cell nuclei segmentation, 3D foci segmentation is performed in the FISH channel using global thresholding and morphological opening. As a result, quantitative information of FISH foci (e.g., volume, 3D position, and 3D shape) is obtained. In addition, the 3D regions of segmented FISH foci are used to quantify heterochromatin concentrations in the DAPI channel.

In a subsequent statistical analysis, we further investigated the mean number of foci per nucleus denoted by n and the quantified foci volumes denoted by v. We subdivided the results into 3 groups w.r.t. the experimental setup: (1) wild type cells, (2) *Suv4-20h* DKO cells, (3) re-express *Suv4-20h2* cells. To ensure that our findings (Fig. 5c) are statistically relevant, we first performed a Shapiro-Wilk test, which indicated that in all groups n is normally distributed, and an F-Test which revealed that the variance of n differs significantly for groups (1) vs. (3). Therefore, we used a Welch-test which showed that the mean values of n for groups (1) vs. (2) and (3) vs. (2) differ significantly, while the mean values of n of groups (1) vs. (3) do not differ significantly. To investigate the foci volumes, we computed histograms of v for each group. It can be seen, that group (2) contains significantly more small foci with a volume < 2500 voxels, while groups (1) and (3) contain more foci with a larger volume.

Quantification of peripheral heterochromatin and nuclear pores

To determine quantitative information about the nuclear pores from the two-channel 3D SIM images, we developed an automatic 3D image analysis approach consisting of 3D cell nuclei segmentation and

3D model-based segmentation of the pores. First, the 3D cell nuclei are segmented in the DAPI channel by multi-level 3D Otsu thresholding and by using 3D grayscale morphological filters. Second, the 3D nuclear pores are localized and segmented in the NPC channel using an automatic 3D approach based on a 3D anisotropic Gaussian parametric intensity model (Worz et al. 2010), which is accurate for small subcellular structures. As a result, quantitative information about each of the segmented nuclear pores (e.g., volume, 3D position, and distance to neighboring pores) is obtained with subvoxel accuracy. By using the results of 3D cell nuclei segmentation, relevant parameters like, e.g., the mean volume or mean distance to neighboring pores, are determined individually for each cell nucleus.

To quantify the amount of heterochromatin near the nuclear lamina, 2D slices along the z-axis from the segmented 3D cell nuclei volumes are extracted. For each extracted slice, a region-of-interest is defined near the nuclear lamina within a 150 nm radius from the contour of the segmented nucleus. Then, within the region-of-interest the total amount of signal intensity in the DAPI channel is determined.

SUPPLEMENTAL REFERENCES

Dambacher S, Deng W, Hahn M, Sadic D, Frohlich J, Nuber A, Hoischen C, Diekmann S, Leonhardt H, Schotta G. 2012. CENP-C facilitates the recruitment of M18BP1 to centromeric chromatin. *Nucleus* **3**.

Erdel F, Schubert T, Marth C, Langst G, Rippe K. 2010. Human ISWI chromatin-remodeling complexes sample nucleosomes via transient binding reactions and become immobilized at active sites. *Proc Natl Acad Sci U S A* **107**: 19873-19878.

Gustafsson MG, Shao L, Carlton PM, Wang CJ, Golubovskaya IN, Cande WZ, Agard DA, Sedat JW. 2008. Three-dimensional resolution doubling in wide-field fluorescence microscopy by structured illumination. *Biophysical journal* **94**: 4957-4970.

Hansen J, Floss T, Van Sloun P, Fuchtbauer EM, Vauti F, Arnold HH, Schnutgen F, Wurst W, von Melchner H, Ruiz P. 2003. A large-scale, gene-driven mutagenesis approach for the functional analysis of the mouse genome. *Proc Natl Acad Sci U S A* **100**: 9918-9922.

Jegou T, Chung I, Heuvelman G, Wachsmuth M, Gorisch SM, Greulich-Bode KM, Boukamp P, Lichter P, Rippe K. 2009. Dynamics of telomeres and promyelocytic leukemia nuclear bodies in a telomerase-negative human cell line. *Mol Biol Cell* **20**: 2070-2082.

Muller KP, Erdel F, Caudron-Herger M, Marth C, Fodor BD, Richter M, Scaranaro M, Beaudouin J, Wachsmuth M, Rippe K. 2009. Multiscale analysis of dynamics and interactions of heterochromatin protein 1 by fluorescence fluctuation microscopy. *Biophysical journal* **97**: 2876-2885.

Schermelleh L, Carlton PM, Haase S, Shao L, Winoto L, Kner P, Burke B, Cardoso MC, Agard DA,

Gustafsson MG et al. 2008. Subdiffraction multicolor imaging of the nuclear periphery with 3D structured illumination microscopy. *Science* **320**: 1332-1336.

Schotta G, Sengupta R, Kubicek S, Malin S, Kauer M, Callen E, Celeste A, Pagani M, Opravil S, De La Rosa-Velazquez IA et al. 2008. A chromatin-wide transition to H4K20 monomethylation impairs genome integrity and programmed DNA rearrangements in the mouse. *Genes Dev* **22**: 2048-2061.

Seitan VC, Hao B, Tachibana-Konwalski K, Lavagnolli T, Mira-Bontenbal H, Brown KE, Teng G, Carroll T, Terry A, Horan K et al. 2011. A role for cohesin in T-cell-receptor rearrangement and thymocyte differentiation. *Nature* **476**: 467-471.

Wachsmuth M, Weidemann T, Muller G, Hoffmann-Rohrer UW, Knoch TA, Waldeck W, Langowski J. 2003. Analyzing intracellular binding and diffusion with continuous fluorescence photobleaching. *Biophysical journal* **84**: 3353-3363.

Whelan G, Kreidl E, Wutz G, Egner A, Peters JM, Eichele G. 2012. Cohesin acetyltransferase Esco2 is a cell viability factor and is required for cohesion in pericentric heterochromatin. *EMBO J* **31**: 71-82.

Worz S, Sander P, Pfannmoller M, Rieker RJ, Joos S, Mechtersheimer G, Boukamp P, Lichter P, Rohr K. 2010. 3D geometry-based quantification of colocalizations in multichannel 3D microscopy images of human soft tissue tumors. *IEEE transactions on medical imaging* **29**: 1474-1484.

Table S1. Mass-spec list of the Suv4-20h2 GST pulldown assays. The number of unique spectra that were identified for each protein in the mass-spec analysis is indicated (Scaffold analysis).

gene	name	GST	M5	M7	delta
Suv420h2	histone-lysine N-methyltransferase SUV420H2	4	112	62	108
Lmnb1	lamin-B1	1	82	75	81
Top2a	DNA topoisomerase 2-alpha	0	49	0	49
Cbx5	chromobox protein homolog 5	0	41	0	41
Hnrnpu	heterogeneous nuclear ribonucleoprotein U	2	43	4	41
CBX1	chromobox protein homolog 1	0	40	0	40
Plec	plectin	0	40	8	40
CBX3	chromobox protein homolog 3	1	40	0	39
Jup	junction plakoglobin	4	37	13	33
Mybbp1a	myb-binding protein 1A	0	30	0	30
Ahnak	AHNAK nucleoprotein	4	34	13	30
Krt31	keratin, type I cuticular Ha1	0	29	0	29
Ddx21	nucleolar RNA helicase 2	0	28	0	28
Nop58	nucleolar protein 58	0	23	0	23
Ncl	nucleolin	1	24	1	23
Nop56	nucleolar protein 56	0	23	12	23
5430421N21	type II hair keratin	1	20	2	19
Eef2	elongation factor 2	0	19	8	19
Hnrnpa3	heterogeneous nuclear ribonucleoprotein A3	4	23	12	19
Ddx5	probable ATP-dependent RNA helicase DDX5	4	22	1	18
Cltc	clathrin heavy chain 1	0	18	3	18
Vcl	vinculin	0	18	4	18
Acly	ATP-citrate synthase	0	18	5	18
Nup93	nuclear pore complex protein Nup93	0	16	0	16
Fasn	fatty acid synthase	0	16	3	16
Nolc1	nucleolar and coiled-body phosphoprotein 1	0	15	0	15
Hsp90b1	endoplasmin	2	17	8	15
Nup107	nuclear pore complex protein Nup107	0	14	0	14
Tpr	nuclear pore complex-associated protein Tpr	0	14	0	14
Nedd4	E3 ubiquitin-protein ligase NEDD4	0	14	3	14
Ddx3x	ATP-dependent RNA helicase DDX3X	2	15	0	13
Smarca5	SWI/SNF-related matrix-associated actin-dependent regulator of chromatin subfamily A	0	12	0	12
Ranbp2	E3 SUMO-protein ligase RanBP2	0	12	3	12
Vcp	transitional endoplasmic reticulum ATPase	2	14	6	12
Spna2	spectrin alpha chain, brain	0	12	6	12
Vdac2	voltage-dependent anion-selective channel protein 2	3	14	1	11
Myh9	myosin-9	0	11	3	11
Atrx	transcriptional regulator ATRX	0	10	0	10
Ddost	dolichyl-diphosphooligosaccharide--protein glycosyltransferase 48 kDa subunit	0	10	0	10
Las1l	protein LAS1 homolog	0	10	0	10
Nup85	nuclear pore complex protein Nup85	0	10	0	10
Nup98	nucleoporin 98	0	10	0	10
Snrnp200	U5 small nuclear ribonucleoprotein 200 kDa helicase	0	10	0	10
Ephx1	epoxide hydrolase 1	4	14	1	10
Vars	valyl-tRNA synthetase	0	10	2	10
Col1a1	collagen alpha-1(I) chain	2	12	4	10
Actn1	alpha-actinin-1	2	12	6	10
Hnrnpul2	heterogeneous nuclear ribonucleoprotein U-like protein 2	0	9	1	9
Trim28	transcription intermediary factor 1-beta	0	9	1	9
Eef1b2	elongation factor 1-beta	3	12	3	9
Spnb2	spectrin beta chain, brain 1	0	9	4	9
Krt77	keratin, type II cytoskeletal 1b	4	13	6	9
Nat10	N-acetyltransferase 10	0	8	0	8

Orc1	origin recognition complex subunit 1	0	8	0	8
Pwp2	periodic tryptophan protein 2 homolog	0	8	0	8
Eprs	bifunctional aminoacyl-tRNA synthetase	0	8	1	8
Nup205	nucleoporin 205	0	8	1	8
Canx	calnexin	2	10	5	8
Krt78	keratin Kb40	4	12	6	8
Hist1h3e	histone H3.2	1	9	9	8
Rif1	telomere-associated protein RIF1	1	8	0	7
Mcm3	DNA replication licensing factor MCM3	0	7	0	7
Tcof1	treacle protein	0	7	0	7
Vdac1	voltage-dependent anion-selective channel protein 1	3	10	1	7
Eif3c	eukaryotic translation initiation factor 3 subunit C	0	7	1	7
Smc1a	structural maintenance of chromosomes protein 1A	0	7	1	7
Rpl5	60S ribosomal protein L5	2	8	0	6
Mki67	antigen KI-67	0	6	0	6
Ptbp1	polypyrimidine tract-binding protein 1	0	6	0	6
Ruvbl1	ruvB-like 1	0	6	0	6
Sf3b1	splicing factor 3B subunit 1	0	6	0	6
Tmpo	lamina-associated polypeptide 2	0	6	0	6
Uqcrc1	cytochrome b-c1 complex subunit 1, mitochondrial	0	6	0	6
Alb	serum albumin	2	8	2	6
Ndufs1	NADH-ubiquinone oxidoreductase 75 kDa subunit, mitochondrial	0	6	2	6
Top2b	DNA topoisomerase 2-beta	2	8	3	6
Rrbp1	ribosome-binding protein 1	0	6	3	6
Snd1	staphylococcal nuclease domain-containing protein 1	0	6	3	6
Stt3a	dolichyl-diphosphooligosaccharide--protein glycosyltransferase subunit STT3A	0	6	3	6
Aldh18a1	delta-1-pyrroline-5-carboxylate synthase	0	6	4	6
LOC100047		0	6	4	6
Krt75	keratin, type II cytoskeletal 75	1	7	5	6
Insrr	insulin receptor-related protein	2	8	7	6
Krt13	keratin, type I cytoskeletal 13	0	6	7	6
Hnrnpl	heterogeneous nuclear ribonucleoprotein L	2	7	0	5
Ddx17	probable ATP-dependent RNA helicase DDX17	0	5	0	5
Mcm5	DNA replication licensing factor MCM5	0	5	0	5
Numa1	nuclear mitotic apparatus protein 1	0	5	0	5
Otc	ornithine carbamoyltransferase, mitochondrial	0	5	0	5
Pdcd11	protein RRP5 homolog	0	5	0	5
Sf3a1	splicing factor 3A subunit 1	0	5	0	5
Sf3b2	splicing factor 3b, subunit 2	0	5	0	5
Wdr3	WD repeat-containing protein 3	0	5	0	5
Ddx3y	ATP-dependent RNA helicase DDX3Y	2	7	1	5
Lyz1	lysozyme C-1	3	8	2	5
Sfn	14-3-3 protein sigma	0	5	2	5
Dnmt3b	DNA (cytosine-5)-methyltransferase 3B	0	5	3	5
Hnrnpa2b1	heterogeneous nuclear ribonucleoproteins A2/B1	4	9	6	5
Fam161b	protein FAM161B	1	5	0	4
2610101N10	U2 snRNP-associated SURP motif-containing protein	0	4	0	4
Acin1	apoptotic chromatin condensation inducer in the nucleus	0	4	0	4
Ddx18	ATP-dependent RNA helicase DDX18	0	4	0	4
Fads2	fatty acid desaturase 2	0	4	0	4
Flnc	filamin-C	0	4	0	4
Krt33a	keratin, type I cuticular Ha3-I	0	4	0	4
Lama3	laminin subunit alpha-3	0	4	0	4
LOC100046		0	4	0	4
Nnt	NAD(P) transhydrogenase, mitochondrial	0	4	0	4
Nvl	nuclear valosin-containing protein-like	0	4	0	4
Prpf6	pre-mRNA-processing factor 6	0	4	0	4
Rpl22	60S ribosomal protein L22	0	4	0	4
Rpl23	60S ribosomal protein L23	0	4	0	4

Tln1	talin-1	0	4	0	4
Wdr36	WD repeat domain 36	0	4	0	4
D1Pas1	putative ATP-dependent RNA helicase Pl10		4	0	4
Fscn1	fascin	2	6	1	4
Hnrnph1	heterogeneous nuclear ribonucleoprotein H	2	6	1	4
Hspb1	heat shock protein beta-1	0	4	1	4
Actn4	alpha-actinin-4	0	4	2	4
Dst	dystonin	0	4	2	4
Gemin5	gem-associated protein 5	0	4	2	4
Hspa4	heat shock 70 kDa protein 4	0	4	2	4
Odf2l	outer dense fiber protein 2-like	0	4	2	4
Bicd1	protein bicaudal D homolog 1	0	4	3	4
Sarnp	SAP domain-containing ribonucleoprotein	0	4	3	4
Vps35	vacuolar protein sorting-associated protein 35	4	8	4	4
Gucy2c	heat-stable enterotoxin receptor	2	6	4	4
Krt35	keratin, type I cuticular Ha5	2	6	4	4
Plk2	serine/threonine-protein kinase PLK2	2	6	6	4
2410002O22	UPF0533 protein C5orf44 homolog	1	4	0	3
Fam98c	uncharacterized protein LOC73833	1	4	0	3
Rpl28-ps3		1	4	0	3
Shisa9	protein shisa-9	1	4	0	3
Abcc2	canalicular multispecific organic anion transporter 1	0	3	0	3
Alyref	THO complex subunit 4	0	3	0	3
Cacna2d4	voltage-dependent calcium channel subunit alpha-2/delta-4	0	3	0	3
Dsg1a	desmoglein-1-alpha	0	3	0	3
E2f2	transcription factor E2F2	0	3	0	3
Eed	polycomb protein EED	0	3	0	3
Eftud2	116 kDa U5 small nuclear ribonucleoprotein component	0	3	0	3
Fam65b	protein FAM65B	0	3	0	3
Grpel1	grpE protein homolog 1, mitochondrial	0	3	0	3
Hdac2	histone deacetylase 2	0	3	0	3
Kif1b	kinesin-like protein KIF1B	0	3	0	3
Lgals3bp	galectin-3-binding protein	0	3	0	3
Nup160	nuclear pore complex protein Nup160	0	3	0	3
P2rx3	P2X purinoceptor 3	0	3	0	3
Pcnxl3	pecanex-like protein 3	0	3	0	3
Pml	protein PML	0	3	0	3
Smc3	structural maintenance of chromosomes protein 3	0	3	0	3
Smg6	telomerase-binding protein EST1A	0	3	0	3
Tnr	tenascin-R	0	3	0	3
Vezt	vezatin	0	3	0	3
Vps16	vacuolar protein sorting-associated protein 16 homolog	0	3	0	3
Wdr46	WD repeat-containing protein 46	0	3	0	3
Yes1	tyrosine-protein kinase Yes	0	3	0	3
Arid5a	AT-rich interactive domain-containing protein 5A	0	3	1	3
Ddx58	probable ATP-dependent RNA helicase DDX58	0	3	1	3
Gdf15	growth/differentiation factor 15	0	3	1	3
Hinfp	histone H4 transcription factor	0	3	1	3
Sf3b3	splicing factor 3B subunit 3	0	3	1	3
Slc25a13	calcium-binding mitochondrial carrier protein Aralar2	0	3	1	3
Stag2	cohesin subunit SA-2	0	3	1	3
Taf1	transcription initiation factor TFIID subunit 1	0	3	1	3
Lrpprc	leucine-rich PPR motif-containing protein, mitochondrial	1	4	2	3
Herc2	E3 ubiquitin-protein ligase HERC2	0	3	2	3
Rere	arginine-glutamic acid dipeptide repeats protein	0	3	2	3
Hnrnpab	heterogeneous nuclear ribonucleoprotein A/B	4	7	3	3
Fras1	extracellular matrix protein FRAS1	2	5	3	3
Hnrnpd	heterogeneous nuclear ribonucleoprotein D0	2	5	3	3
Chrna10	neuronal acetylcholine receptor subunit alpha-10	0	3	3	3

Dock9	dedicator of cytokinesis protein 9	0	3	3	3
Erc1	ELKS/Rab6-interacting/CAST family member 1	0	3	3	3
Hnrnpa0	heterogeneous nuclear ribonucleoprotein A0	0	3	3	3
Pard6g	partitioning defective 6 homolog gamma	0	3	3	3
Prpf8	pre-mRNA-processing-splicing factor 8	0	3	3	3
Ube2t	ubiquitin-conjugating enzyme E2 T	0	3	3	3
Vash1	vasohibin-1	1	4	4	3
Mei4	UPF0623 protein	0	3	4	3

Table S2. Primer sequences.

cloning primer		
Suv39h2	f	ggggacaagtttgtacaaaaaagcaggcttaactatggcggcggccagggcc
	r	ggggaccactttgtacaagaaagctgggtcgttgaggtaacctctgcaa
M12,M13+M14 pGex6P1 direct cloning		
Suv4-20h2 pGex6P1: 350f BamHI	f	GGGATCCgtcctccgcactgcctgtgt
Suv4-20h2 pGex6P1: 385f BamHI	f	GGGATCCcgctggaccccacaacag
Suv4-20h2 pGex6P1: 412r EcoRI	r	GGAATTCctaggctaggcgggtaagttc
Suv4-20h2 pGex6P1: 385r EcoRI	r	GGAATTCctagcgagtctgggggcgcag
M7	f	ggggacaagtttgtacaaaaaagcaggcttaaccatgacccgcctagccccagcc
	r	ggggaccactttgtacaagaaagctgggtctggctcaccactattgat
M12	f	ggggacaagtttgtacaaaaaagcaggcttaaccatggtcctccgcactgcctgt
	r	ggggaccactttgtacaagaaagctgggtcggctaggcgggtaagttc
M13	f	ggggacaagtttgtacaaaaaagcaggcttaaccatggtcctccgcactgcctgt
	r	ggggaccactttgtacaagaaagctgggtcgcgagtctgggggcgcag
M14	f	ggggacaagtttgtacaaaaaagcaggcttaaccatgcgctggaccccacaacag
	r	ggggaccactttgtacaagaaagctgggtcggctaggcgggtaagttc
ΔM12	f	attgcctcctccagccctgccagctgct
	r	gctggaggaggcaatgaagcctggc
HP1β	f	ggggacaagtttgtacaaaaaagcaggcttaactatggggaaaaagcaaaac
	r	ggggaccactttgtacaagaaagctgggtcattcttgtcgtcttttttgtc
HP1γ	f	ggggacaagtttgtacaaaaaagcaggcttaaaaatggcctccaataaaactac
	r	ggggaccactttgtacaagaaagctgggtcttgtgcttcatcttcaggac
HP1α	f	ggggacaagtttgtacaaaaaagcaggcttaagacatgggaaagaagacc
	r	ggggaccactttgtacaagaaagctgggtcgctcttcgcgctttcttttttc
Suv4-20h1_10	f	GGGGACAAGTTTGTACAAAAAAGCAGGCTACaacatggtggtgaatggcaggag
Suv4-20h1_883	r	GGGGACCACTTTGTACAAGAAAGCTGGGTCtgcgttcagtcttagagactgatc
Suv4-20h1_392	r	GGGGACCACTTTGTACAAGAAAGCTGGGTCcttacttgcattgtctttttcctg
Suv4-20h1_392	f	GGGGACAAGTTTGTACAAAAAAGCAGGCTTAaccatgtctaatcgaaaatcttcagttggtgtg
Suv4-20h1_847	r	GGGGACCACTTTGTACAAGAAAGCTGGGTCgtcatcatcgaagtcatcctcgc
Suv4-20h1_496	r	GGGGACCACTTTGTACAAGAAAGCTGGGTCctccctttctttcttaattggc
ChIP primer		
Major satellites	f	GACGACTTGAAAAATGACGAAATC
	r	CATATTCCAGGTCCTTCAGTGTGC
Chr. 6	f	GATGGGAAAGCGTTGTTAGC
chr6:90702961+90703046	r	AAGGACAGCTCCTTTTTCAGG
Chr. 7	f	AATTTCACTGCGATCCTTGC
chr7:45669448+45669542	r	GCCGGAATTATGGCTCTATG
Chr. 10	f	TTCTGCTAAAGCCTGGACTTG
chr10:76574384+76574531	r	TGCTTGCAAGTGGCTAAGG
Chr. 5	f	ATGCTCACGTCCTTGTCCAGAA
chr5:147617294+147617396	r	TCTGGCAGCCTTCAACGTTTGT
Chr. 6-1	f	TGCAGGTGGGATTAACTGTG
chr6:122673061+122673143	r	CTACCCACCCCCTATTCTCC
Chr10-1	f	TGGGTGCCGTATGCCACATTAT
chr10:79154346+79154481	r	TTTCTGGCCATCCGCACCTTAT
genotyping primer for Suv4-20h2 knock-in		
MGC_tag_1f	f	CACTCCCACTGTCCTTTCCTAA
MGC_tag_1r	r	CAAACTCACAGAGAGCCACCTA
MGC_tag_2f	f	TCGCATTGTCTGAGTAGGTGTC

A

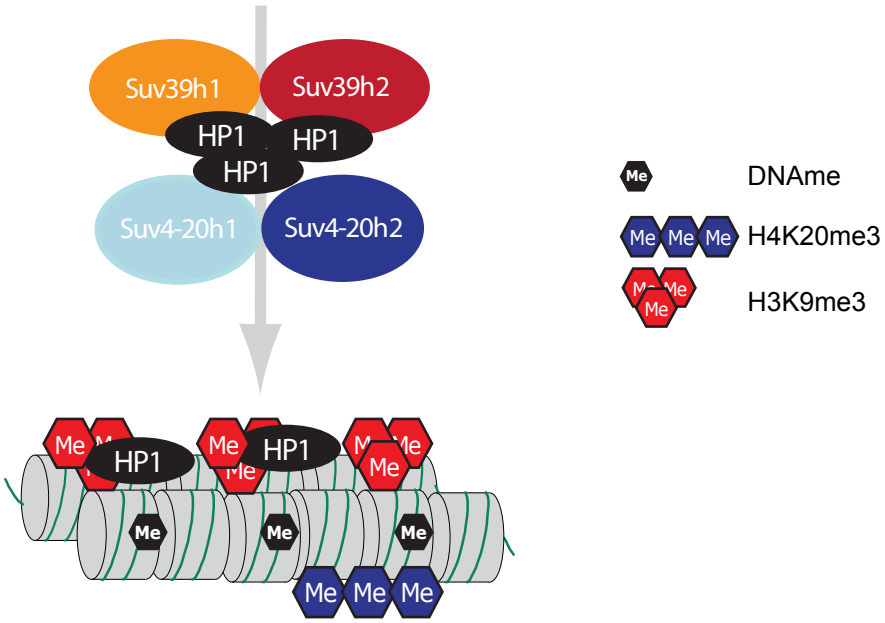
Suv39h1
Suv39h2
HP1
HP1
HP1
Suv4-20h1
Suv4-20h2
Me
DNAme
Me Me Me
H4K20me3
H3K9me3
HP1
HP1

B

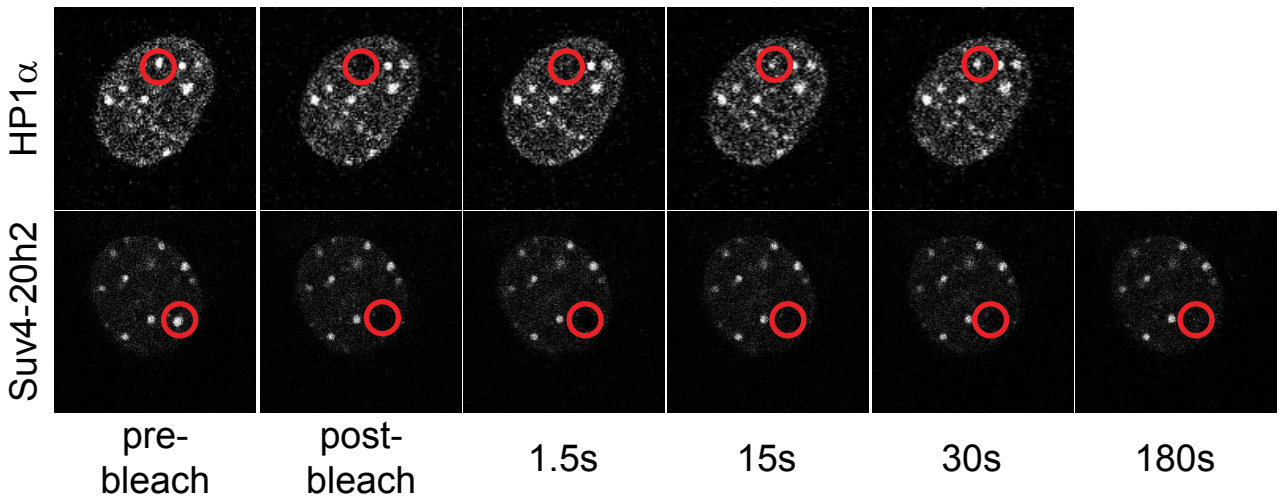
FRAP analysis at heterochromatin
HP1α
Suv4-20h2
pre-bleach
post-bleach
1.5s
15s
30s
180s

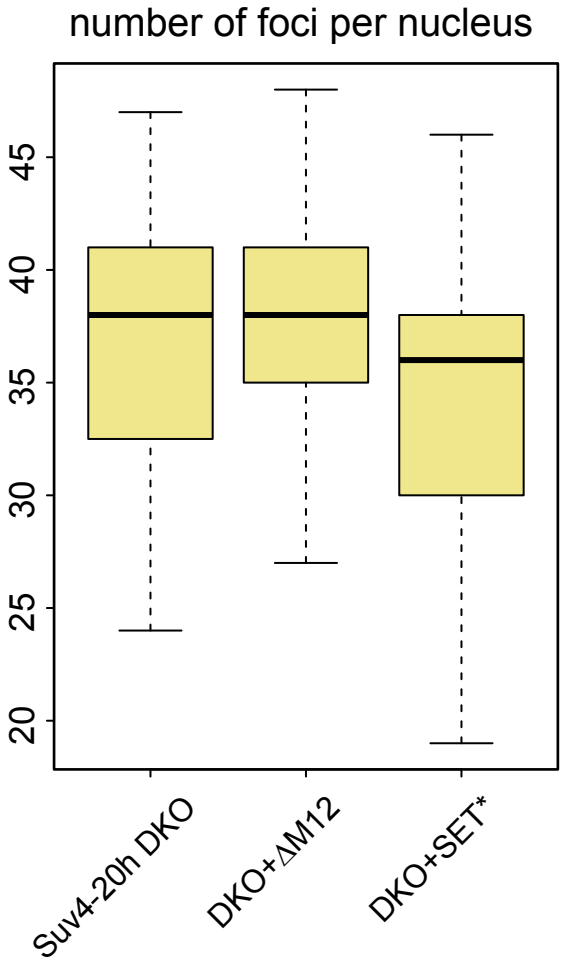

Shapiro-Wilk test

DKO:	W=0,9519
	p-value=0,2205
DKO+ΔM12:	W=0,9705
	p-value=0,6575
DKO+SET*:	W=0,9591
	p-value=0,3963

F-test

DKO	
vs. DKO+ΔM12:	p-value=0,6402
DKO	
vs. DKO+SET*:	p-value=0,8246

Welch-test

DKO	
vs. DKO+ΔM12:	p-value=0,4517
DKO	
vs. DKO+SET*:	p-value=0,1573

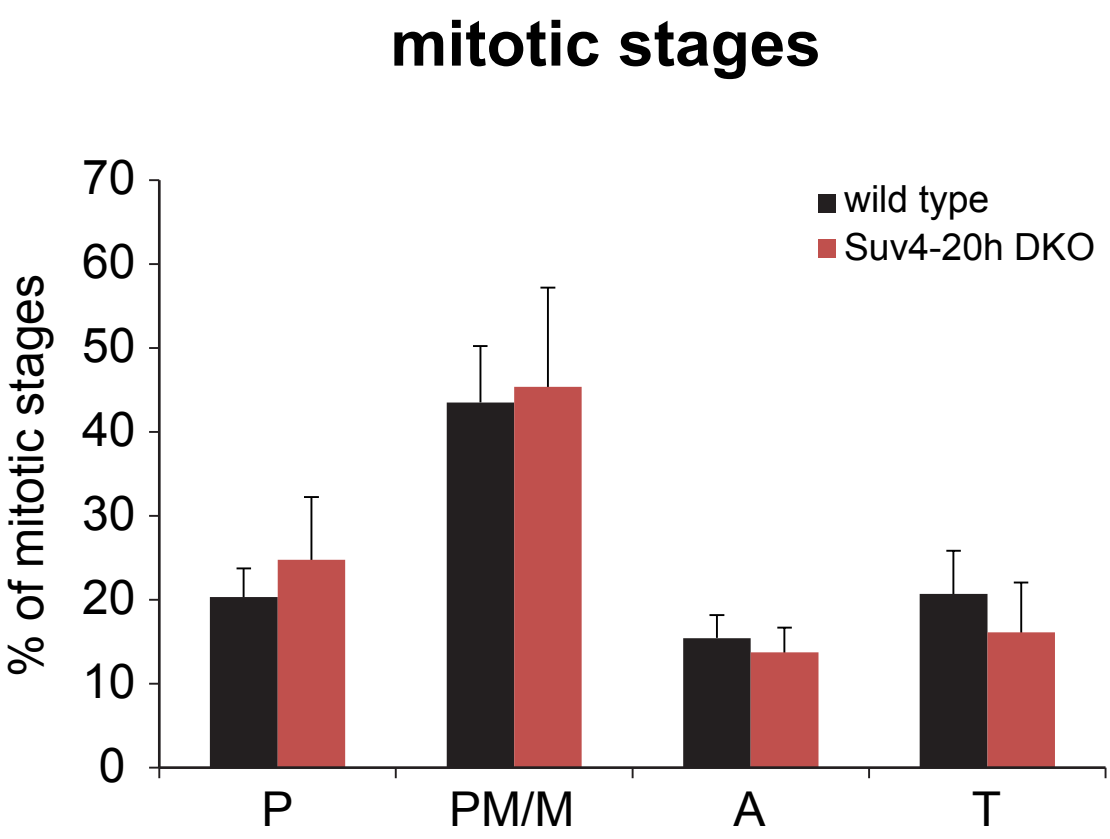
mitotic stages
% of mitotic stages
70
60
50
40
30
20
10
0
P
PM/M
A
T
wild type
Suv4-20h DKO

A

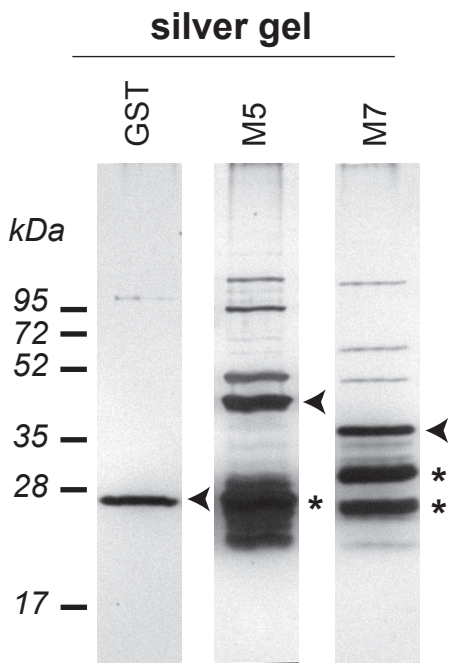
silver gel
GST
M5
M7
kDa
95
72
52
35
28
17
*
*
*

B

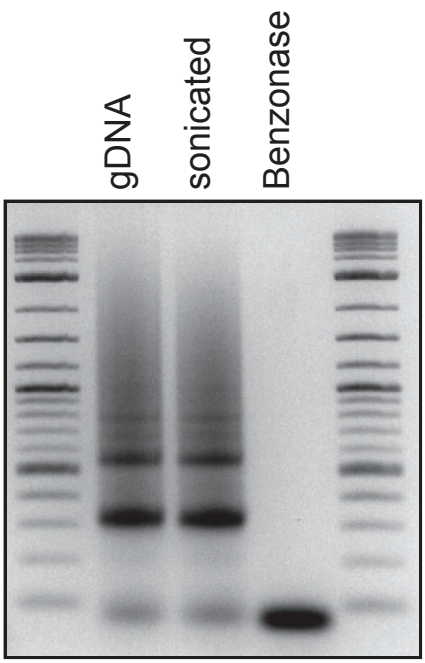
PCR major satellites
gDNA
sonicated
Benzonase

C

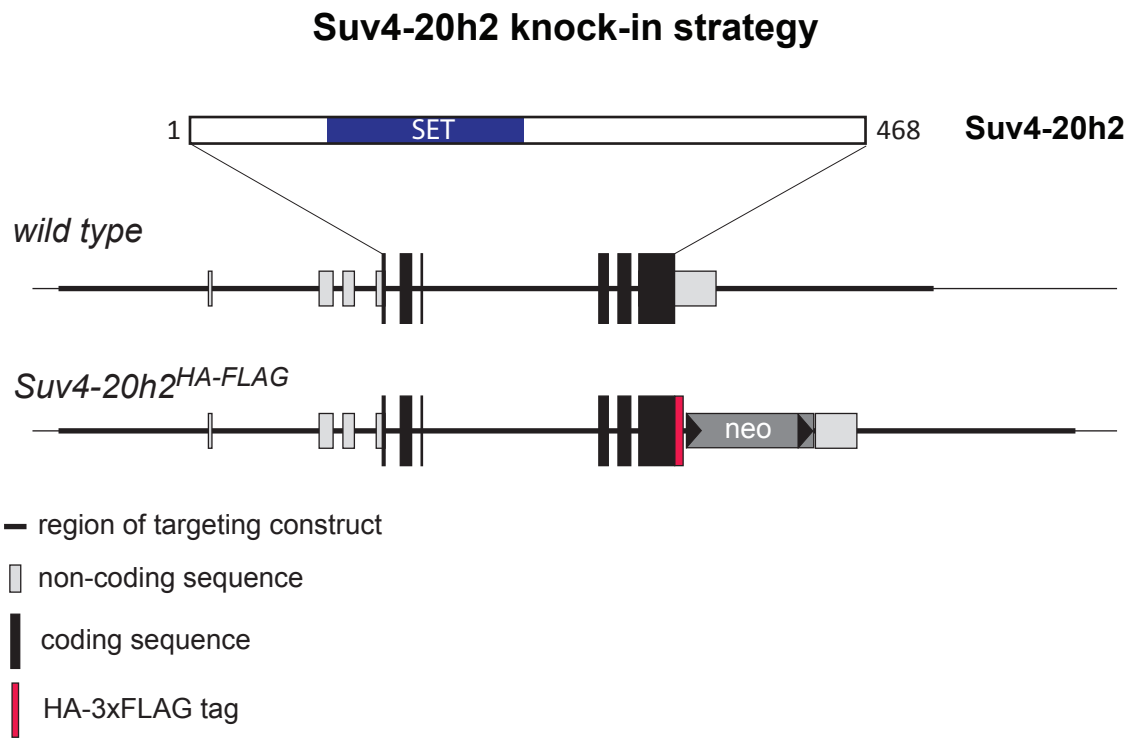
Suv4-20h2 knock-in strategy
1
SET
468
Suv4-20h2
wild type
Suv4-20h2HA-FLAG
neo
region of targeting construct
non-coding sequence
coding sequence
HA-3xFLAG tag

D

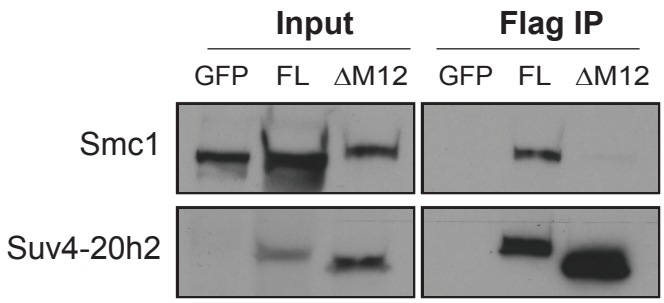
Input
Flag IP
GFP
FL
ΔM12
GFP
FL
ΔM12
Smc1
Suv4-20h2

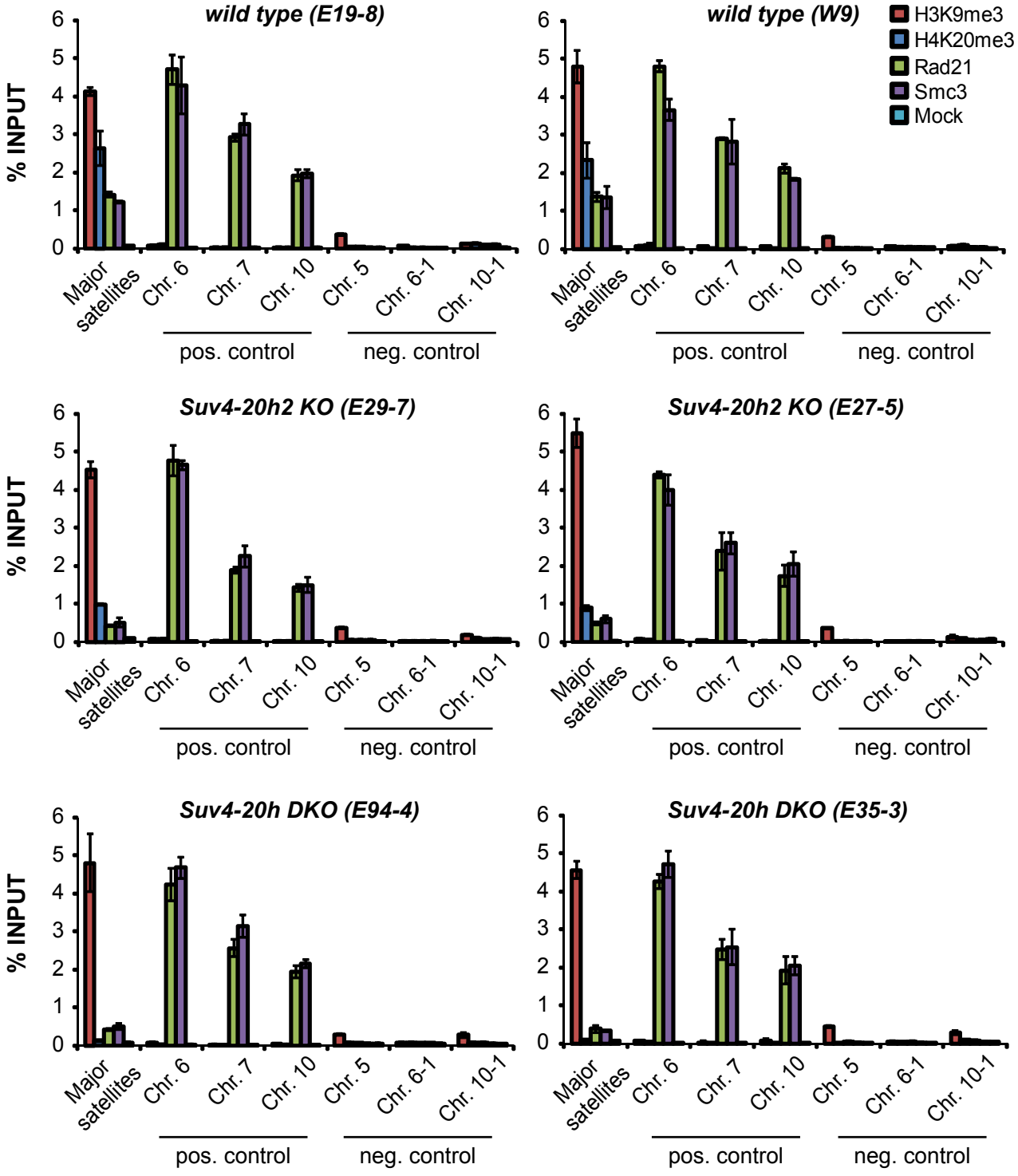
wild type (E19-8)
wild type (W9)
Suv4-20h2 KO (E29-7)
Suv4-20h2 KO (E27-5)
Suv4-20h DKO (E94-4)
Suv4-20h DKO (E35-3)
% INPUT
H3K9me3
H4K20me3
Rad21
Smc3
Mock
Major satellites
Chr. 6
Chr. 7
Chr. 10
Chr. 5
Chr. 6-1
Chr. 10-1
pos. control
neg. control

wild type (W9)

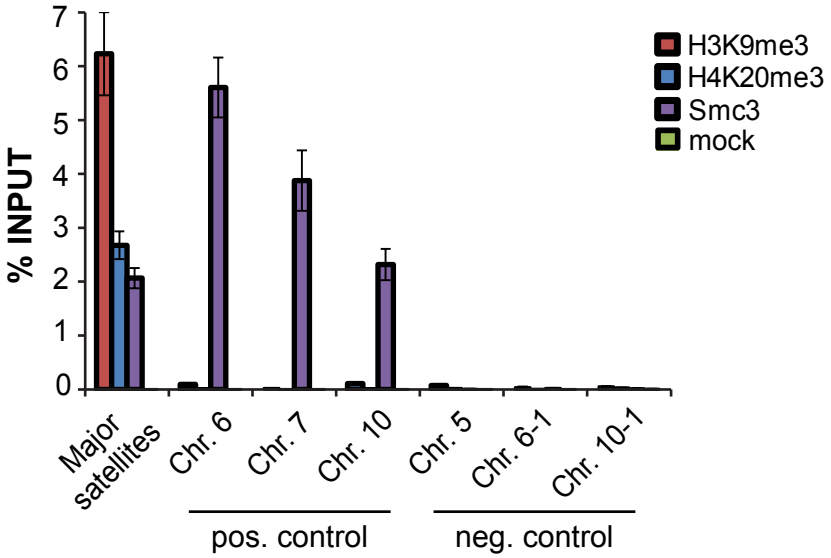

Suv39h DKO (E124-1)

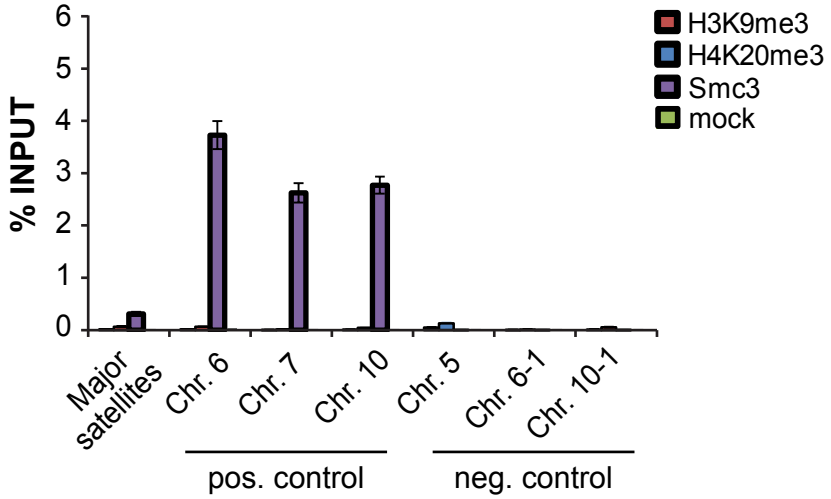

Suv39h DKO (D15)

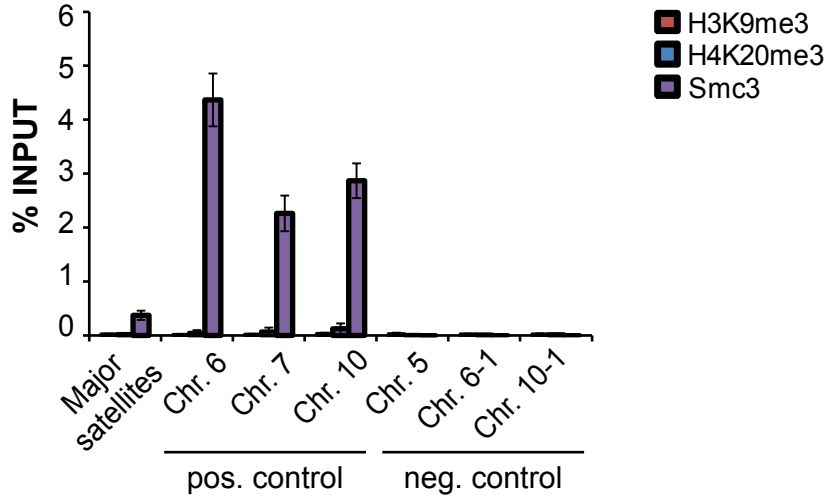

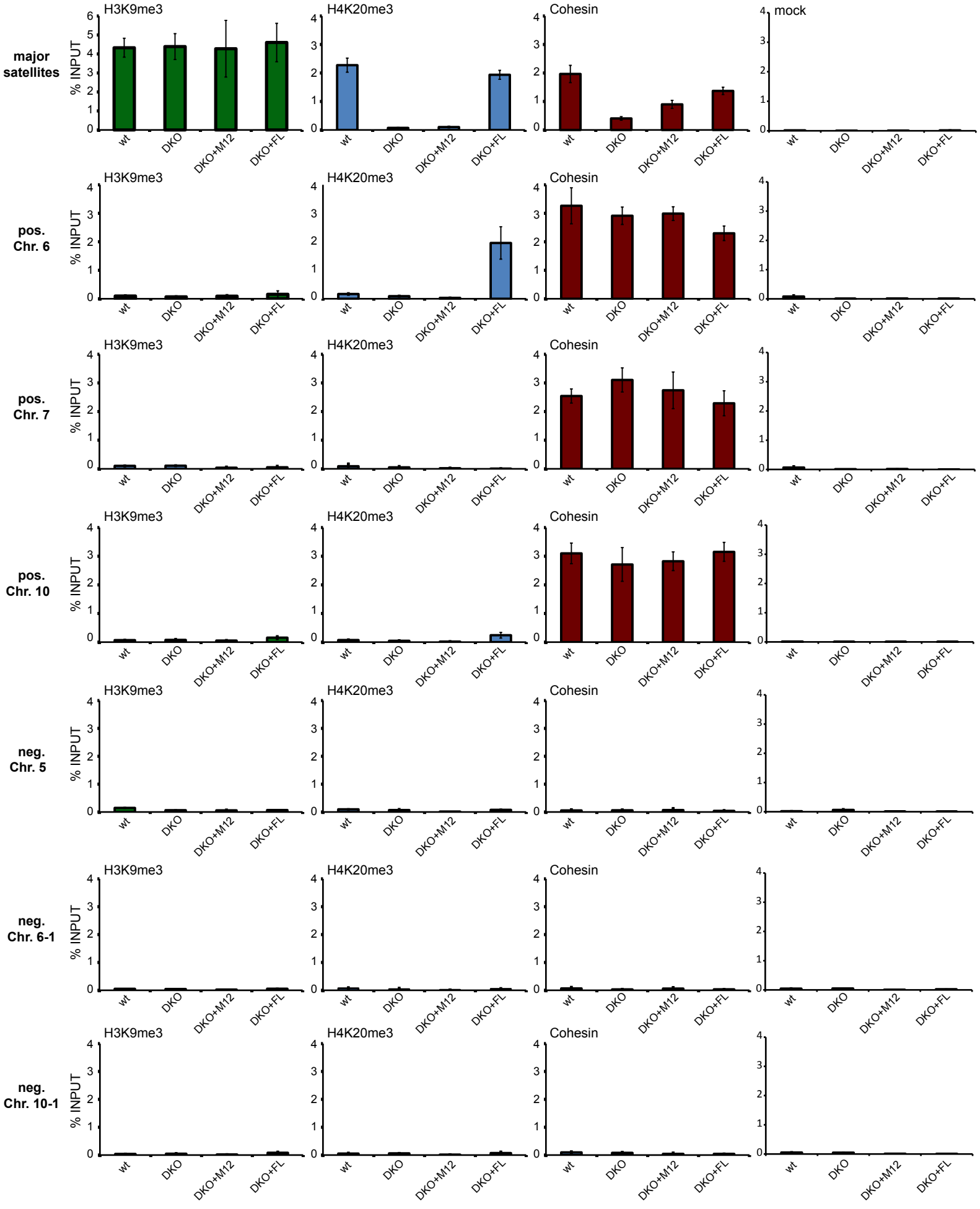
major satellites
pos. Chr. 6
pos. Chr. 7
pos. Chr. 10
neg. Chr. 5
neg. Chr. 6-1
neg. Chr. 10-1
H3K9me3
H4K20me3
Cohesin
mock
% INPUT
wt
DKO
DKO+M12
DKO+FL

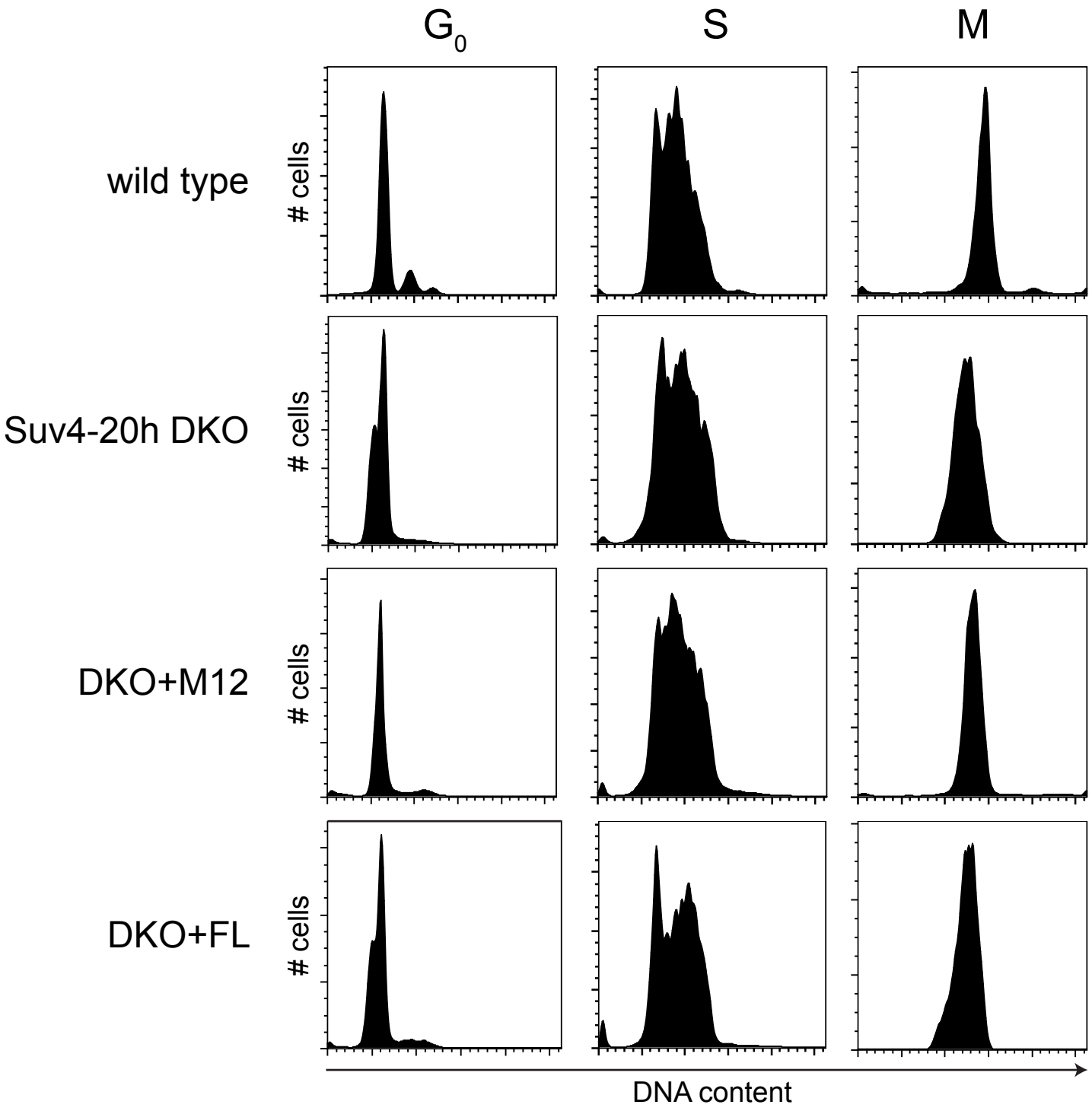
G0
S
M
wild type
Suv4-20h DKO
DKO+M12
DKO+FL
cells
cells
cells
cells
DNA content

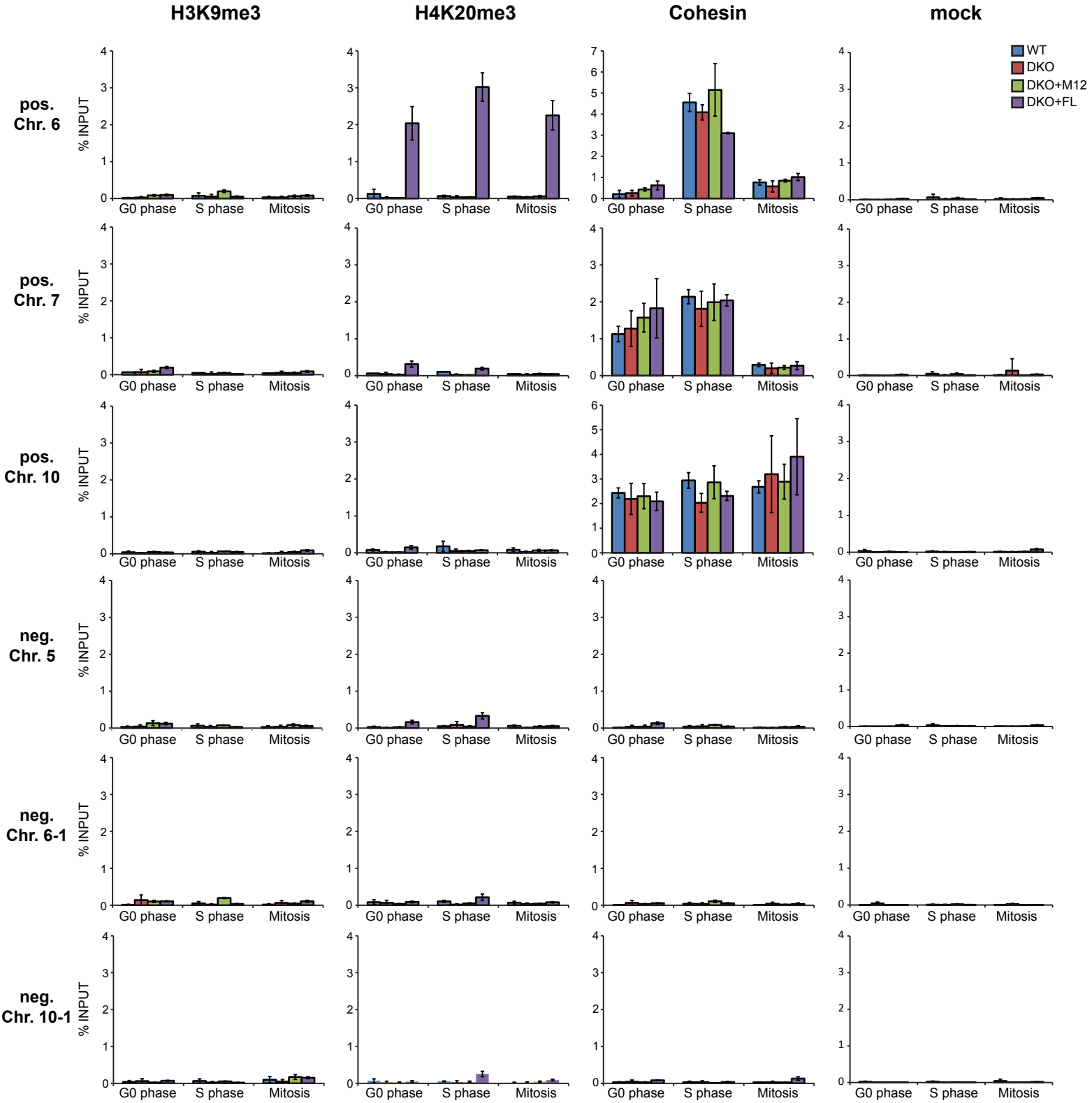
H3K9me3
H4K20me3
Cohesin
mock
WT
DKO
DKO+M12
DKO+FL
pos. Chr. 6
pos. Chr. 7
pos. Chr. 10
neg. Chr. 5
neg. Chr. 6-1
neg. Chr. 10-1
% INPUT
G0 phase
S phase
Mitosis

A

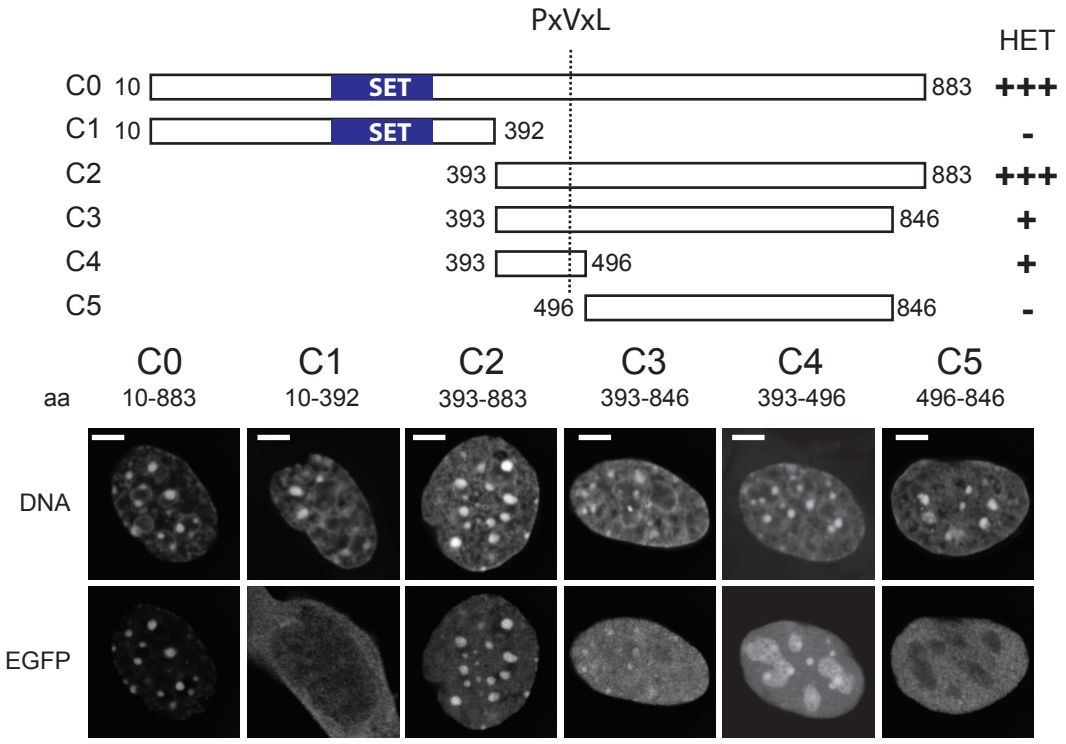
PxVxL
HET
C0 10 SET 883 +++
C1 10 SET 392 -
C2 393 883 +++
C3 393 846 +
C4 393 496 +
C5 496 846 -
C0 C1 C2 C3 C4 C5
aa 10-883 10-392 393-883 393-846 393-496 496-846
DNA
EGFP

B

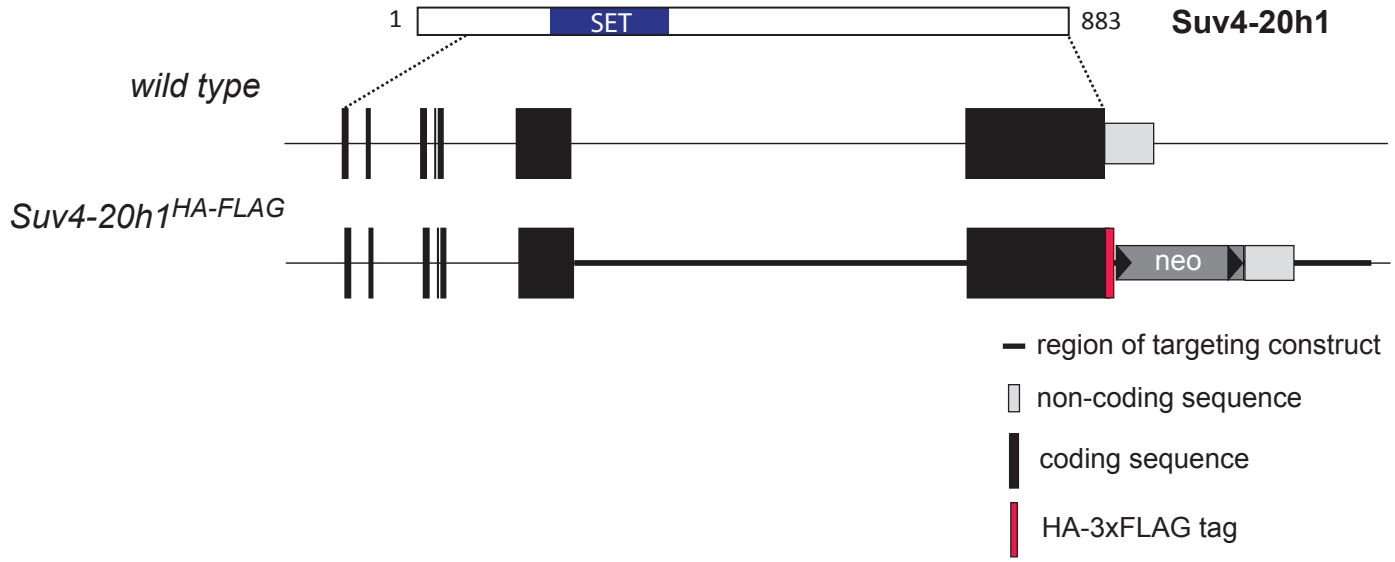
1 SET 883 Suv4-20h1
wild type
Suv4-20h1HA-FLAG
neo
region of targeting construct
non-coding sequence
coding sequence
HA-3xFLAG tag

C

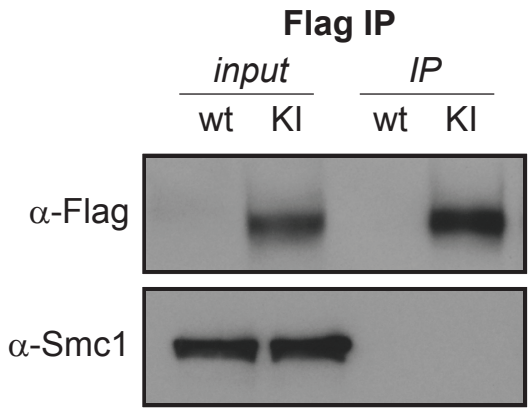
Flag IP
input IP
wt KI wt KI
α-Flag
α-Smc1

A

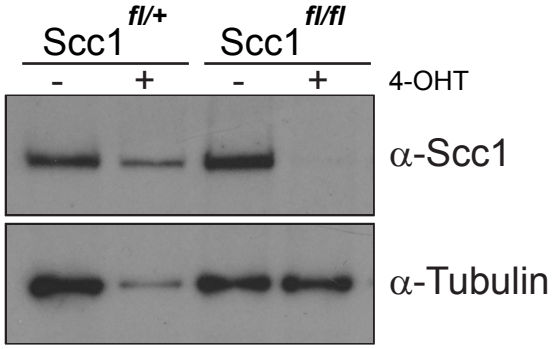

B

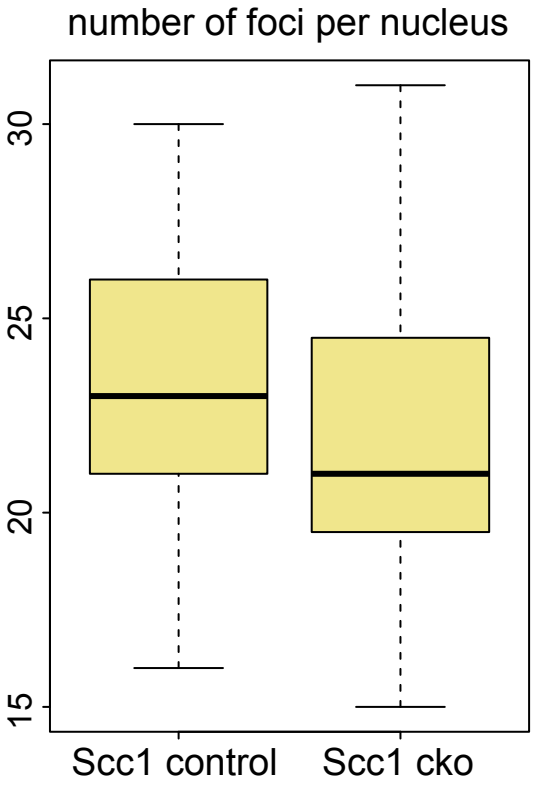

Shapiro-Wilk test

Scc1 control: W=0,9193
p-value=0,04929
Scc1 cKO: W = 0.8979
p-value = 0.01024

F-test

Scc1 control
vs. Scc1 cKO: p-value=0,04495

Welch-test

Scc1 control
vs. Scc1 cKO: p-value=0,1564

A

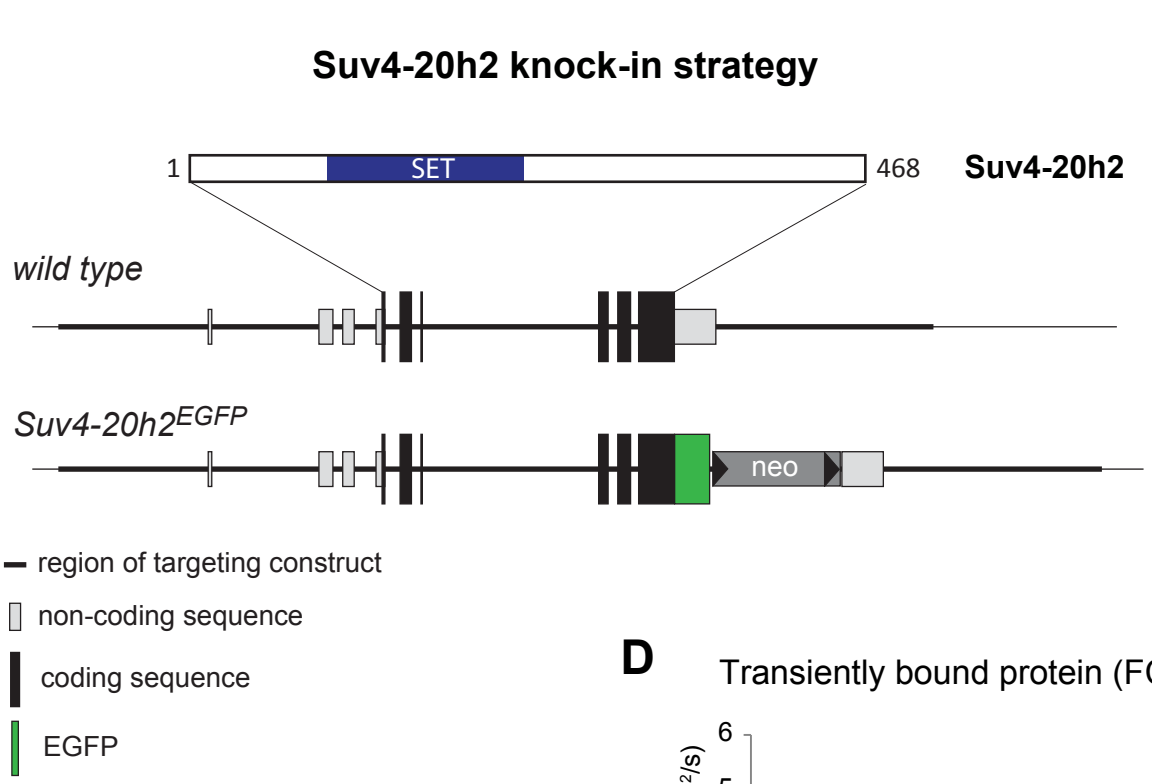
Suv4-20h2 knock-in strategy
1
SET
468
Suv4-20h2
wild type
Suv4-20h2EGFP
neo
region of targeting construct
non-coding sequence
coding sequence
EGFP

B

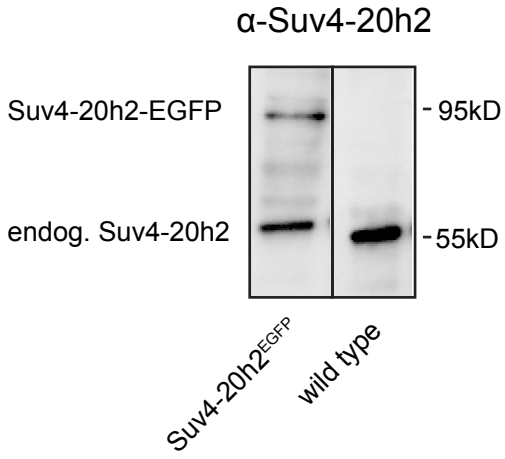
α-Suv4-20h2
Suv4-20h2-EGFP
endog. Suv4-20h2
95kD
55kD
Suv4-20h2EGFP
wild type

C

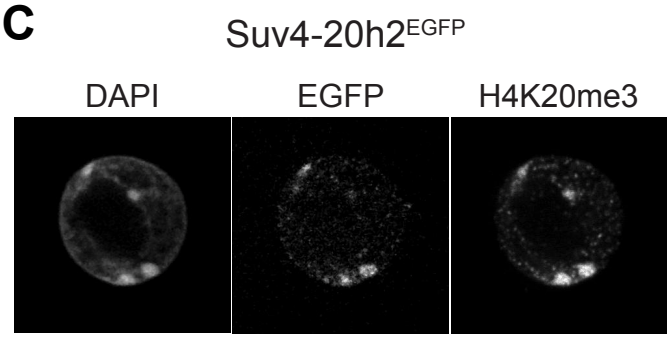
Suv4-20h2EGFP
DAPI
EGFP
H4K20me3

D

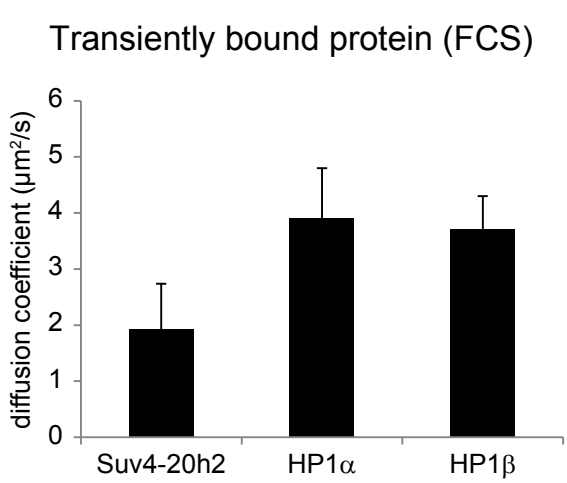
Transiently bound protein (FCS)
diffusion coefficient (µm²/s)
0
1
2
3
4
5
6
Suv4-20h2
HP1α
HP1β

E

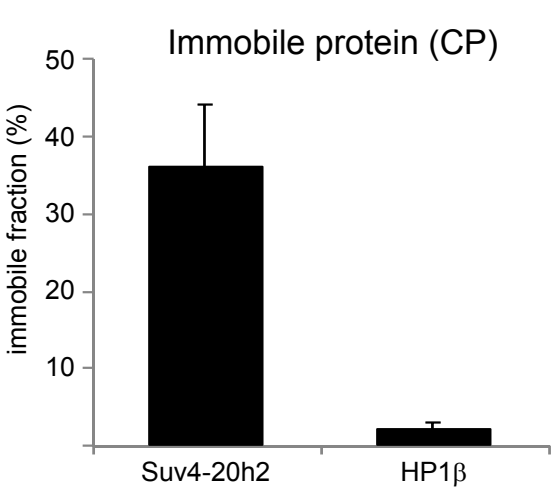
Immobile protein (CP)
immobile fraction (%)
10
20
30
40
50
Suv4-20h2
HP1β

F

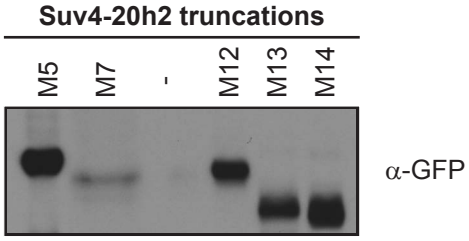
Suv4-20h2 truncations
M5
M7
-
M12
M13
M14
α-GFP

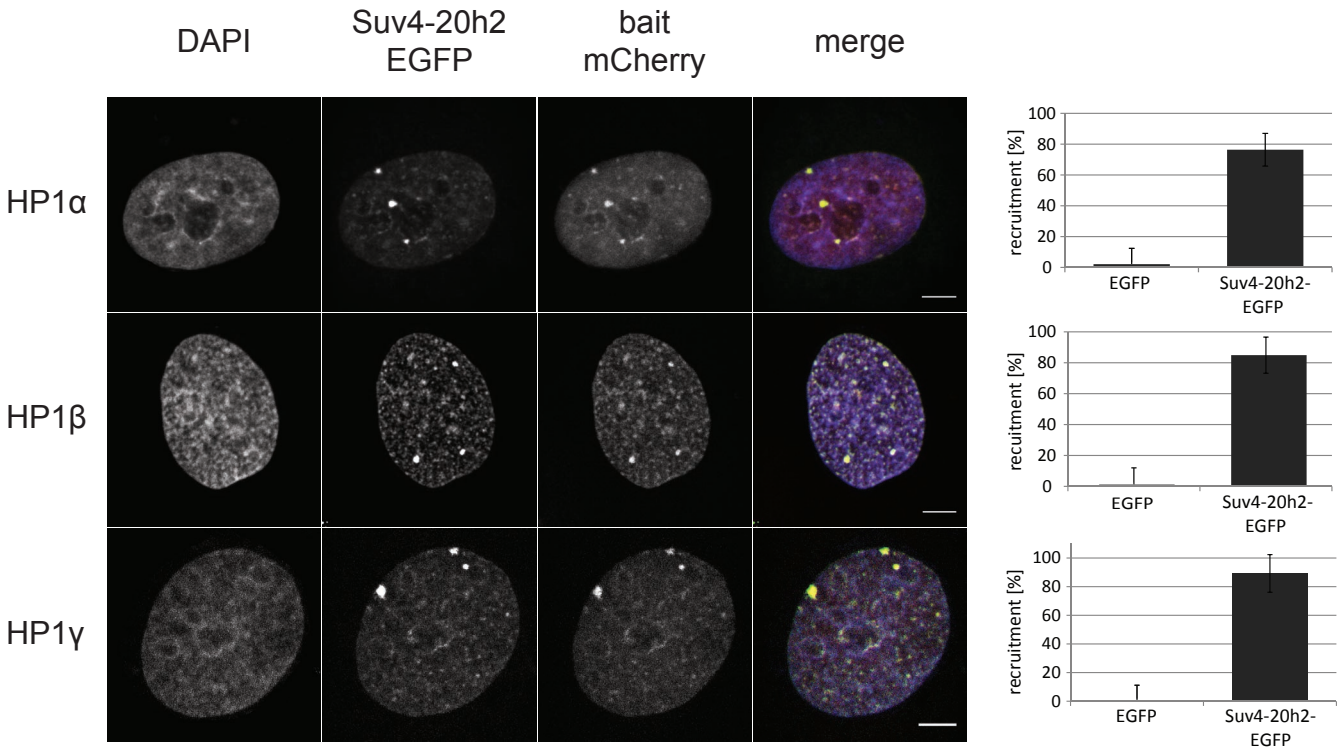
DAPI
Suv4-20h2 EGFP
bait mCherry
merge
HP1α
HP1β
HP1γ
recruitment [%]
100
80
60
40
20
0
EGFP
Suv4-20h2-EGFP

A

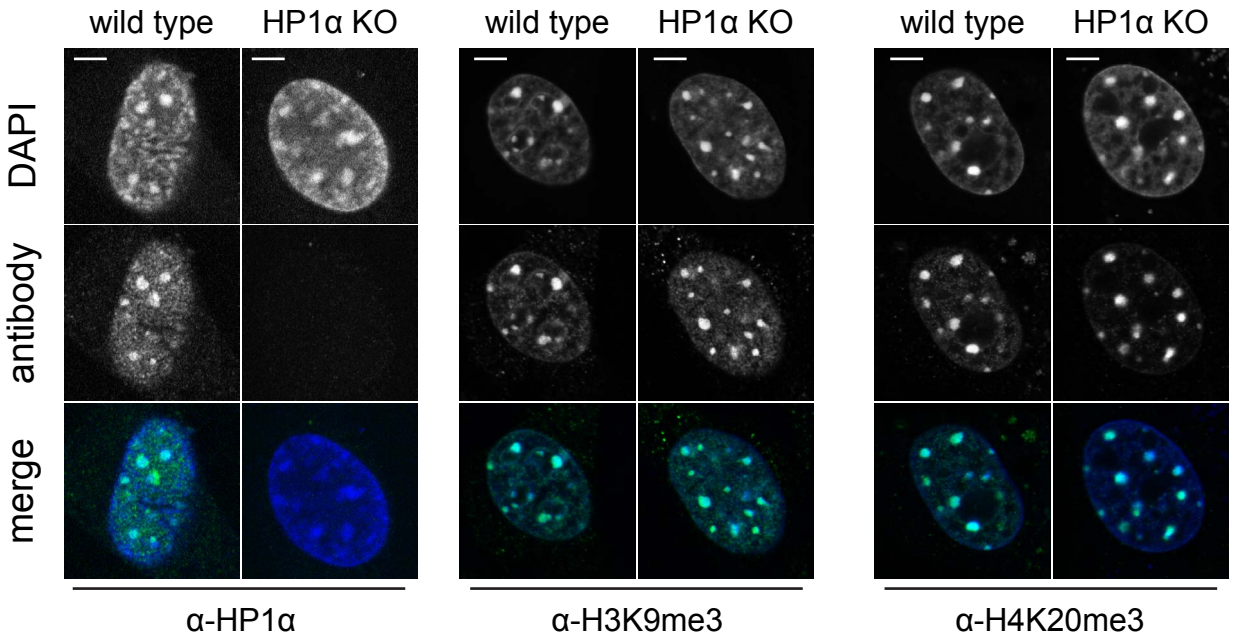
wild type
HP1α KO
wild type
HP1α KO
wild type
HP1α KO
DAPI
antibody
merge
α-HP1α
α-H3K9me3
α-H4K20me3

B

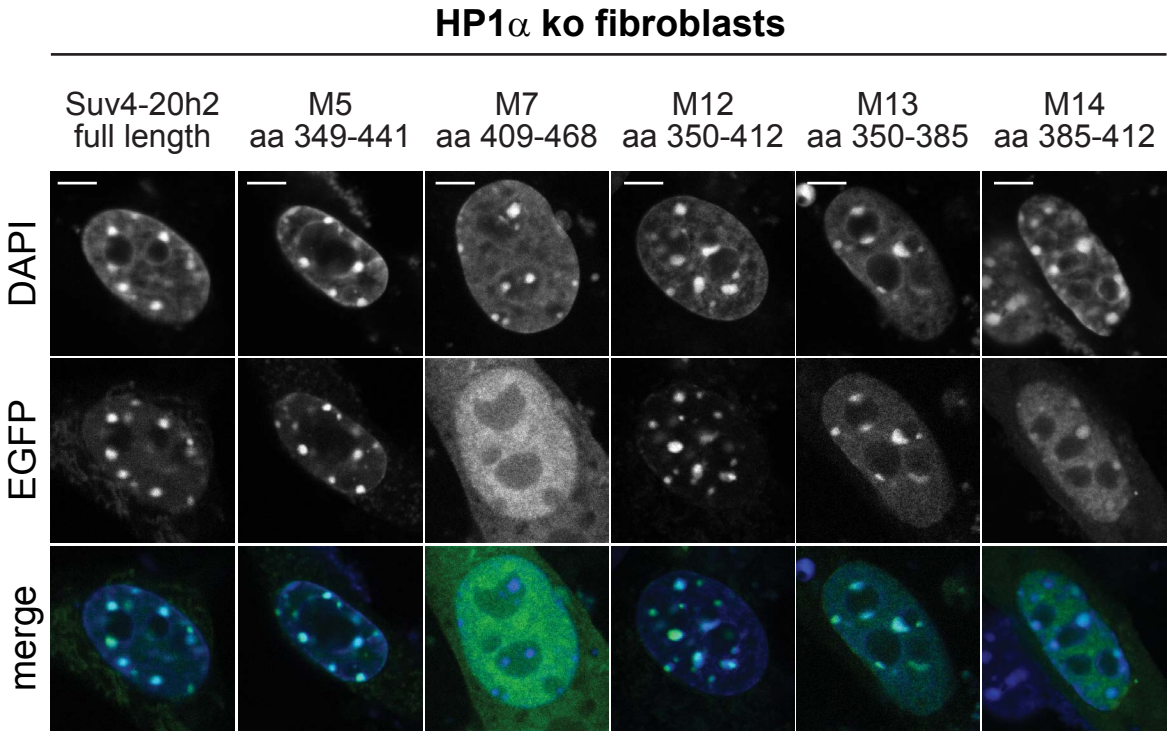
HP1α ko fibroblasts
Suv4-20h2 full length
M5 aa 349-441
M7 aa 409-468
M12 aa 350-412
M13 aa 350-385
M14 aa 385-412
DAPI
EGFP
merge

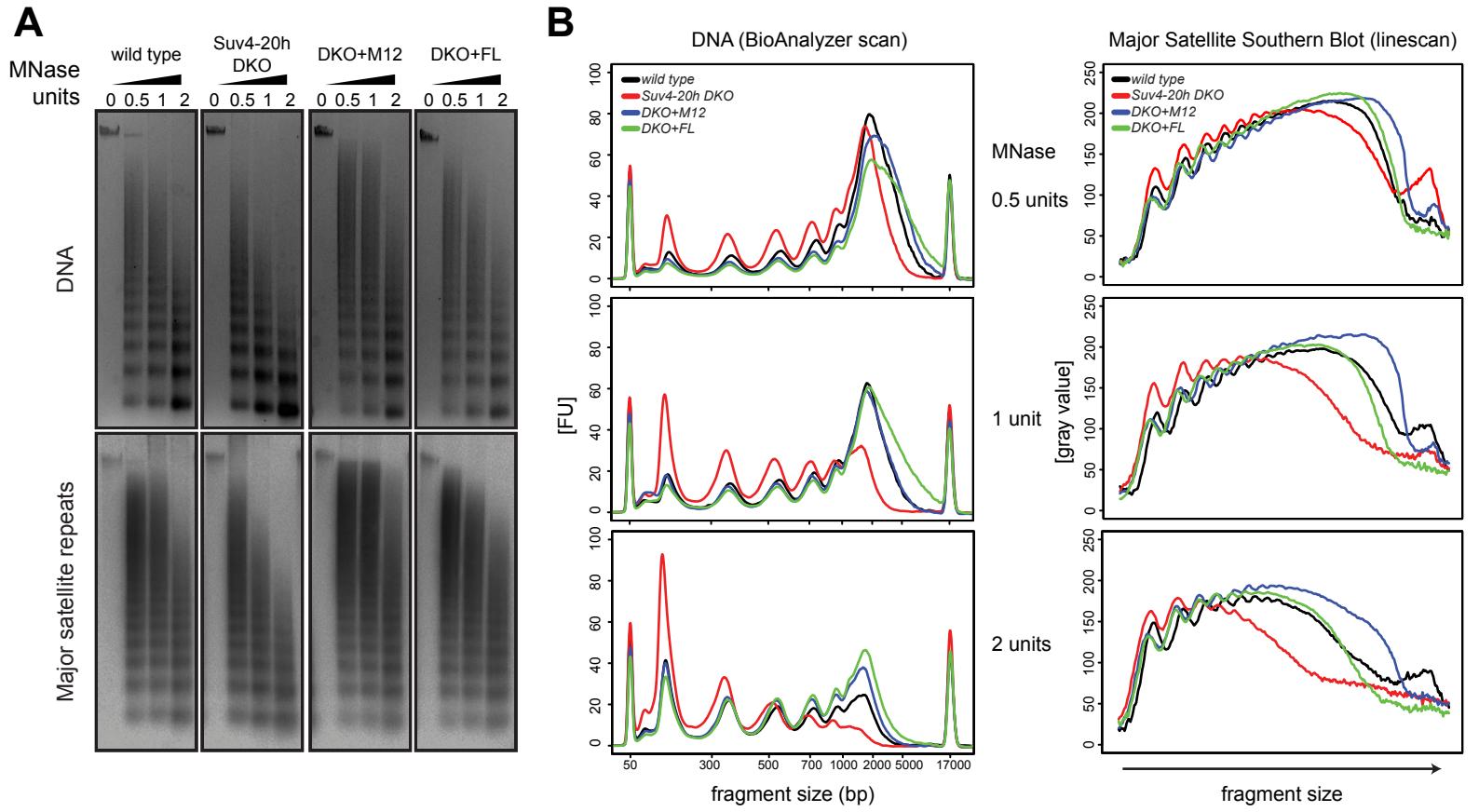
A
MNase units
wild type
Suv4-20h DKO
DKO+M12
DKO+FL
0 0.5 1 2
DNA
Major satellite repeats
B
DNA (BioAnalyzer scan)
Major Satellite Southern Blot (linescan)
wild type
Suv4-20h DKO
DKO+M12
DKO+FL
MNase
0.5 units
1 unit
2 units
[FU]
[gray value]
50 300 500 700 1000 2000 5000 17000
fragment size (bp)
fragment size

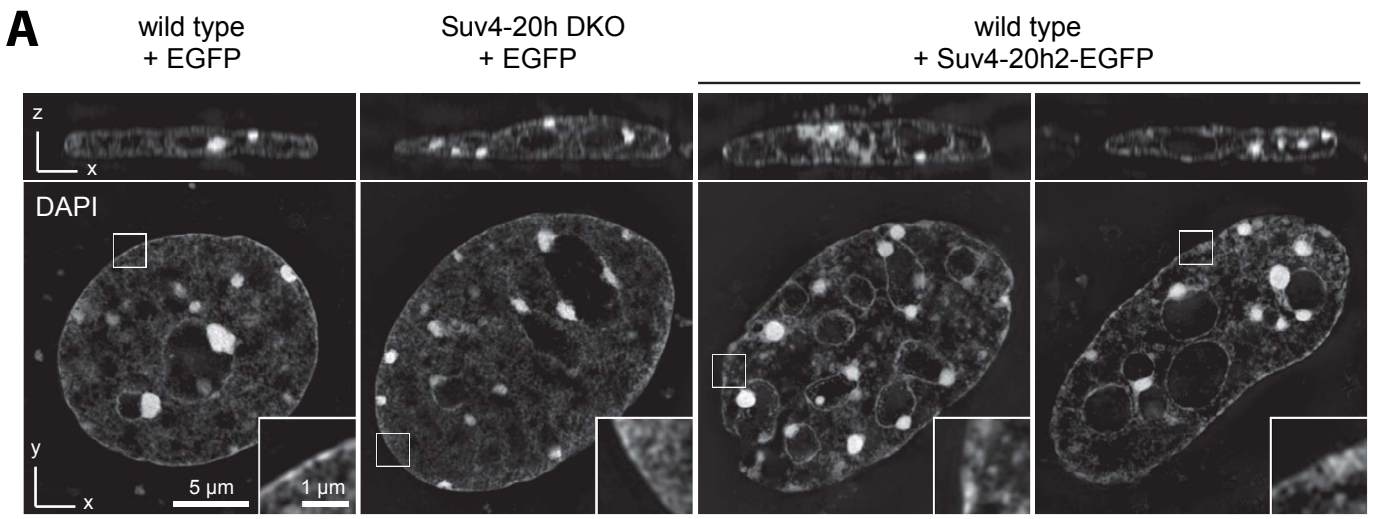
A
wild type
+ EGFP
Suv4-20h DKO
+ EGFP
wild type
+ Suv4-20h2-EGFP
z
x
DAPI
y
x
5 µm
1 µm

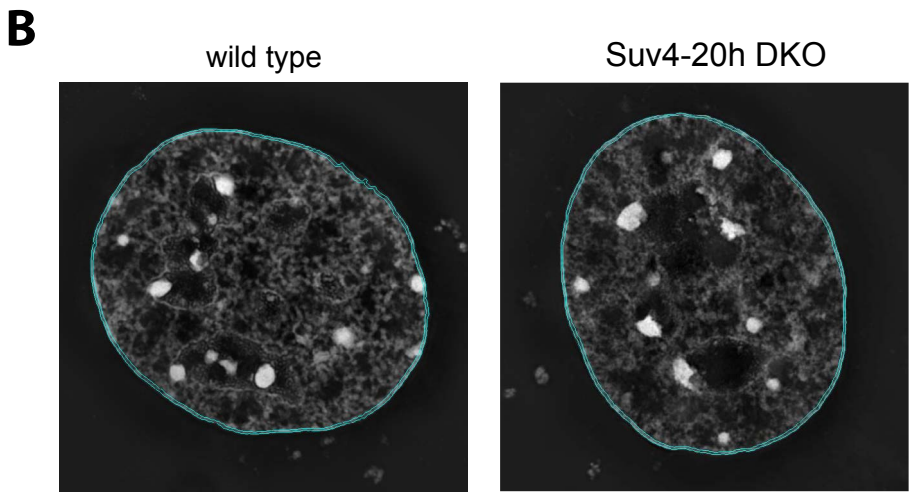
B
wild type
Suv4-20h DKO

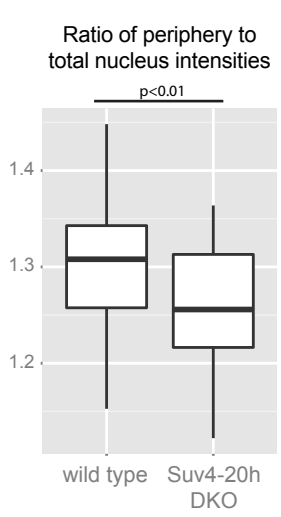
C
Ratio of periphery to
total nucleus intensities
p<0.01
1.4
1.3
1.2
wild type
Suv4-20h
DKO

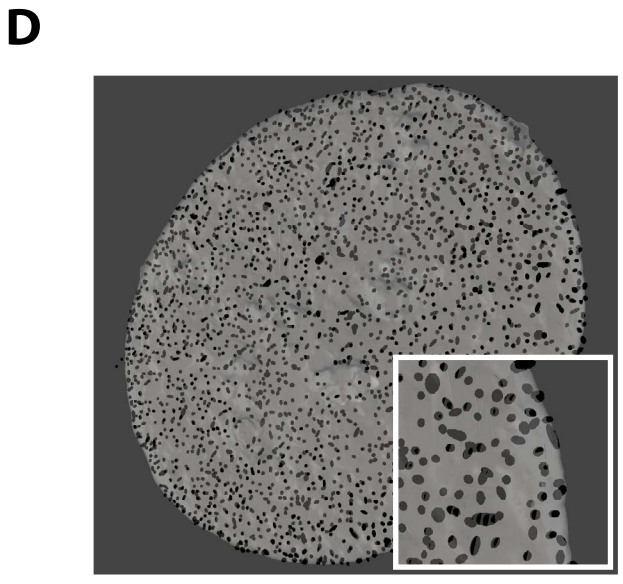
D

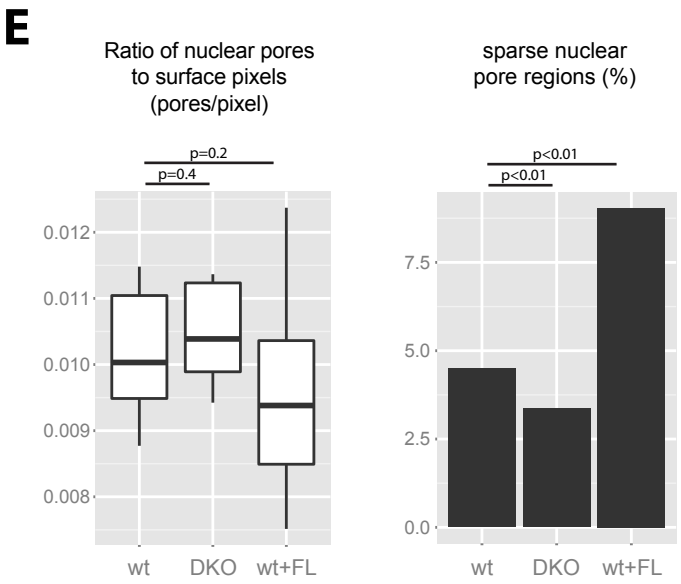
E
Ratio of nuclear pores
to surface pixels
(pores/pixel)
p=0.2
p=0.4
0.012
0.011
0.010
0.009
0.008
wt
DKO
wt+FL
sparse nuclear
pore regions (%)
p<0.01
p<0.01
7.5
5.0
2.5
0.0
wt
DKO
wt+FL

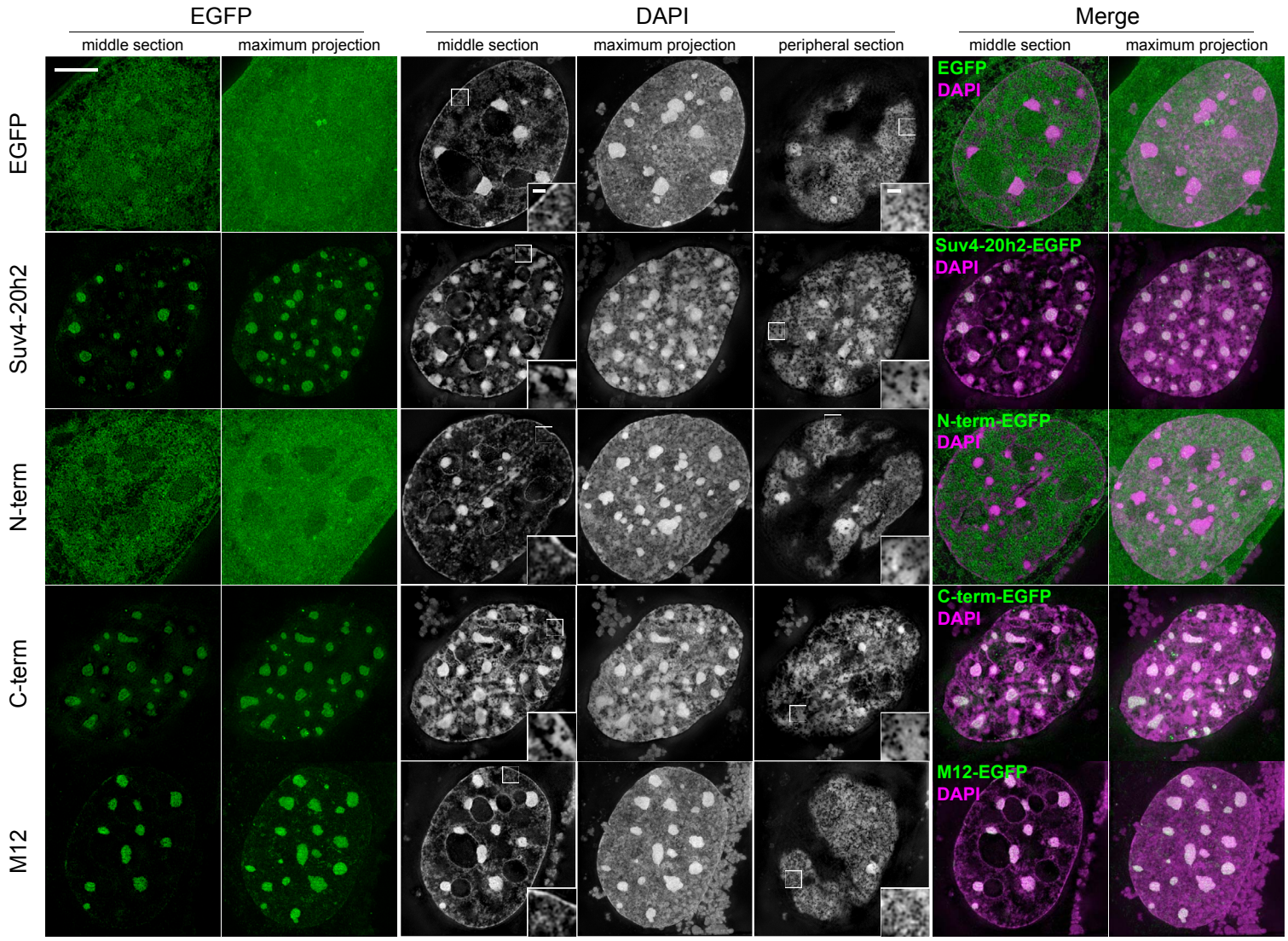
EGFP
middle section
maximum projection
DAPI
middle section
maximum projection
peripheral section
Merge
middle section
maximum projection
EGFP
Suv4-20h2
N-term
C-term
M12
EGFP
DAPI
Suv4-20h2-EGFP
DAPI
N-term-EGFP
DAPI
C-term-EGFP
DAPI
M12-EGFP
DAPI

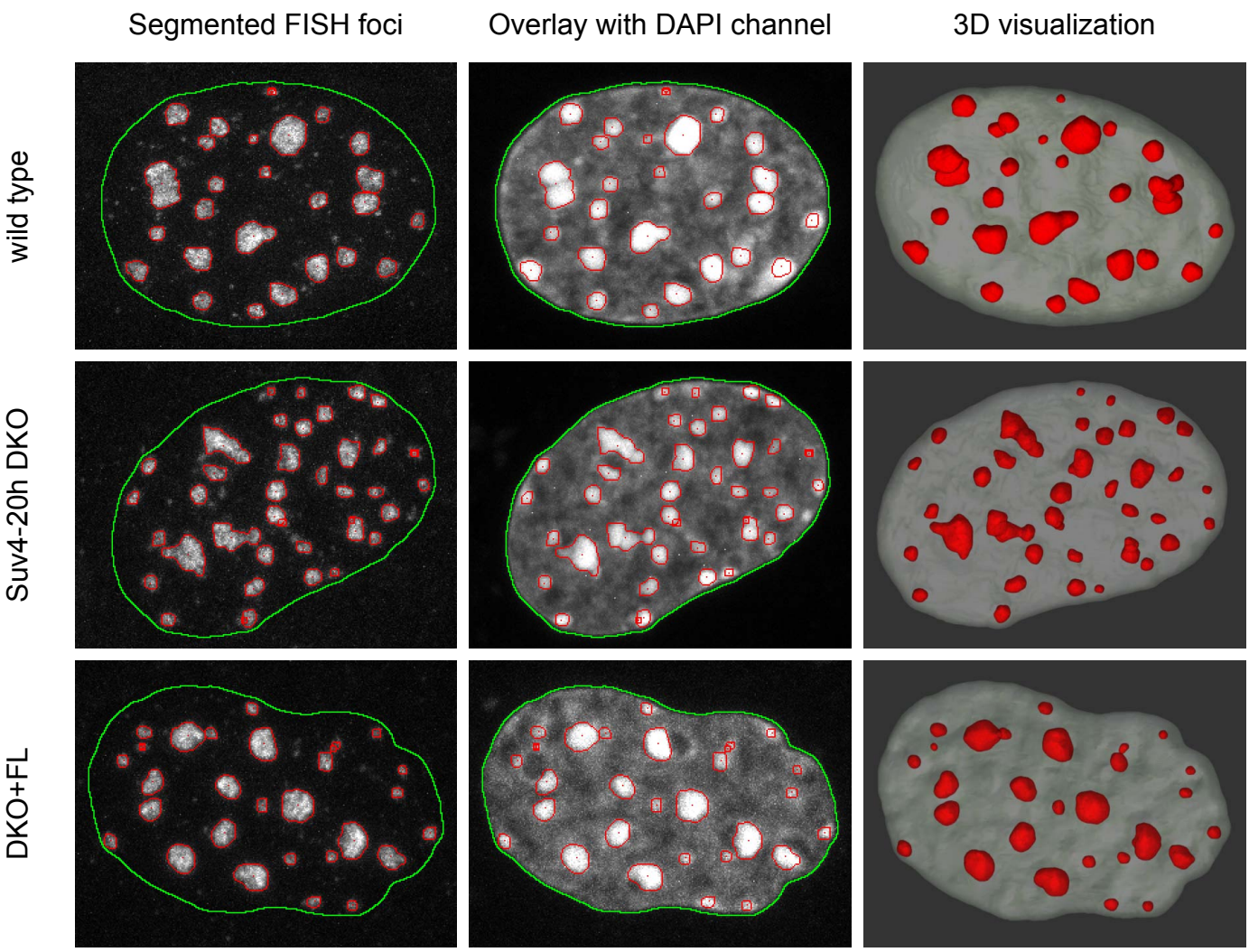
Segmented FISH foci
Overlay with DAPI channel
3D visualization
wild type
Suv4-20h DKO
DKO+FL

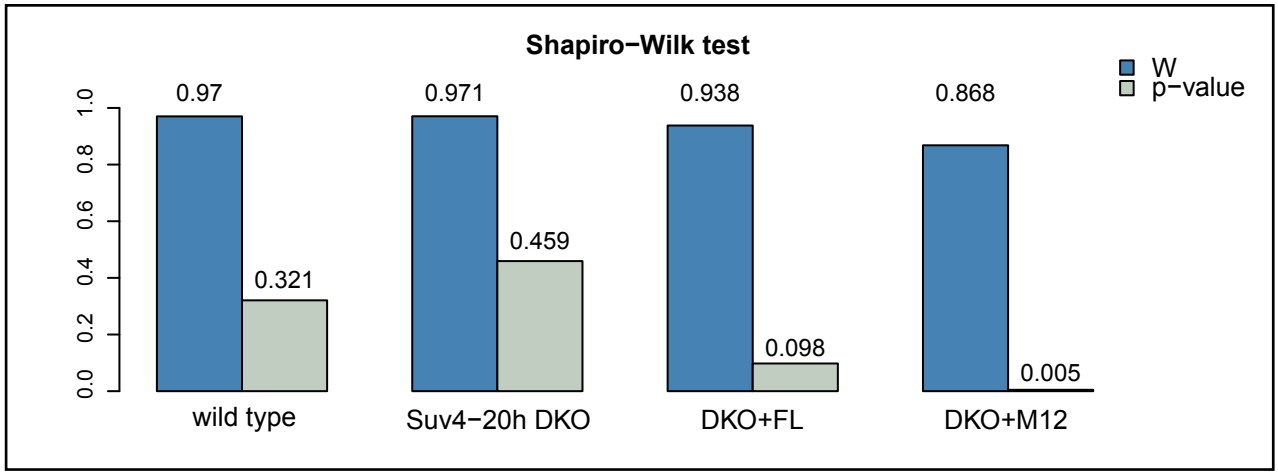
Shapiro−Wilk test
W
p−value
0.0
0.2
0.4
0.6
0.8
1.0
0.97
0.321
0.971
0.459
0.938
0.098
0.868
0.005
wild type
Suv4−20h DKO
DKO+FL
DKO+M12

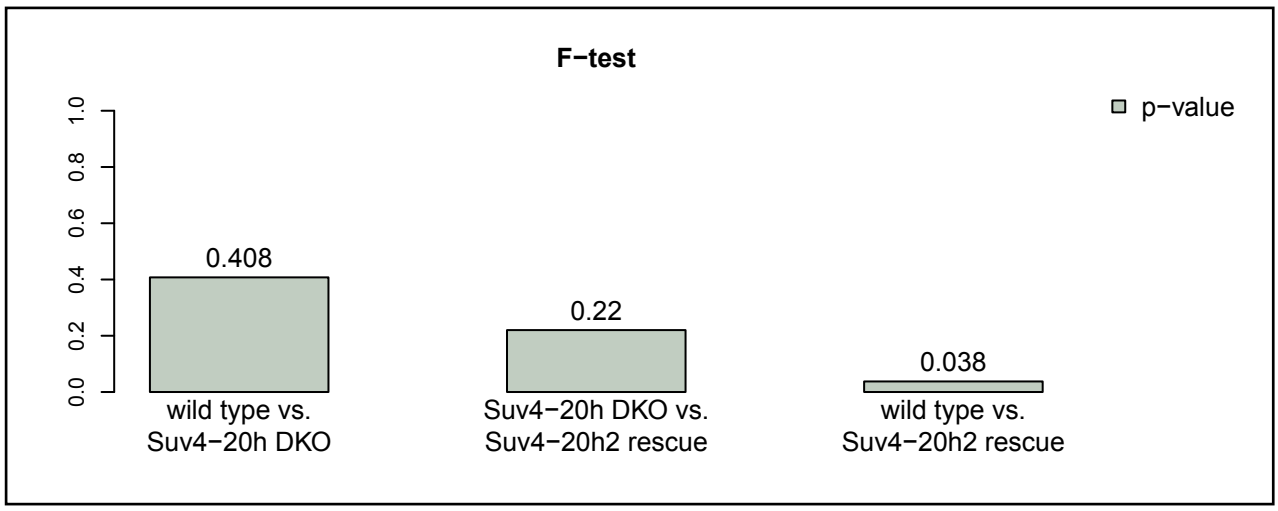
F−test
p−value
0.0
0.2
0.4
0.6
0.8
1.0
0.408
0.22
0.038
wild type vs.
Suv4−20h DKO
Suv4−20h DKO vs.
Suv4−20h2 rescue
wild type vs.
Suv4−20h2 rescue

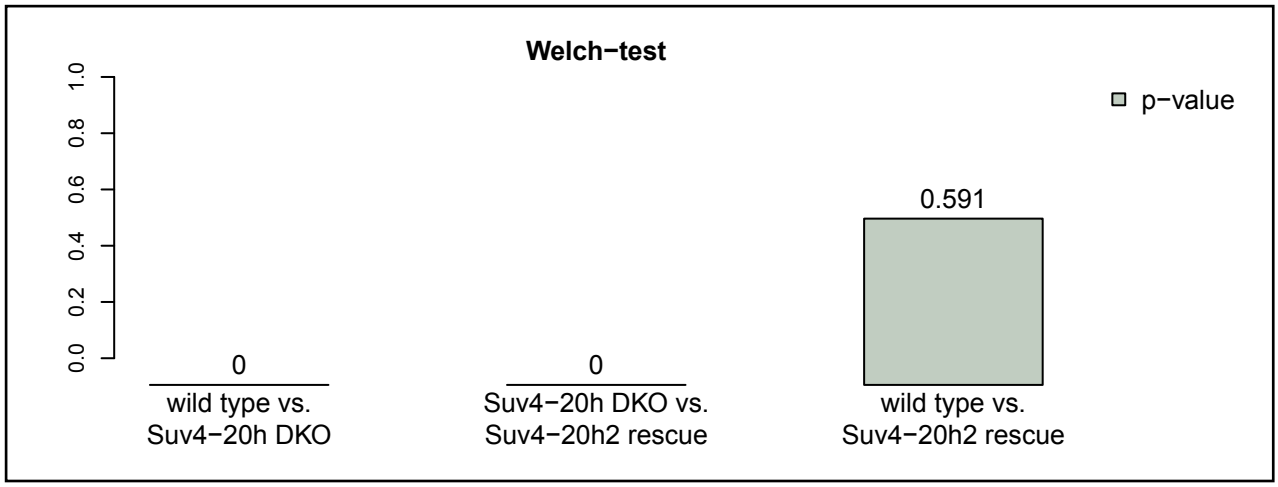
Welch−test
p−value
0.0
0.2
0.4
0.6
0.8
1.0
0
0
0.591
wild type vs.
Suv4−20h DKO
Suv4−20h DKO vs.
Suv4−20h2 rescue
wild type vs.
Suv4−20h2 rescue